POLITECNICO DI TORINO

SCUOLA DI DOTTORATO
PhD Course in Fluidodinamica – XXVIII cycle

PhD Dissertation

Statistical analysis of inhomogeneous fluctuation fields

Scalar transport in shearless turbulent mixing, effects of stratification, solar wind and solar wind-interstellar medium interaction

Luca Gallana
matricola: 200001

Advisor
prof. Daniela Tordella

Marzo 2016

Abstract

Turbulence is a condition that can occur in a broad range of fluids, which may belong to very different physical environments, each with their own unique characteristics. Mathematical and analytical studies are generally limited by the high degree of complexity of the system, therefore, numerical/laboratory experiments and in-situ measurements play a fundamental role in the study of these phenomena.

An analysis on two different anisotropic fluctuating fluid fields has been performed: both flows, while belonging to different physical contexts, are characterized by the presence of multiscale inhomogeneous fluctuations, to which is associated a strong anisotropy, and by the presence of effects related to stratification / mixing.

The first is one of the most simple anisotropic turbulent flow, namely the shearless turbulent mixing, and it has been studied by means of direct numerical simulation of Navier-Stokes equations, with the aim of characterize the passive scalar transport and the effects related to the presence of a thermal stratification. The second is a more complex fluid field, that is the solar wind, which belong to magnetohydrodynamic flows; the analysis on solar wind have been performed taking advantage of in-situ measurement of the Voyager 2 spacecraft, trying to provide a statistical and spectral characterization despite the presence of gaps in the recorded time-series.

Acknowledgements

I would like to thank Daniela Tordella and Michele Iovieno for their help and scientific guidance.

For the code develpment and the computational resources I acknowledge the CINECA award under the ISCRA initiative, for the availability of high performance computing resources and support; the hpc@polito, which is a project of Academic Computing within the Department of Control and Computer Engineering at the Politecnico di Torino (http://www.hpc.polito.it); PRACE for awarding us access to resources Curie based in France at TGCC and Fermi based in Italy at CINECA.

For the access to the Voyager data, the research visiting position at MIT I want to acknowledge the MITOR project and John Belcher; in particular, for the help and advice, as well as for the kindness, I would particularly like to thank John Richardson and Merav Opher.

I also thank the other PhD students with whom I had the pleasure of working: Francesca De Santi, Silvio Di Savino, and Federico Fraternale.

Finally, I thank all my family, friends and all those who supported me in these years.

Contents

Chapter 1

Introduction

The context of turbulent, inhomogeneous flows cover a broad range of fields, also in everyday life – let's think, for instance, to the wake of a ship, the wind blowing, a fast flowing river, etc. Nevertheless, turbulence is one of the greatest unsolved mystery of modern physics – although it is not so famous outside the scientific community. In fact, a model that fully describe turbulence does not exist: the equation are strongly non-linear, strictly related to the initial conditions, and predict the evolution of the flow is very difficult. Also Kolmogorov postulated, where it says that the dissipation scale are locally isotropic, it's not true: both inertial and dissipative scales are anisotropic, reflecting the large-scale structure (Frisch, 1995; Warhaft, 2000). As evidence of the difficulties in obtaining an universal solution, there is a quote attributed to Heisenberg (Gleick, 1987) that reads: "There is a story about Heisenberg on his deathbed, declaring that he will have two questions for God: Why relativity? and Why turbulence? Heisenberg says, – I really think He may have an answer only to the first question.". Nowadays there are many theoretical studies to simple flows , first of all the homogeneous isotropic turbulence.

In this thesis two different kind of turbulent, inhomogeneous flows are studied. Both flows, while belonging to different physical contexts, are characterized by the presence of multiscale inhomogeneous fluctuations, to which is associated a strong anisotropy (particularly in large scales, but not only), and by the presence of effects related to stratification / mixing. In the first part we deeply examine the phenomenology of one of most simpler inhomogeneous flows, that is a shear-less turbulent mixing, focusing in particular on the transport of passive scalars, and on the effects of temperature stratification, taking advantage of direct numerical simulations. Instead, in the second part, we analyze a real, more complex flow, that is the solar wind, trying to identify (and, if present, characterize) the turbulent behavior in the outer heliosphere – starting from few astronomical units (around 5 AU), with the objective of expanding the study to the edge of the heliosphere (distance of the order of 100 AU).

For what concern our first study, it is important to observe that the transport of passive scalars (that can be temperature, concentration of a pollutant, fluorescence or another quantity which is transported by the flow, without affecting the flow field itself) is not as simple as it may seem at first sight. Even if the transport equation for the scalar field is linear, the scalar transport is not a simply footnote of the turbulence, as many experiment performed in past years have shown: a peculiar aspect is that intermittency in the scalar fluctuations is observed even in presence of a Gaussian velocity field, and the small scales show an anysotropic behavior even for large Reynolds number. Both these apparently distinctly effects – local anisotropy at the small scales, and the internal intermittency – are not provided by the Kolmogorov-Obuchov-Corrsin (KOC) phenomenology (Sreenivasan, 1996). Many semi-empirical law have been expressed, but none can explain well the turbulence phenomenology. This is why in-situ measurement and laboratory/computational experiments are still important to analyze turbulence.

The reason that prompts to explain (and to predict) how a scalar is transported is that it is a phenomenon very present in real disciplines, for example meteorology, combustion engineering, biology, experimental aerodynamics, cosmology. Of course phenomenon to be studied may involve the presence of other effects (as buoyancy for atmospheric phenomena) that may adds nonlinearities to the problem. In such case there is a feedback of the scalar concentration on the flow field and, therefore, there is a two-way coupling between the scalar and momentum equation, with relevant effects on the time evolution of the system (Davies Wykes & Dalziel, 2014). Mixing across stratified interfaces is a frequent phenomenon in geophysical and engineering flows. Some common geophysical examples are the deepening of the upper-ocean mixed layer into the stably stratified pycnocline owing to turbulence induced by surface wind or cooling, the thickening of the sediment-suspension layer in the oceanic benthic boundary layer, and the growth of the planetary boundary layer (Fernando, 1991).

The solar wind fills the heliosphere, from the Sun to the termination shock with a supersonic flow of magnetized plasma. This flow is time dependent on all scales and expands with distance. The solar wind is characterized by a broad range of phenomena, in particular sharp changes in the flow and extreme conditions can often be met due to the crossing of the heliospheric current sheet, the presence of shocks and interaction regions between slow and fast wind streams and zones of strong density variations. Flow fluctuations are not just convected outward but show active energy cascades among the different scales. The solar wind turbulence phenomenology has been comprehensively reviewed by Tu & Marsch (1995) and Bruno & Carbone (2013). Most studies of solar wind turbulence use data from near-Earth, measured by spacecraft in the ecliptic near 1 AU (Tu & Marsch, 1995). In order to understand the evolution of the solar wind and its properties, it is necessary to analyze data at large radial distances. However, data gaps in the measured time series typically increase with the distance from the sun and make the spectral analysis challenging: at 5 AU 27 % of the data are missing, while in the heliosheath almost 97 % of the high resolution data are absent (70 % considering hourly averaged data).

This thesis is divided into two main sections. In the first part we will consider a shear-less turbulent mixing obtained coupling two homogeneous turbulence, focusing on the passive scalar transport and on the effects related to the presence of buoyancy forces – stratified flows. In particular, we introduce the passive scalar problem in chapter 2 and the stratified turbulence in chapter 3. An overview on equation used and our Navier-Stokes numerical code is given in chapter 4.

The second part of this thesis concern the solar wind study performed using the Voyager spacecraft data, and on the problem related to the analysis process due to the presence of gaps in the dataset. Chapter 5 focus on the characterization of the flow at 5 AU, methods to perform spectral analysis on gapped dataset, andresults for low gapped data (at distance of the around 5 AU from the sun); some preliminary results on heliosheath data analysis (at distance of the order of 100 AU) are presented in section 5.5. General conclusion are reported in chapter 6.

Part I

Shearless Turbulent Mixing

Chapter 2

Passive Scalar Transport

As defined in the introduction, a passive scalar is a quantity transported by a fluid flow, without having any influence on its motion. As said, the transport of a passive substance within a turbulent field is an important process in many natural and engineering contexts (i.e. chemical mixing, combustion, and pollutant dispersal in oceanography and atmospheric science). As a consequence, it is important to understand and predict the mixing and dispersion rates of passive scalars in order to evaluate, for example, the efficiency of mixing and combustion, or environmental pollution. To understand the high number of involved phenomena, it can be observed that also the propagation of light and radio waves in the atmosphere is influenced by the distribution of small scale temperature gradients and water vapour concentration, which, in a first simplification, almost behave like passively advected substances.

The concentration of a passive substance exhibits a complex behavior, showing some phenomenological parallels with the advecting turbulent velocity field, but the statistical properties of passive scalar concentration are only partly influenced by the Kolmogorov cascade phenomenology. In part, in fact, these properties are decoupled from those of the underlying velocity field. The phenomenological picture of scalar transport is thus undergoing a reinterpretation in last years as empirical evidence shows that local isotropy, both at the inertial and dissipation scales, is violated, see the recent reviews by Sreenivasan & Antonia (1997), Shraiman & Siggia (2000) and Warhaft (2000).

The classical view due to Taylor-Kolmogorov of small-scale velocity and scalar fields in fully developed homogeneous turbulence is based on the idea that small scales are not directly influenced by large-scale and therefore must be locally isotropic. This view does not always agree with measurements of higher moments in turbulent flows, in particular in presence of anisotropic or intermittent large-scale motions or anisotropic forcing, as described by Frisch (1995), Hunt *et al.* (1988), and Shraiman & Siggia (2000). In the case of an imposed mean scalar gradient, experimental measurements and numerical simulations show that scalar gradients aligned with the imposed mean gradient are on average larger than those perpendicular to the mean gradient (Pumir, 1994; Mydlarski & Warhaft, 1998; Warhaft, 2000). Measurements do not indicate that the small scales tend to become isotropic as the Reynolds number increases. Furthermore, some of the anomalous statistical behavior of passive scalar turbulence, such as scaling properties and appearence of coherent structure, occur even for a scalar transported by a simple random Gaussian velocity field (Kraichnan, 1974, 1994; Holzer & Siggia, 1994).

Moreover, dispersion usually occurs in time dependent inhomogeneous flows, which are hard to describe with analytical models or, in many cases, even with numerical simulations. A simple inhomogeneous time dependent situation that can be numerically analysed is a shear-free mixing layer. The mixing, for this case, is an important test field for the non-trivial statistical aspects of the scalar fluctuations which studies (Shraiman & Siggia, 2000; Donzis & Yeung, 2010; Danaila *et al.*, 2012) show to originate in the mixing process itself, rather than being inherited from the complexity of the turbulent velocity field. In connection with that, in this chapter we describe the study we have carried out on the turbulent transport of a passive scalar across an interface, which is represented by a thin layer with a large mean scalar gradient, which separates two regions with uniform concentration, observing the evolution of an initial value problem system, obtained by the imposition of the initial condition. The interface matches two homogeneous isotropic turbulent fields (HIT) with different levels of kinetic energy: the global velocity field is then composed by an high kinetic energy HIT which can convectively diffuse into a lower energy one, producing a shear-less mixing in the interacting region. This mixing region is characterized by an highly intermittent thin layer - where the energy flux is maximum - that propagates into the low energy region, see Tordella & Iovieno (2006); Tordella *et al.* (2008); Tordella & Iovieno (2011, 2012). It should be noticed that this field features a compression of the fluid filaments normal to the interface, that is signature of the small scale anisotropy Tordella & Iovieno (2011). This local compression is also a feature associated with the ramp and cliff structure of the scalar field observed in the case of an imposed mean scalar gradient in anisotropic turbulent like flow field (Holzer & Siggia, 1994; Warhaft, 2000; Gotoh *et al.*, 2011). The study is carried out by means of the direct numerical simulation of the Navier-Sokes and advective-diffusive equations. The presence of the interaction zone offers the way to carry out numerical measurements of the long-term temporal turbulent diffusivity in an inhomogeneous context.

The results shown in this chapter have been presented in the IX EFM Conference (Iovieno *et al.*, 2012, Rome) and XXI AIMETA Conference (Di Savino *et al.*, 2013, Turin) and published on the Journal of Turbulence (Iovieno *et al.*, 2014).

The initial condition construction and computational method are described in section 2.1. In section 2.2, we document the passive scalar turbulent transport in two and three dimensions by means of one-point Eulerian statistics, which describe the first four centered moments of the passive scalar concentration In three dimension, the highest Taylor microscale Reynolds number is 250. For what concern two dimensional flow, the equivalent Re_λ is also equal to 250. In section 2.3 we show that the doubled intermittency layer can be generated by simple transverse wave perturbations of the initial interface separating the velocity and passive scalar fields. Conclusion remarks about this chapter are in section 4.

2.1 Method

The Navier-Stokes equations for an incompressible fluid have been solved in a parallelepiped domain together with the advection-diffusion equation for a passive scalar,

$$\frac{\partial \theta}{\partial t} + u_j \frac{\partial \theta}{\partial x_j} = \kappa \nabla^2 \theta \qquad (2.1)$$

where θ is the passive scalar concentration, u_j is the velocity field and κ is the diffusivity of the passive scalar. Figure 2.1 shows a schematic diagram of the flow configuration and the coordinate system used. For the initial condition, two isotropic fields are separated by a thin layer which is as thick as the correlation length ℓ. From a numerical point of view, the flow is assumed to be contained in a parallelepiped (or a rectangle in two dimensions) and periodic boundary conditions are applied to all the spatial directions. The coordinate system is chosen with the x axis along the direction of the kinetic energy gradient, axis y_1 and y_2 along the homogeneous directions. The initial condition is obtained by matching two homogeneous and isotropic fields with the same integral scale but each with different turbulent kinetic energy as in Tordella & Iovieno (2006); Tordella *et al.* (2008); Iovieno *et al.* (2014); Gallana *et al.* (2014*a*). In practice, the initial condition is generated as

$$u_i = u_i^{(1)} p(x)^{\frac{1}{2}} + u_i^{(2)} (1 - p(x))^{\frac{1}{2}},$$

where $u_i^{(1)}$ and $u_i^{(2)}$ are two homogeneous and isotropic velocity fields with turbulent kinetic energies equal to E_1 and E_2, respectively. The weighting

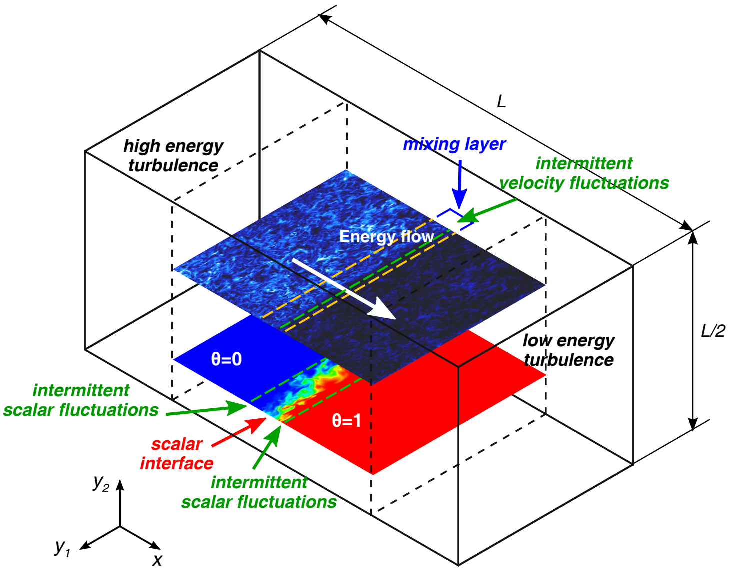

Figure 2.1. System configuration with coordinate system. Since the boundary conditions are periodic periodic, the computational domain includes two mixing layers along the x direction, which is the direction where the inhomogeneity takes places. The dashed lines indicate the central part of the domain where results are presented. The other two directions (in this chapter y_1 and y_2) are homogeneous. L is the domain size in x direction. As a reference dimensional field, we considered the following set of data: domain size $L = 4{,}1$ m, kinematic viscosity 1.5×10^{-5} m^2/s, integral scale $\ell = 1.0 \times 10^{-1}$ m and turbulent kinetic energy $E_1 = 5.0 \times 10^{-4}$ J/kg ($Re_\lambda = 45$), integral scale $\ell = 1.18 \times 10^{-1}$ m and turbulent kinetic energy $E_1 = 4.8 \times 10^{-2}$ J/kg ($Re_\lambda = 150$),integral scale $\ell = 1.34 \times 10^{-1}$ m and turbulent kinetic energy $E_1 = 1.3 \times 10^{-1}$ J/kg ($Re_\lambda = 250$); energy ratio $E_1/E_2 = 6.7$ for all Renolds numbers. The initial conditions for the velocity are generated by a linear matching of two homogeneous and isotropic fields over a thickness δ, see equation (2.2), while the initial mean scalar distribution is a discontinuity smoothed enough to avoid the Gibbs phenomenon, as in equation (2.3).

function $p(x)$, defined as

$$p(x) = \frac{1}{2}\left[1 + \tanh a\frac{x}{L}\tanh a\frac{x - L/2}{L}\tanh a\frac{x - L}{L}\right], \tag{2.2}$$

has been chosen to allow a smooth transition between the two regions (in equation 2.2 L is the domain size in the x direction and a is a constant, which is chosen in order to have an initial transition layer that is no larger than the integral scale, $a = 55$). The resulting field is then made divergence-free by a standard projection onto a solenoidal space. These operations ensure the continuity of the flow across the whole domain.

In this study, we consider the interaction of two flows with the same integral scale and different turbulent kinetic energy, so we choose $u_i^{(2)} = u_i^{(1)}/\mathcal{E}^{1/2}$, where $\mathcal{E} = E_1/E_2$ is the imposed initial kinetic energy ratio.

A description of how the presence of different integral scales can influence the turbulent kinetic energy diffusion can be found in Tordella & Iovieno (2006, 2012).

In order to analyse the diffusion of the passive scalar interface across the turbulent kinetic energy gradient, the passive scalar is introduced into the low kinetic energy region of the flow at $t = 0$. To avoid the Gibbs phenomenon, the discontinuity is replaced by a sufficiently smooth transition. The initial condition for the passive scalar θ is thus defined via the same matching function as

$$\theta(x, y_i) = \frac{1}{2}\left[1 - \tanh 2a\frac{x}{L}\tanh 2a\frac{x - L/2}{L}\tanh 2a\frac{x - L}{L}\right], \tag{2.3}$$

By choosing $a = 55$ in equation (2.3), the passive scalar interface is smoothed on a length which is about half the initial integral scale. No passive scalar fluctuation is introduced: the passive scalar concentration is initially uniform in the two isotropic regions, $\theta = 0$ in the high energy region and $\theta = 1$ in the low energy region. Passive scalar variance will be generated by the underlying turbulent flow, see figure 2.2.

The mass, momentum and and the passive scalar transport equation are solved by using a dealiased pseudospectral Fourier-Galerkin spatial discretization coupled with a fourth order Runge-Kutta explicit time integration, as described in chapter 4. The size of the dimensionless computational domain is $4\pi \times (2\pi)^2$ in the three-dimensional simulations. The domain used in the two-dimensional simulation has the same aspect ratio: it is $4\pi \times 2\pi$. For further details on the numerical technique and the initial conditions generation, see Iovieno *et al.* (2001); Tordella & Iovieno (2006); Tordella *et al.* (2012).

We have carried out a numerical experiments with an imposed initial turbulent kinetic energy ratio of 6.7 in both two and three dimensions. In the three-dimensional simulations, we have performed two experiments in which the higher energy turbulent field $u_i^{(1)}$ has an initial Taylor microscale Reynolds number equal to 45, 150 and 250.

The domain is discretized with 256×128^2 grid points in the simulation at $Re_\lambda = 45$, with 1200×600^2 grid points in the simulation at $Re_\lambda = 150$ and with 2048×1024^2 in the simulation at $Re_\lambda = 250$. The two dimensional simulations use a 4096×2048 grid for an initial integral scale Reynolds number equal to about 3000.

In this forst numerical investigation of the passive scalar transport in a shearless energy mixing, the Schmidt number $Sc = \kappa/\nu$ is set equal to one in all the simulations. Schmidt numbers of order one are typical of many transport phenomena in air, from small temperature fluctuations to water vapour transport, Yeung *et al.* (2004).

About 20 initial eddy turnover times have been simulated in two dimensions and ten initial eddy turnover times in three dimensions. We have estimated that, due to the mixing layer growth, the two separate homogeneous and isotropic regions will be destroyed by their interaction after about 30-35 initial eddy turnover times. Directions y_1 and y_2 in this flow configuration remain statistically homogeneous during the decay, so that all the statistics can be computed as plane averages in these directions. Moreover, in two dimensions we have enlarge our statistical sample by ensemble averaging also on fifty repetitions of the simulation with different but statistically equivalent initial conditions.

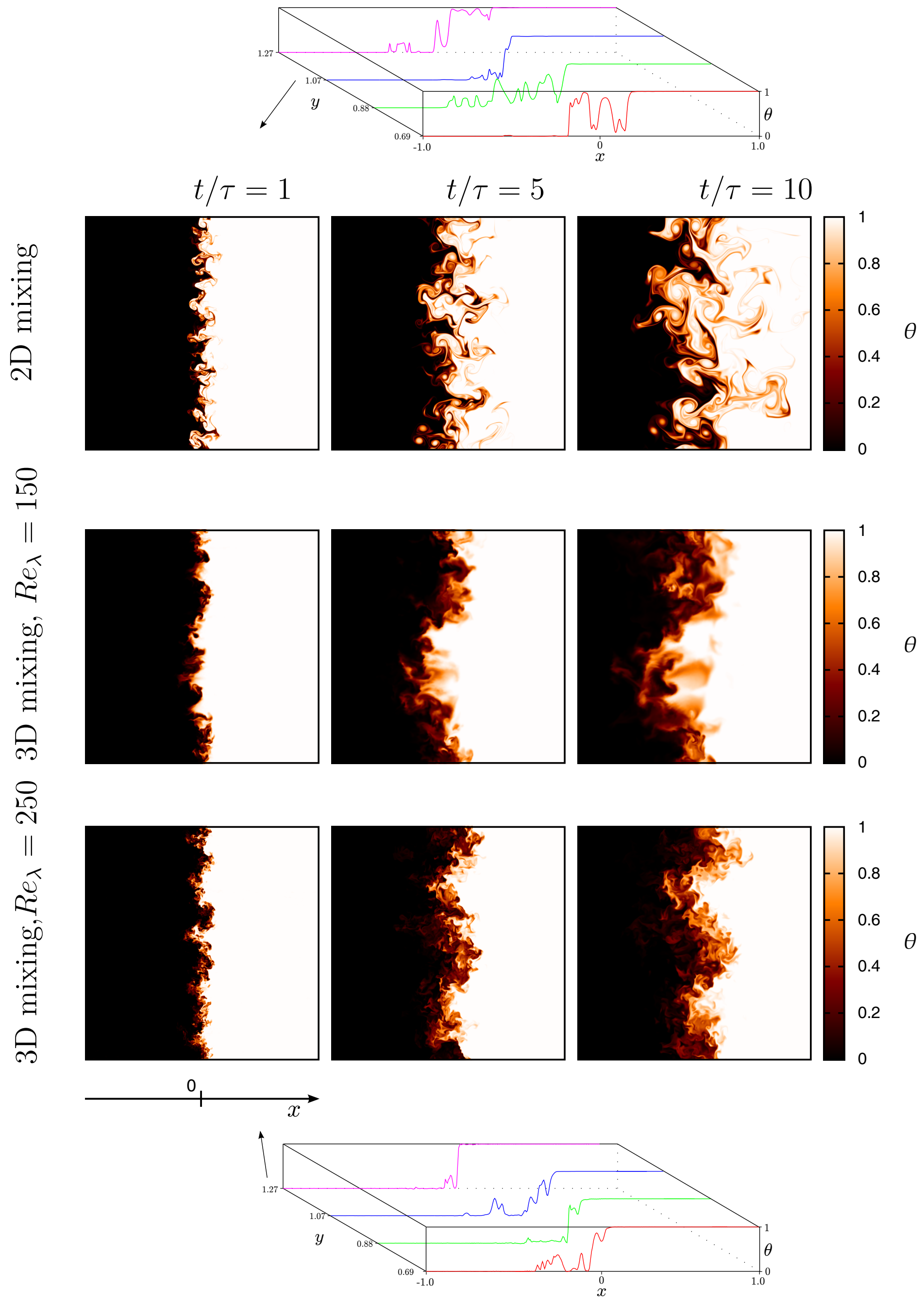

Figure 2.2. Visualization of the scalar field in a plane within the central part of the computational domain. The high turbulent energy velocity field is on the left of each image. The three different instants correspond, from left to right, to t/τ = 1,5,10, respectively. τ is the initial eddy turnover time of the high energy region. The three-dimensional simulation has an initial R_λ equal to 150 and 250 in the high energy isotropic region and 60, 100 in the low energy region. The initial value of the energy ratio of the two interacting isotropic turbulences is 6.7. The insets show the concentration along few lines in the direction parallel to the mean gradient at $t/\tau = 1$.

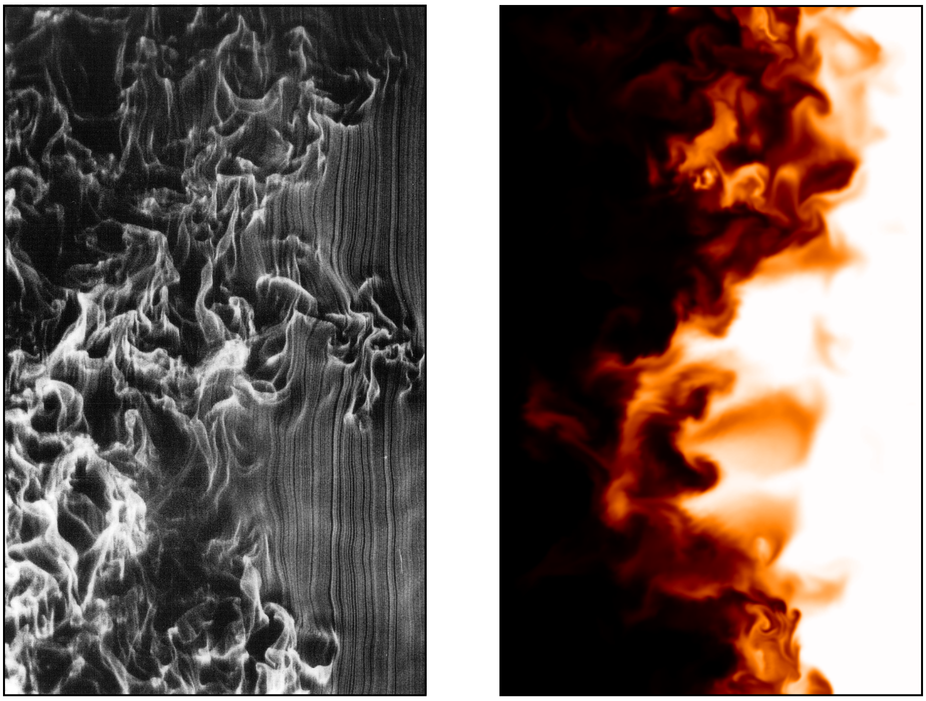

(a) Jayesh & Warhaft laboratory experiment

(b) Present numerical experiment

Figure 2.3. Comparison between a laboratory visualization by Jayesh & Warhaft (from Jayesh & Warhaft (1994), figure 8(a)) and present simulation: (a) Smoke-wire (streaklines) visualization of the shearless mixing layer without thermal stratification, wind tunnel experiment, side view at a distance from the grid equivalent to our time evolution at $t/\tau \approx 9$. The flow is from top to bottom and $Re_\lambda = 130$ Jayesh & Warhaft (1994). The energy ratio can be estimated as of order 10^2 because the turbulence level in the part of the flow out of the grid (on the right in this picture) has a ratio velocity rms/mean velocity less than 0.25%. It should be noted that this visualization is not exactly the equivalent of the one in panel (b). In fact, the equivalent view would have been a tunnel cross section at a constant x. (b) Pseudocolor of the passive scalar concentration along the mixing layer in a central portion of the domain at $t/\tau = 10$, initial $Re_\lambda = 150$, the initial energy ratio is equal to 6.7.

Grid	3D Mixing $Re_\lambda = 45$ $128^2 \times 256$		$Re_\lambda = 150$ $600^2 \times 1200$		$Re_\lambda = 250$ $1024^2 \times 2048$		2D Mixing $Re_\lambda \approx 250$ 2048×4096	
t/τ	Re_λ	$\nabla\theta$ [m^{-1}]	Re_λ	$\nabla\theta$ [m^{-1}]	Re_λ	$\nabla\theta$ [m^{-1}]	Re_ℓ	$\nabla\theta$ [m^{-1}]
0	45	7.51	150	7.65	250	8.49	3076	13.50
1	40	3.11	136	3.12	231	2.85	4762	4.44
5	34	1.20	120	1.32	199	1.25	10200	1.21
10	32	0.80	110	0.92	185	0.89	16297	0.71

Table 2.1. Passive scalar gradient and instantaneous Reynolds number for all the simulations: $Re_\lambda = u'\lambda/\nu$, $Re_\ell = u'\ell/\nu$, where λ is the Taylor microscale and ℓ the integral scale.

2.2 Passive scalar transport across the interface

The initial conditions for the velocity field produce a kinetic energy gradient in the direction of inhomogeneity (x) as already shown in many experiments (e.g. Veeravalli & Warhaft (1989); Tordella & Iovieno (2006, 2011)). Outside this inhomogeneous region, the kinetic energy shows a power law decay, with exponents approximately equal to -1.2, for both $Re_\lambda = 150$ and $Re_\lambda = 250$ in three dimensions, while no significant energy decay is observed in two dimensions due to the inverse cascade. In both cases, the initially imposed energy ratio between the two homogeneous regions is almost preserved during the time evolution of the flow.

In all flow configurations, the velocity mixing layer was observed to be highly intermittent and the velocity fluctuations in the x direction have large skewness and kurtosis, see Veeravalli & Warhaft (1989); Tordella & Iovieno (2006); Tordella *et al.* (2008). Across the mixing layer the second, third and fourth velocity moments collapse using a single lengthscale; the mixing width δ_E, conventionally defined as the distance between the points with normalized energy $(E(x,t) - E_2(t))/(E_1(t) - E_2(t))$ equal to 0.75 and 0.25. In this paper, we focus on the passive scalar dispersion through the shearless mixing layer. For the velocity statistics refer to Veeravalli & Warhaft (1989); Tordella & Iovieno (2006); Tordella *et al.* (2008).

As it has been already observed, one-point statistics of the velocity fluctuations along the inhomogeneous direction indicate the presence of a highly intermittent layer which is shifted with respect to the centre of the mixing region toward the lower energy flow Veeravalli & Warhaft (1989); Tordella & Iovieno (2006); Tordella *et al.* (2008). This is marked by a single large peak

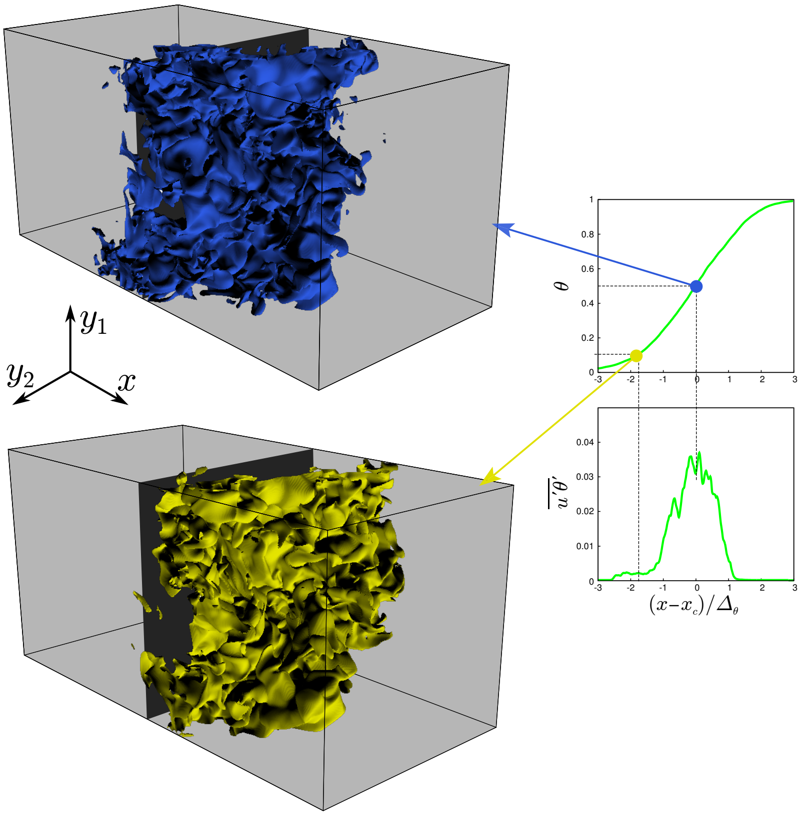

Figure 2.4. Visualization of the isosurfaces $\theta = 0.1$ and $\theta = 0.5$ of the scalar field at $t/\tau = 4$, where τ is the initial eddy turnover time of the high energy turbulence) in a portion of the domain – one quarter of each dimension is shown – in the three dimensional mixing at $Re_\lambda = 250$. The low energy turbulence is on the left of each image, the grey plane in the background is the initial position of the interface.[External MEDIA: file **isosurface__passiveScalar.mp4** shows the temporal evolution of a scalar concentration isosurface at $\theta = 0.75$.]

of both the skewness and the kurtosis. The intensity of the intermittency and the penetration of this layer are controlled by the kinetic energy gradient and, when present, by the integral scale gradient. The Reynolds number has a minor effect on the large-scale velocity intermittency but has a major impact on the level of small scale intermittency Tordella & Iovieno (2011).

The main results of this work is that, in contrast with the velocity transport case, the scalar field is characterized by the presence of the two intermittent fronts which are located at the sides of the interaction region between the two isotropic fields. These fronts can be identified by the peaks of the spatial distributions of the higher order moments of both the scalar field and its derivatives. These two layers delimit a high scalar variance region which is generated by the the temporal smoothing of the initial steep scalar gradient, which we identify as our initial thin interface.

Mean scalar diffusion and mixing growth

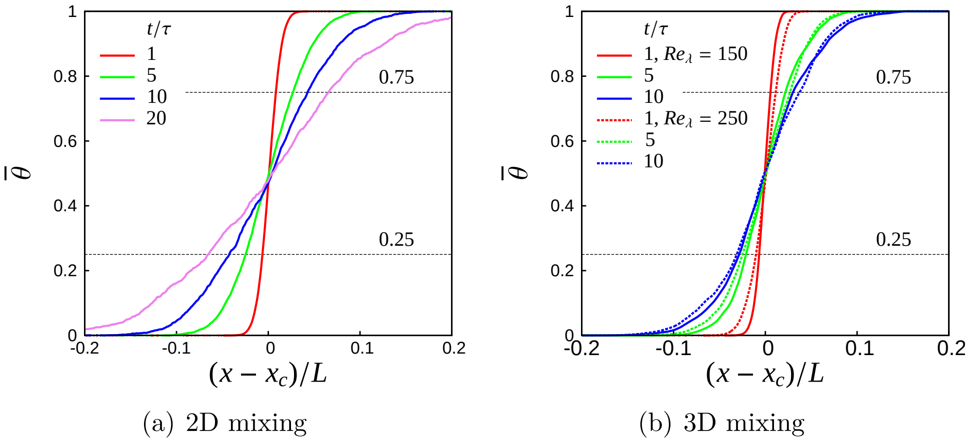

(a) 2D mixing

(b) 3D mixing

Figure 2.5. Mean scalar profiles inside the mixing layer: (a) two dimensional flow, (b) three dimensional flow. The initial energy ratio E_1/E_2 is equal to 6.7 in both cases. L is the domain size in the x direction and x_c the centre of the mixing layer. The dashed horizontal lines indicates $\overline{\theta} = 0.25$ and $\overline{\theta} = 0.75$.

A visualization of the time evolution of the passive scalar concentration at three different instants is shown in figure 2.2. The passive scalar interface, which initially separates the low energy region with passive scalar concentration $\theta = 1$ (on the right of the figures) from the high energy region with passive scalar concentration $\theta = 0$, is spread by turbulent eddies and a passive scalar mixing region with high variance is generated. Scalar concentration isosurfaces are highly corrugated by the advecting velocity eddies as can be seen in figure 2.4, which shows the two surfaces where the passive scalar concentration is half of the maximum value (blue surface) and where the scalar is quite absent and its concentration is only 10% of the maximum value (yellow surface). These two surfaces are very similar, no difference in the corrugation structures is visually evident. From the inspection of the visualization images in figure 2.2, it should be noted that one cannot deduce the direction in which the scalar is diffusion and mixing.This highlights a symmetry of the system that is associated to the fact that by overturning the initial condition for the scalar field, the concentration field becomes equal to the complement to 1 of the field before the exchange. From these considerations, it can be noted that

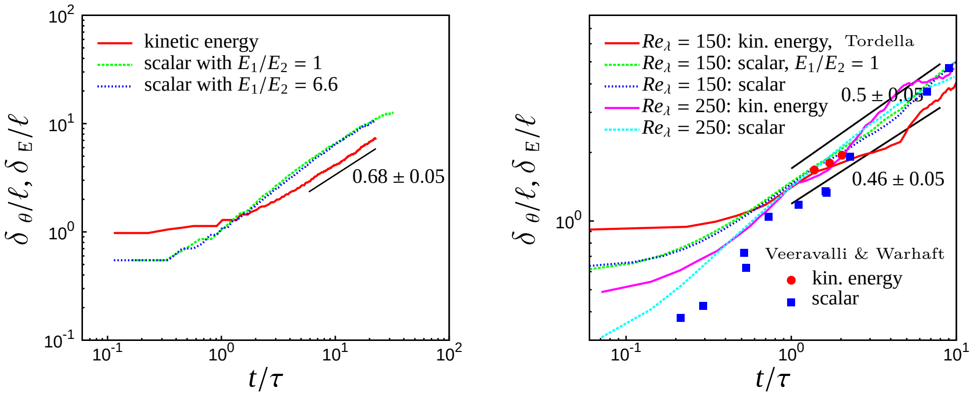

(a) 2D mixing

(b) 3D mixing

Figure 2.6. Interaction layer thickness, normalized with the initial integral scale ℓ. The scalar layer thickness δ_θ is defined as the distance between the points where $\overline{\theta}$ is equal to 0.25 and 0.75. The energy layer thickness is defined as the distance between the points where the normalized turbulent kinetic energy $(E - E_2)/(E_1 - E_2)$ is equal to 0.25 and 0.75 as in Tordella *et al.* (2008). The exponents of the power law fitting of the scalar thickness growth are indicated. The accuracy of the exponents is about 10%. The same mixing length growth can be observed in the absence of the kinetic energy gradient $(E_1/E_2 = 1)$. Experimental data are from the wind tunnel experiments by Veeravalli & Warhaft (1989) and Veeravalli & Warhaft (1990) with $E_1/E_2 = 7$. It should be noted that in this last work the authors propose an exponent of 0.34 for the final stage of the scalar dispersion.

an inference about possible symmetric arrangements of statistical quantities can be drawn.

In figure 2.2, the insets shows the concentration distribution along a direction normal to the interface (but aligned with the mean scalar gradient). In the central part of the distributions, some resemblance can be seen with the features called ramp-and-cliff, first noticed in the 1970's by Gibson, Antonia, Sreenivasan and others (see Warhaft (2000) for details). These features are considered due to the presence of large scale straining motions with the direction of compression approximatively aligned with the mean scalar gradient. This situation is also met in the present shearless mixing.

The width of the mixing region can be measured by considering the mean passive scalar distributions (figure 2.5). The passive scalar mixing layer thickness δ_θ is defined, in analogy with the energy layer thickness δ_E, as the distance between the points with means passive scalar $\overline{\theta}$ equal to 0.75 and 0.25.

After an initial transient of about one eddy-turnover time, the time evolution of these interaction widths follow a trend similar to those observed for the self-diffusion of the velocity field with the same dimensionality, and a stage of

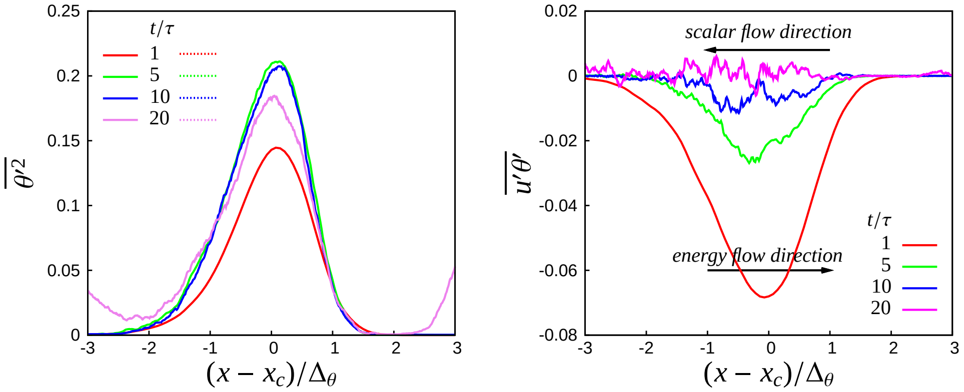

(a) 2D mixing, scalar variance (b) 2D mixing, scalar flux

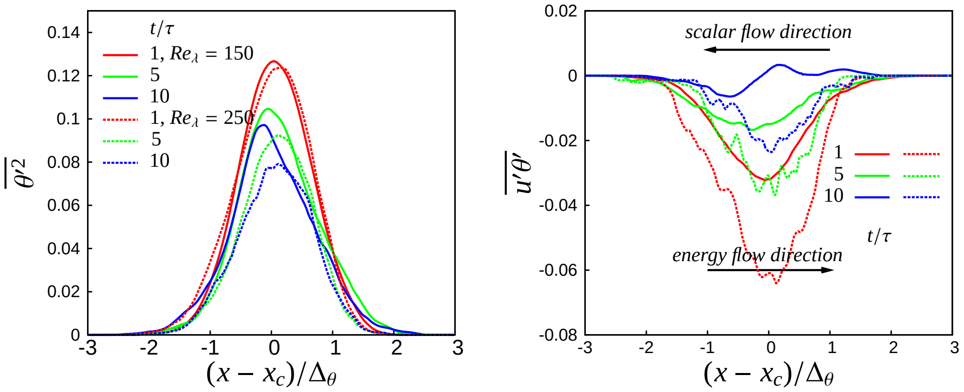

(c) 3D mixing, scalar variance (d) 3D mixing, scalar flux

Figure 2.7. (a,c) Scalar variance in the simulations in two and three dimensions. (b,d) Scalar flux $\overline{u'\theta'}$ in the simulations in two and three dimensions. The arrows indicate the scalar and energy flow directions. The initial energy ratio is $E_1/E_2 = 6.7$ in all simulations; δ_θ is the passive scalar mixing thickness which increases in time as shown in figure 2.6. According to our estimate, for the three-dimensional, $\delta_\theta \sim t^{0.5}$ at $Re_\lambda = 250$

evolution with a power law scaling of the scalar mixing thickness is reached in both two and three dimensions. However, the time scaling of the growth of the interaction width is superdiffusive in two dimensions ($\delta_\theta \sim t^{0.7}$), while it is very slightly subdiffusive in three dimensions ($\delta_\theta \sim t^{0.46}$ at $Re_\lambda = 150$ and $\delta_\theta \sim t^{0.5}$ at $Re_\lambda = 250$), see figure 2.6. Superdiffusive dispersion seems to be characteristic of two dimensional flows as observed in Hansen *et al.* (1998). As opposed to three-dimensional turbulence, in two dimensions vortices tend to live much longer than their turnover time thus enhancing the transport.

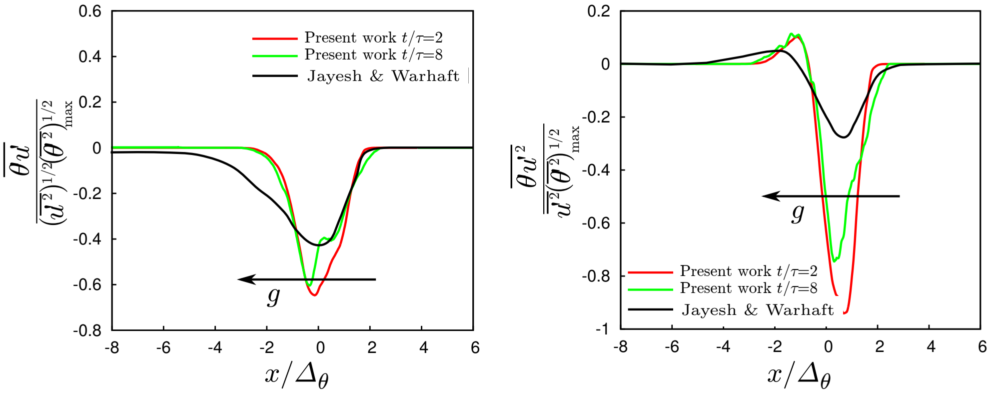

(a) 3D mixing, $Re_\lambda = 150$ (b) 3D mixing, $Re_\lambda = 150$

Figure 2.8. (a) Scalar flux and (b) third order mixed moment: comparison between the present simulation with an initial Reynolds number $Re_\lambda = 150$ and laboratory data by Jayesh & Warhaft (1994) at $Re_\lambda = 130$ obtained in a shearless mixing in presence of a mild stable temperature stratification (the direction of the gravitational acceleration is indicated by the arrow). In the considered measurement stations $x/M = 32$ and the Richardson number is equal to 0.77.

The same mixing growth can be observed in the absence of the kinetic energy gradient (that is, $E_1/E_2 = 1$) and thus the mixing width does not seem to be influenced by the presence of the energy gradient.

The three dimensional simulations show a fair agreement with the wind tunnel experiments on the scalar diffusion from a line source in a shearless mixing Veeravalli & Warhaft (1990), in particular considering the evolution, after an initial transient, of the scalar and kinetic energy interaction layers thickness normalized with the integral scale ℓ, see figure 2.6. The agreement is better for higher Re_λ values. An other similarity can be found in the asymmetry of the flux, that decays rapidly in the low energy region as in Jayesh & Warhaft (1994); Veeravalli & Warhaft (1990), see figure 2.7 (d - f)

2.2.1 Statistics

A mixed region with high passive scalar variance is immediately generated in the centre of the interaction layer. In the three-dimensional flow, the passive scalar variance reaches its maximum after less than one eddy turnover time and, after that, it slowly decreases. In the following 10 eddy turnover times, about 20% of the variance present at $t/\tau = 1$ is lost. In two dimensions,

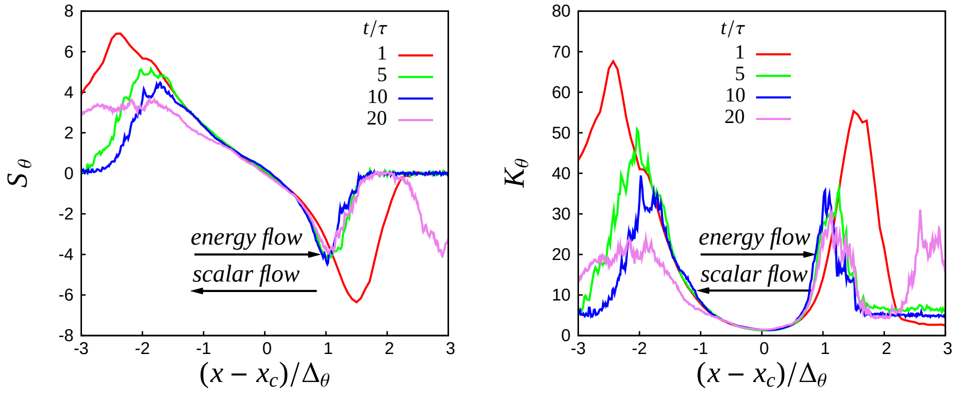

(a) 2D mixing (b) 2D mixing

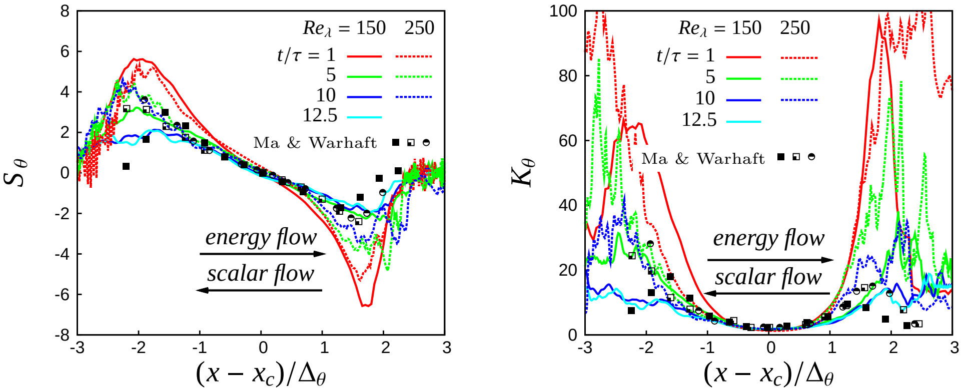

(c) 3D mixing (d) 3D mixing

Figure 2.9. (a,c) Passive scalar skewness distribution and (b,d) passive scalar kurtosis distributions. All the simulations have an initial energy ratio $E_1/E_2 = 6.7$. The vertical dashed lines indicate the position of the maximum of intermittence at the end of the simulation. The arrows indicate the passive scalar and energy flow directions which are opposite in this simulations. Leaving aside the sign, the distributions remain unchanged when the passive scalar mean gradient is concurrent with the energy gradient. Symbols in parts (c) and (d) are from the thermal mixing in grid experiments by Ma & Warhaft (1986) at $Re_\lambda = 32.7$: ■ mandoline heater, $x/M = 62.4$, □ toaster heater, $x/M = 62.4$, • toaster heater, $x/M = 82.4$.

the passive scalar flow is almost twice as large and the initial variance generation last longer: the maximum is attained later and is about 50% higher. Notwithstanding the presence of the energy gradient, the mean passive scalar and passive scalar variance profiles are almost symmetric, see figures 2.5 and

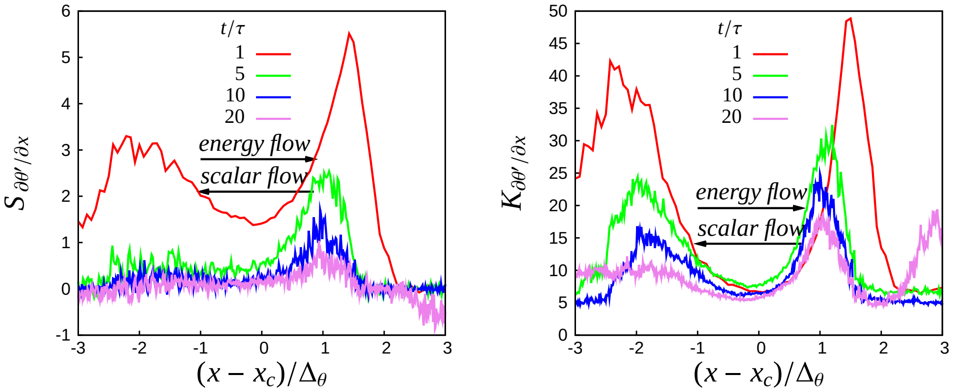

(a) 2D mixing (b) 2D mixing

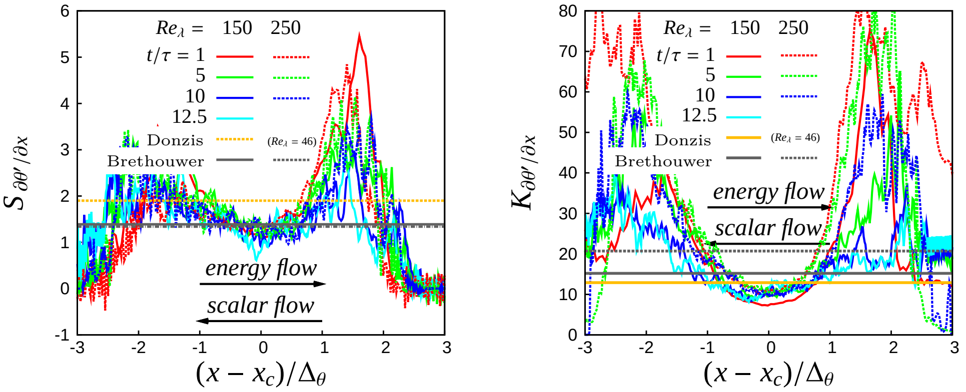

(c) 3D mixing (d) 3D mixing

Figure 2.10. (a,b) Skewness and (c,d) kurtosis distributions of the derivative of the passive scalar fluctuation in the inhomogeneous direction x. All the simulations have an initial energy ratio $E_1/E_2 = 6.7$. The vertical dashed lines indicate the position of the maximum of intermittence at the end of the simulation. The arrows indicate the passive scalar and energy flow directions which are opposite in this simulations. Leaving aside the sign, the distributions remain unchanged when the passive scalar mean gradient is concurrent with the energy gradient. The Taylor microscale of the homogeneous flow comparison data in parts (c,d) is equal to 140 and 240 in the data by Donzis & Yeung (2010) and to 46 in the data by Brethouwer *et al.* (2003).

2.7.

The presence of the turbulent energy gradient is instead felt on the distribution of higher order moments as the passive scalar skewness and kurtosis shown in figures 2.9 and in the scalar flux shown in figure 2.7.

In the central region the values of S and K tend to the ones of a gaussian distribution ($S = 0$, $K = 3$), while on the mixing edges they present two peaks. This means that, in contrast with the velocity field in which there is only one intermittent layer Tordella & Iovieno (2006); Tordella *et al.* (2008), the third and fourth order moments show the presence of two intermittent fronts at the border of the mixing region, see figure 2.9 and 2.10. It's interisting to observe that, through the normalization of the x coordinate with the mixing layer thickness δ_θ, for different time and also for different Re_λ such peaks collapse in the same position (empirical indication of self-similarity). In fact, this behavior can be observed also with very different Re_λ. Data from Ma and Warhaft Ma & Warhaft (1986) with low Re_λ (≈ 30), without kinetic energy gradient show the presence of those two intermittent front in the same position of the normalized coordinate, see figure 2.9, panels (c - d).

Intermittent fronts (highly non-gaussian regions, with large values of S and K) are associated to the presence of inhomogeneity in the scalar field, in particular where the scalar gradient quickly changes and assumes high values. This is related to the formation of an interface with crests and troughs shown in both in figure 2, and in following figure 10, where the formation of this kind of interface will be discussed in an extremely simplified case, see section 3.3 for details. The existence of a kinetic energy gradient is instead responsible of the asymmetries in the distributions of S and K.

In the firsts eddy turnover times the intermittency at the edges of the mixing layer is very intense, and then decreases as the system decays, with the dissipation of kinetic energy and the thicketing of the mixing layer: the inomogeneity intensity decrease, as the same occurs at the field that transports the scalar. As a conseguenge not only the intermittency levels decrease, but also the scalar flow tends to disapear, see figure 2.7 panels (b - d). In three dimensions, because of the faster energy decay, the intermittency reduction is evident, above all when the $Re_\lambda = 150$. In this case, the peaks in the distributions of skewness and kurtosis present the same levels in two and three dimensions after about one eddy turnover time but, after ten eddy turnover times, in two dimensions the peaks of skewness and kurtosis are twice as high.

In Ma & Warhaft (1986) asymmetries of S and K is due to the formation of scalar fluctuations in the high concetration region that arise during the experimental formation of the scalar discontinuity. In present study the observed asymmetries, that can be observed in the firsts eddy turnover times, is instead correlated with the presence of a kinetic energy gradient. In fact, considering the crests and troughs interface, the asymmetries are formed due to the different mixing intensity in the edges of the layer: next to the crests (high energy) the greater velocity fluctuations concur to enhance the scalar mixing, and the concentration is more homogeneous, viceversa next to the troughs (low energy region) this process is slower, and intermittency survives longer. A second effect present in two dimension is the different depth of penetration: after about 5 initial eddy turnover times the depth of penetration is about $2\delta_\theta$ in the high energy region and about δ_θ in the low energy region.

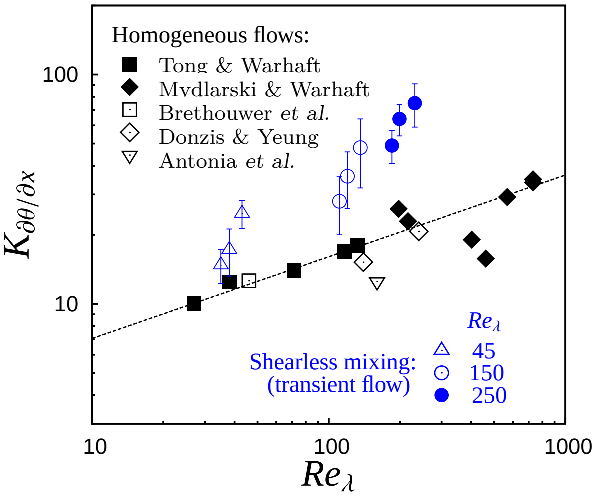

Figure 2.11. Kurtosis of the scalar derivative as a function of Re_λ. The blue symbolds represent the maximum of the kurtosis in the intermittent fronts at $t/\tau = 1$, 5 and 10; the black symbols are data for homogeneous flows by Tong & Warhaft (1994), Mydlarski & Warhaft (1998), Brethouwer *et al.* (2003), Donzis & Yeung (2010) and Antonia *et al.* (1986).

Intermittency is not limited to large scale passive scalar fluctuations, but is quickly spread to small scale fluctuations, as can be inferred from the skewness and kurtosis of the passive scalar derivative in the inhomogeneous direction x, which are shown in figure 2.10(a-b). Two peaks of large intermittency can be seen in correspondence of the two intermittent fronts since $t/\tau = 1$. However, their time evolution is different from the one seen for large scale passive scalar fluctuations: the peaks always decay in time, but now small scale intermittency lasts longer in the three dimensional case. Because the inverse cascade dramatically removes energy from the small scales, in two dimensions the peak of the derivative skewness in the front facing the high energy region has almost vanished after ten eddy turnover times while in the front facing the low energy side it is about half the one present in three dimensions.

The transient scalar derivative moments levels obtained in the two fronts are much higher than the ones observed in isotropic turbulence with a uniform mean scalar gradient at similar Reynolds numbers. For example, Donzis and Yeung Donzis & Yeung (2010) in their numerical simulations obtained a scalar

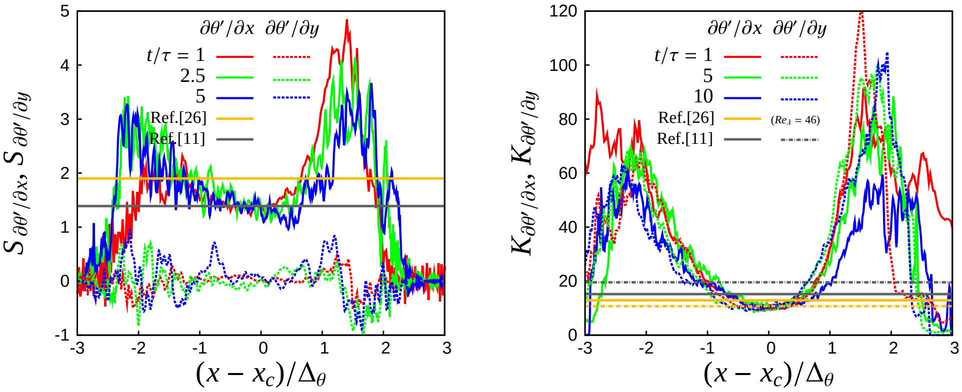

(a) (b)

Figure 2.12. Comparison between the skewness and kurtosis of the passive scalar derivatives $\partial\theta/\partial x$ and $\partial\theta/\partial y_1$ in the directions parallel and normal to the energy gradient in the three dimensional mixing at $Re_\lambda = 250$. All present simulations have an initial energy ratio $E_1/E_2 = 6.7$. The homogeneous flow data by Donzis & Yeung (2010) have a Taylor microscale Reynolds number equal to 240, the data by Brethouwer *et al.* (2003) have a Taylor microscale Reynolds number equal to 46.

skewness equal to 1.39 at $Re_\lambda = 140$ and 1.34 at $Re_\lambda = 240$ with a normalized mean scalar gradient equal to 1. In our experiment, where also the initial mean scalar gradient across the interface was set equal to 1, between $t = 1\tau$ and $t = 5\tau$, we observe a skewness which is in the range 4 - 5.5 at $Re_\lambda = 250$ and between 3 - 5.7 at $Re_\lambda = 150$. An even greater departure can be observed in the derivative kurtosis, whose extreme values can be twice the values in homogeneous turbulence as shown in figure 2.11, where our data are compared with the set of data with derivative parallel to the mean gradient which are included in figure 3 of the review by Warhaft Warhaft (2000),as well as in Brethouwer *et al.* (2003); Antonia *et al.* (1986); Donzis & Yeung (2010), see also table 2.1.

In a laboratory experiment of a decaying grid turbulence with a uniform scalar gradient at $Re_\lambda = 580$, Warhaft Warhaft (2000) and Mydlarski and Warhaft Mydlarski & Warhaft (1998) found a passive scalar derivative kurtosis close to 20 in the presence of a mean passive scalar gradient equal to about 3.6 K/m (temperature field) after about one eddy turn over time.

The difference becomes more marked as the Reynolds number increases. The intermittency of the two fronts is enhanced by a Reynolds number increment in a way similar to the linear dependence of the intermittency of temperature fluctuations as a function of the Reynolds number oberved in a

Rayleigh-Bernard convection Emran & Schumacher (2008). This could be a general property of scalar transport. Schumacher observed that the probability density function of the magnitude of the passive scalar gradient increases with the Reynolds number in numerical simulations at moderate Reynolds number Schumacher & Sreenivasan (2005). A higher Reynolds number enables the passive scalar to be more efficiently stirred on all scales leading to an increase of scalar fluctuations and derivative moments.

Simulations in absence of a turbulent energy gradient (i.e., $E_1/E_2 = 1$), not shown in the figures, do not show the asymmetry in the position of the scalar intermittent fronts even if the thickness of the mixing layer follows the same temporal growth.

The passive scalar derivative in the directions normal to the kinetic energy and passive scalar gradients (directions parallel to the mixing) shows a slightly reduced level of intermittency in the two fronts but a much reduced asymmetry in its probability density function as its skewness is lower as shown in 2.12. That is, the passive scalar derivative in the homogeneous direction normal to the mixing process is much less affected by the energy and passive scalar gradients. The Reynolds number and the energy gradient both influence the passive scalar intermittency at small scales Warhaft (2000).

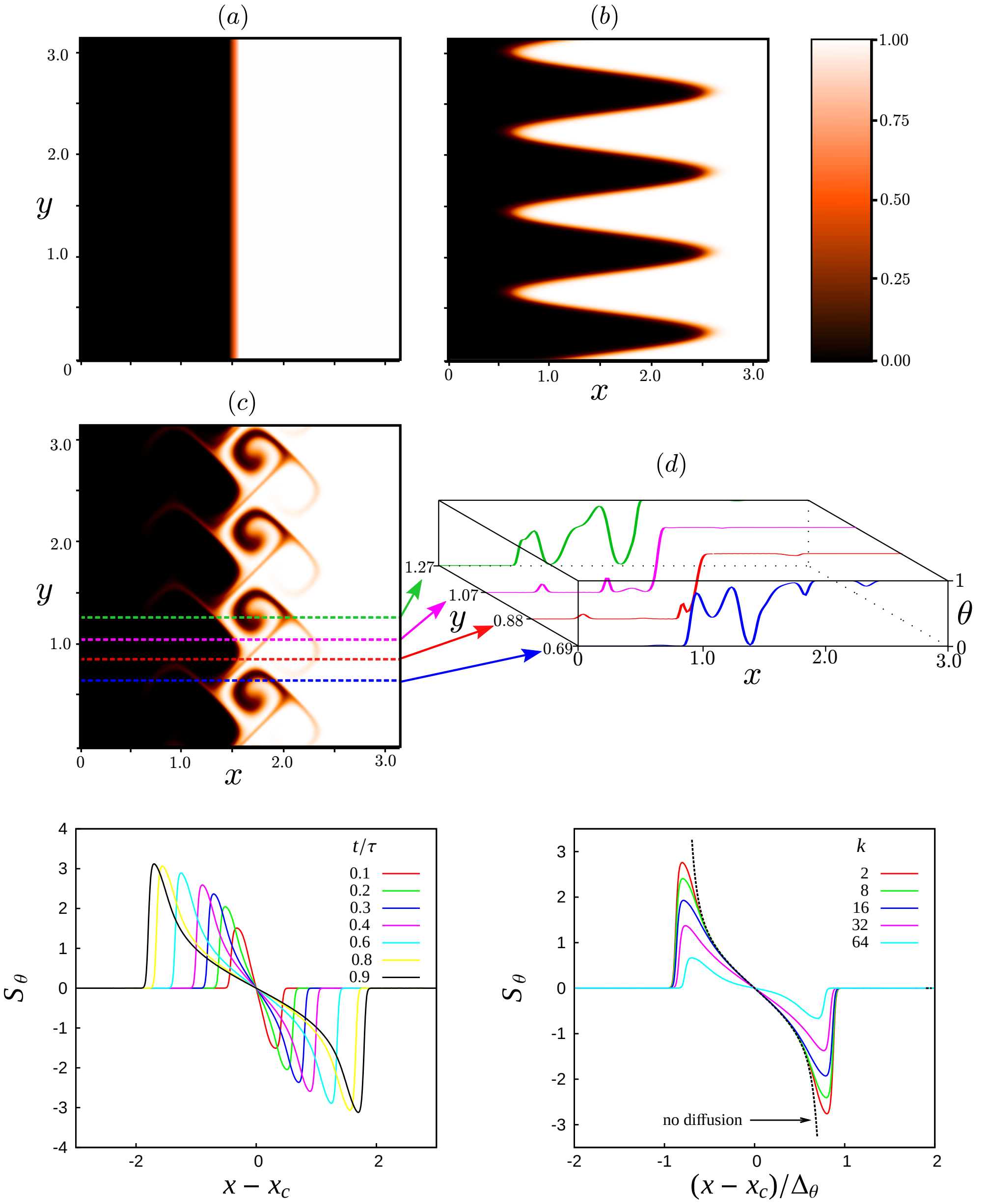

(e)

(f)

Figure 2.13. Scalar advection by a wave perturbation: (a) initial scalar concentration, (b) scalar concentration obtained at $t/\tau = 1$ with the flow field given by equation (2.4), (c) scalar concentration at $t/\tau = 1$ with $u = u_0 \sin(ky - \omega t)$ and $v = u_0 \sin(kx - \omega t)$ ($k = 8$, $u_0 = 1$) $k = 2$, $Re = u_0(2\pi/k)/\nu = 1420$, (d) one-dimensional sections showing the concentration cliffs, (e-f) skewness obtained from the simple wave model: (e) time evolution for a shear wave with wavenumber $k = 2$ ($Re = 5654$), (f) data at $t/\tau = 0.5$ for different wavenumbers.

2.3 Intermittency generated by linear wave perturbations of the interface

Is the generation of a double intermittency layer specific to a turbulent velocity transport? To answer this question we have considered a simple two-dimesional situation where the deformation of the interface, represented by the heaviside function, is due by a single wave with given wave number and frequency. In so doing, the effects of multiple interacting scales on the scalar transport and interface modification will be disregarded. We considered simple velocity waves

$$u_i = u_0 \sin(kx_j - \omega t). \tag{2.4}$$

and verified that only velocity normal to the interface and oscillating in space along a direction parallel to the interface produced an undulating interface.

With reference to the system configuration in figure 2.13, the perturbation effective in undulating the initially planar scalar interface is $u = u_0 \sin(ky - \omega t)$.

At the beginning of the process, we assume that the molecular diffusion is negligible in the direction parallel to the interface, that is $\partial^2\vartheta/\partial y^2$ can be neglected with respect to $\partial^2\vartheta/\partial x^2$. It can then be shown that equation (2.1) has the analytical solution

$$\vartheta(x, y, t) = \frac{1}{2}\left(1 + \text{erf}\left(\frac{x - \int_0^t u(y, t')\mathrm{d}t'}{\sqrt{2\kappa t}}\right)\right) \tag{2.5}$$

where $\kappa = Sc\,\nu$ is the scalar diffusivity. In fig. 2.13, two visualizations of the scalar concentration field from an initially flat interface can be seen. The scalar fields are obtained from two numerical simulation, a first one (panel b) where the velocity field is just $u = u_0 \sin(ky - \omega t)$ and a second one (panel c) where a second wave $v = v_0 \sin(kx - \omega t)$ is added. This second wave becomes effective in modifying the interface since the instant where the projection of the interface profile along the x direction is no more negligible.

In absense of diffusion, the advection of an interface by a wave like the one represented in fig. 2.13 panel (b) leads to the black/white configuration where, at any given distance x from the initial position of the interface, the fraction of space where $\vartheta = 1$ (flow from right) is $p(x)$ and the fraction of space where $\vartheta = 0$ (flow from left) is $1 - p(x)$. In this situation the mean scalar concentration is $\overline{\vartheta} = p$ and the scalar moments can be easily computed as $\overline{\vartheta'^n} = p(1-p)[(1-p)^{n-1} - (-p)^{n-1}]$. The scalar variance is maximum in the centre and the modulus of all normalized moments increases with the distance from the centre. In presence of diffusion, the situation is as depicted in figure 2.13 for the simple shear wave represented in panel (b). Diffusion smooths out the interface discontinuity and reduces large deviations from the mean value, thus limiting the maximum skewness and kurtosis. This effects is much more visible at higher wavenumbers which have a lower effective Reynolds number.

One could expect that the cumulative effect of many basic eddy patterns with different scales (wavenumbers) could lead to a fractal corrugation of the surface with higher intermittency. As shown in Vucelja *et al.* (2012) for two-dimensional turbulence, the distribution of the isoscalar contours length has been found to be fractal at scales larger than the pumping but soon become smooth at smaller scale. We think that even such a simple linear model may provide a generic kinematic picture of the scalar interface and of the formation of a double layer where high moments of the scalar oscillation peak. Holzer & Siggia Holzer & Siggia (1994) simulated the mixing of a scalar with an imposed mean gradient in an isotropic turbulent-like flow field and observed that the scalar field has a ramp-cliff structure, i.e. regions of well-mixed fluid with a nearly constant scalar concentration bounded by steep cliffs. The ramp-cliff structures are positioned approximately perpendicular to the mean gradient and the visualizations suggest that the cliffs are generated by large-scale straining motions with the direction of compression approximately aligned with the mean scalar gradient. In panel (d) of figure 2.13, one can see that even in this extremely simplified situation a shadow of ramp-cliff behaviour appears.

2.4 Passive scalar spectra across the mixing layer

In this last section, we describe briefly the spectral behaviour of the two and three-dimensional passive scalar trasient transport across the interface bewteen the two isotropic turbulent fields. This is in comparison with the velocity field. In three dimensiosn the velocity field undergoes an intense energy cascade. However, in this study we consider turbulence mixings in temporal decay. This circumstance is complex because the forward cascade in temporal decay is concomitant with the small scale disappearance due to dissipation. In the ten time scales we observe in this set of simulations, the turbulent energy decays more than the 90% ($\mathrm{d}E/\mathrm{d}t \sim t^{-1.2}$ Burattini *et al.* (2006). The inertial range is reduced in width, see fig. 2.14. In two dimension, the dynamics is more complex as the inverse energy cascade is accompanied by the forward enstrophy cascade. In 10 time scales, the total energy decay is still mild: 14% for a global Reynolds number of about 3000 (2048×4096 resolution). We are thus observing the early part of the transient decay.

The situation is the following: after a few eddy turnover times, in the central part of the mixing layer, between the two intermittent fronts, the passive

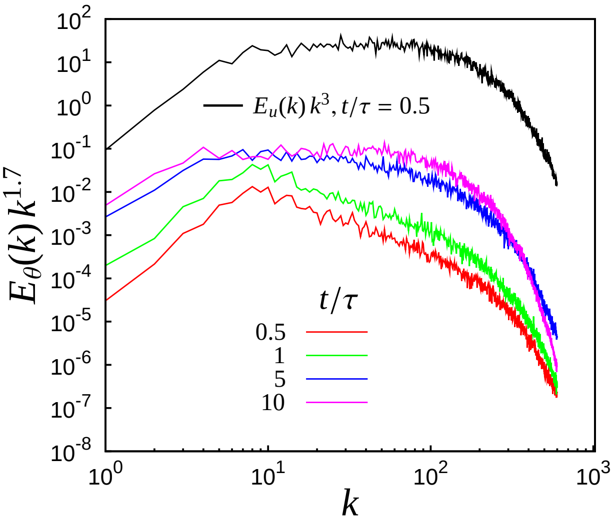

(a) 2D mixing

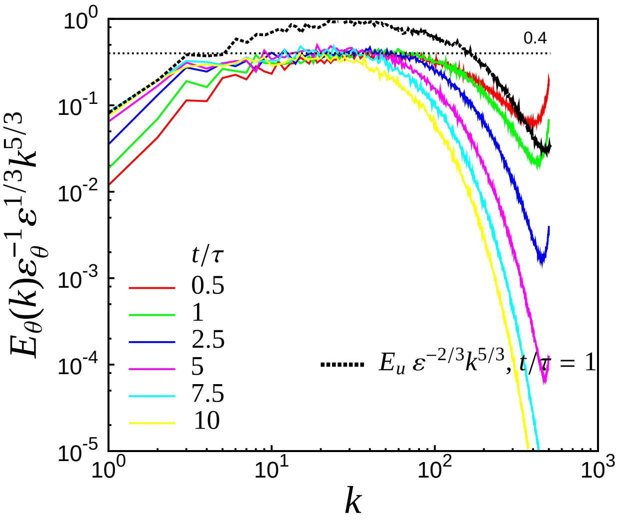

(b) 3D mixing, $Re_\lambda = 250$

Figure 2.14. Compensated passive scalar one-dimensional spectra in the centre of the mixing layer in two (part a) and three dimensions (part c). The black dashed lines reproduce, at one instant, the compensated one-dimensional velocity spectrum in the same position. All spectra have been computed by integrating over the homogeneous directions y_i. All the simulations have an initial energy ratio $E_1/E_2 = 6.7$

scalar fluctuations tend to a slow varying state. As shown in figure 2.7(a,c), the variance in the centre of the mixing region decays very slowly even in the

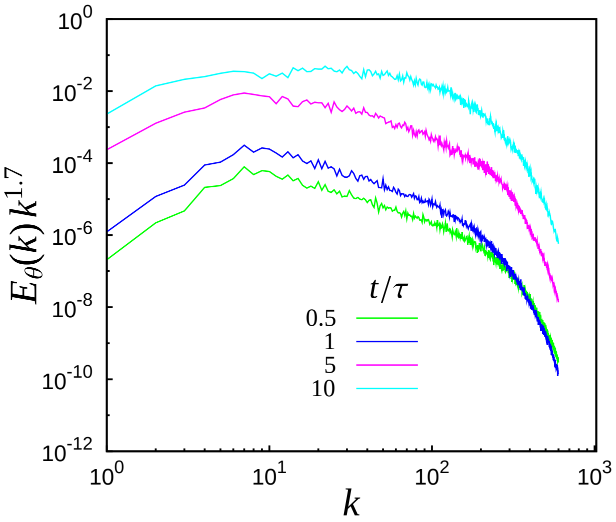

(a) 2D mixing

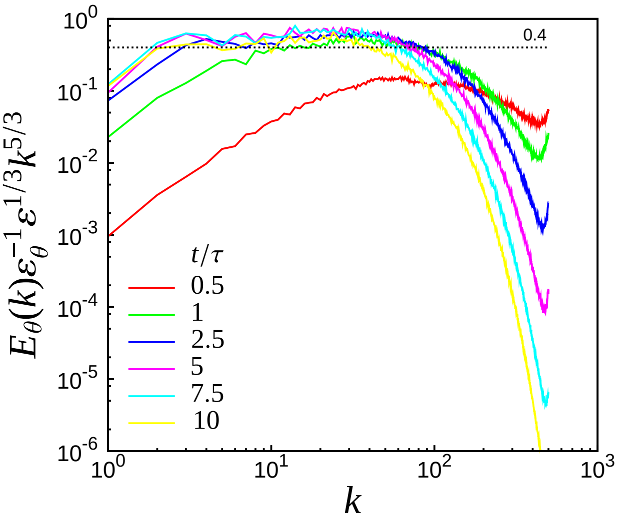

(b) 3D mixing

Figure 2.15. Compensated passive scalar one-dimensional spectra at a fixed position $(x - x_c)/\ell(0) = 1.5$ $(x = x_c + 1.5\ell(0))$. During the transient, the mixing reaches this position, so that the normalized positions $(x - x_c)/\delta_\theta$ is about 1.5, 1.25, 0.5 and 0.25 for t/τ equal to 0,1,5,10 respectively in the three dimensional mixing at $Re_\lambda = 250$. $\ell(0)$ is the initial integral scale. All simulations have an initial energy ratio $E_1/E_2 = 6.7$

three-dimensional flow, which has a fast kinetic energy decay of the underlying flow (see Tordella *et al.* (2008)). In figure 2.14, compensated one-dimensional passive scalar spectra in the centre of the mixing layer are shown. They show a full range of scales just after one eddy turnover time. The spectra in figure 2.14 have been compensated by their inertial range exponents. In the three dimensions, the inertial range scaling $k^{-5/3}$ has been used, Watanabe & Gotoh (2007). The inertial range seems to be wider for the passive scalar fluctuations than for the velocity fluctuations, a feature already observed Mydlarski & Warhaft (1998); Lee *et al.* (2012). In two dimensions, the passive scalar exponent in the inertial range at the end of the transient is about -1.7, which is roughly one half of the -3 exponent of the velocity field and is far from the k^{-1} inertial range scaling of homogeneous and statistically stationary flows (see, e.g., Bos *et al.* (2009); Gotoh *et al.* (2000, 2011)). In three dimensions, the difference between passive scalar and velocity exponents is very mild and both tend to approach the homogeneous turbulence scaling. However, the passive scalar spectrum seems to show a wider inertial range region, a feature which has been observed also in homogeneous flows at moderate Reynolds numbers, see Mydlarski & Warhaft (1998); Danaila & Antonia (2009).

We observe, that for the present three dimensional fields the inertial range scaling exponent for the velocity field is lower than the one of the passive scalar field as previously noted by Warhaft (2000); Danaila & Antonia (2009); Zhou *et al.* (2002). In particular, in homogeneous isotropic turbulence at $Re_\lambda = 250$, Danaila & Antonia (2009) found inertial range exponents equal to 1.58 and 1.62 for velocity and passive scalar fields, respectively. In the present three dimensional numerical experiment, the centre of the mixing layer is characterized by the emerging of an inertial range where the exponents can be estimated as 1.5 (for the velocity field) and 1.62 (for the passive scalar field) at $Re_\lambda = 250$. Following Danaila & Antonia Danaila & Antonia (2009) and Lee *et al.* Lee *et al.* (2012), we have tried to obtain a relation between the spectral exponent of the scalar and velocity fields. With comparison with the estimations by these authors, $m_\theta = 5/6 + m_u/2$, where m is the modulus of the spectral exponents, we found out $m_\theta = 0.57 + 0.67 m_u$. The constant accuracy is 0.57 ± 0.11 and 0.67 ± 0.07.

For three-dimensional flows we found good consistence in the Obukhov-Corrsin constant C_θ Sreenivasan (1996), finding values around the expected 0.4, especially in the $Re_\lambda = 250$ case in the center of the mixing layer, where the scalar fluctuations are well developed. At the boundary of mixing region, the costant value is higher, about 0.5, due to the higher inhomogeneity both in scalar than in kinetic energy fields. For the two-dimensional case we found that the relative Obukhov-Corrsin normalization Bos *et al.* (2009); Gotoh *et al.* (2000) is less suitable to compute C_θ: the exponent we found is -1.8 ± 0.2, different from what expected (-1 for inertial-convective range,

-1.66 for convective-diffusive range). This is due again from the inhomogeneity of the flow, that is more influential than the three-dimensional case.

As general observation, we may say that the spectra of the passive scalar fluctuations seems to be have an asymptotic behaviour in the mixing region. As the front move towards to the homogeneous regions, the passive scalar spectra increases and its exponent tends to $-5/3$ (see figure 2.15). This -5/3 regime is anyway in basic agreement with studies on passive scalar transport in homogeneous flows. For example, it has been found that such regime appears even in homogeneous shear flows for wavenumbers higher than the crossover shear wavenumber Celani *et al.* (2005).

The situation is different for the two dimensional field, because in this case the spectral exponent inside the transient mixing changes little, $m_u = -3 \pm 0.2$. Reynolds effects here are not visible. For the scalar field, instead, the situation is opposite, the exponent variation is large, from $m_\theta = -2.7$ at $t/\tau = 0.5$ to $m_\theta = -1.7$ at $t/\tau = 10$. Once again, the passive scalar field differs substantially from the transport carrier. We have here a situation partly similar to what observed by Bos *et al.* (2009), see fig.4 therein. In that paper, where HIT forced at small wavenumbers is considered (forward enstrophy cascade), the scalar spectrum shows to be substantially smaller than the velocity one (-1 against -3). On this respect, we should point out that the inhomogeneity and anisotropy effects may limit the decrease of scalar spectral exponent with respect to the velocity exponent. Furthermore, a priori we do not know the length of the transient. It is possible that we are still inside the early part of the transient where the forward cascade has not had time to settle on the asymptotic state. This aspect needs to be considered more in depth with further dedicated experiments.

2.5 Conclusion remarks

In this chapter we have analyzed a set of numerical experiments on the transport of a passive scalar through the interfacial layer separating two decaying isotropic turbulent flows with different levels of kinetic energy, both for 2D and 3D turbulence. The evolution of the passive scalar field has been analyzed by means of one-point statistics and spectra computations.

It has been shown that the diffusion length of the scalar, δ_θ, follows closely the temporal evolution of the self-diffusion of the velocity field, δ_E. In two dimensions the growth of the thickness is faster: $\delta_E \sim \delta_\theta \sim t^{0.68\pm0.05}$, while in three dimensions $\delta_E \sim \delta_\theta \sim t^{0.48\pm0.05}$. At equal times in the transient, the scalar flow can be about twice as large in two dimensions than in three dimensions. Also the scalar variance in the center of the mixed layer is 50%

higher in two dimensions.

A first relevant result obtained concerns the presence of two intermittent fronts in the scalar field, which are located at the edges of the mixing region. Such sublayers have initially very high level of intermittency, which gradually decays in time. In all the considered cases, the fronts move away from the initial position of the interface: the front on the high energy side of the mixing penetrates deeper into it. This asymmetry is milder in the three-dimensional case.

The intermittency is not limited to the large scales, but involves also the small scale. In particular, in three dimension the decay of small scales intermittency is slow, and the derivative kurtosis reach values sensibly higher respect to the two-dimensional case. The large scale intermittency is less affected by dimensionality issues, though the kurtosis is higher in three-dimensions.

To better understand the formation and the evolution of such double intermittent layer, we analyzed the effects on the scalar field generates by a simple wavy perturbations of the interface. The formation of the double layer is once again observed and is promoted by undulations which are normal to the interface and propagate along it. Since in this case the flow field is linear and may contain only one spatial and one temporal scale, we may infer that this behavior is a general dynamic characteristic of the chosen scalar field initial condition, and it is not specific to the turbulent transport.

In the center of the shear-less mixing layer, in three dimensions, the passive scalar and velocity spectra both show an inertial range with an exponent close to $-5/3$. The passive scalar exponent is found to be always a bit larger then the energy exponent, in agreement to previus laboratory experiments in grid turbulence.

In two dimensions, the inertial range energy scaling is close to k^{-3}, while the passive scalar tends to $k^{-1.7}$. At the end of the transient evolution in both cases we observed (10 time scales), we found an exponent value which is closer to the three dimensional $k^{-5/3}$ forward cascade than to the two dimensional k^{-1} Batchelor's scaling In this regard, in our early/midterm transients, we see two possible sceneries: the forward enstrophy cascade is still far from the temporal asymptote, or the presence of inhomogeneity and anisotropy effects can anyway limit the decrease of the passive scalar spectral exponent with respect to the one of the energy.

Chapter 3

Effects of Stable/Unstable Stratification in a Shearless Turbulent Mixing

In nature, the behavior of a fluid system is generally much more complex than the incompressible Navier Stokes equations describe. A wide number of phenomena may occur, some of them due to the turbulent field, some of them altering the flow evolution. In a general case, this two thing are coupled: the flow acts on the external phenomenon (i.e. varying concentrations, deforming surfaces, etc.), and the external phenomenon has a force feedback on the flow field.

This is what happens in stratified flows: in that case the external phenomenon is represented by the density of fluid particles, which tends to a certain equilibrium condition. Contrary to what one might imagine, the equilibrium condition is not lighter fluid particle above / heavier particle fluid below, but is to have constant density at every altitude, i.e. the system tends to organize themselves into layers (strata) of constant density. The vertical variation of the density determines is instead related to the stability conditions: in particular, the stable condition states that the lighter particles have to stand above (ans so density has to decrease with altitude).

The presence of a turbulent fluid motion might changes locally the density, altering this equilibrium: as response, buoyancy forces rise, acting on the flow in order to reach again the equilibrium.

These turbulent flows exist also in the simplest of everyday life: from the simple case of water vapor which is generated by boiling water, to more complex phenomena (the knowledge of which is important to the human life) such as the dispersion of hot exhaust gas of an engine, or the weather. Generally speaking, stratified turbulence is one of the characteristic properties of atmospheric flows: the majority of processes in the atmosphere and in the oceans/sees, such as transfer of water vapour and atmospheric dust, heat exchange, and the formation of clouds and precipitation, are closely tied to the turbulent nature of motion in the atmosphere. Atmospheric turbulence renders an essential influence on the propagation of sound, light, and radio waves. Finally, atmospheric turbulence influences flight conditions for aircraft. As a consequence the knowledge of its characteristics is of great significance for many practical purposes.

Geophysical fluid dynamics has recently become an important branch of fluid dynamics due to increasing interest in the environment. The importance of the study of atmospheric dynamics can hardly be overemphasized. We live within the atmosphere and are almost helplessly affected by the weather and its rather chaotic behavior. The motion of the atmosphere is intimately connected with that of the ocean, with which it exchanges fluxes of momentum, heat and moisture, and this makes the dynamics of the ocean as important as that of the atmosphere. The study of ocean currents is also important in its own right because of its relevance to navigation, fisheries, and pollution disposal.

Stratification in the atmosphere is usually stable above the boundary layer, i.e. a fluid particle which is displaced in the vertical direction tends to return to its initial position. In the local atmosphere dynamics the terrestrial rotation becomes of secondary importance, and the stratification effects dominate (Vallis, 2006; Gill, 1982). In the last decade there has been important advances in understanding of turbulence in the presence of strong stratification. In the context of homogeneous stratified turbulence, it is known (Lin & Pao, 1979; Kimura & Herring, 1996) that initially isotropic turbulence in a stratified fluid rapidly becomes anisotropic, with the formation of pancake-like structures in its interior.

In a typical context, the layer is generated by a lighter flow placed above an heavier one, as the one represented in figure 3.1, where it is shown a visualization of the results of a DNS simulations performed by Chung & Matheou (2012) in a HIT field. In that figure the density is represented trough a color-plot (lighter colors correspond to denser fluid): in the top panel the stratification is almost absent, and density behaves like a passive substance exhibiting ramp-and-cliff structures. On contrary, the bottom panel shows the behavior when the stratification effects are strong: the vertical motions are progressively inhibited and eventually turbulence collapses, forming thin layers ans generating the strata-structure.

As pointed out by Malinowski *et al.* (2013), data from most field campaigns and large-eddy simulations are too poorly resolved to allow to infer the details of the interfacial layer, even if they indicate that, in order to allow for

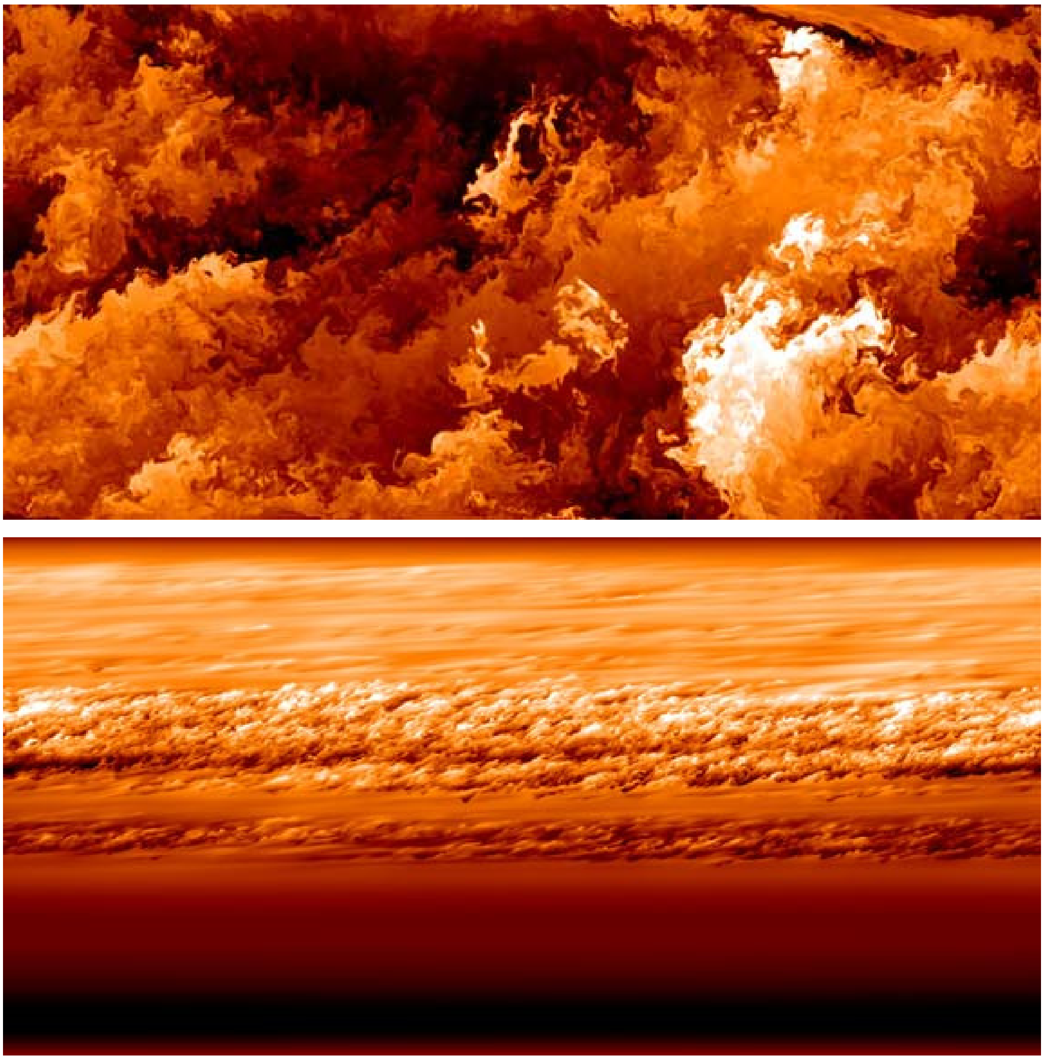

Figure 3.1. Direct numerical simulation of stratified turbulence in shear mixing. Lighter colors correspond to denser fluid. Results by Chung & Matheou (2012)

entrainment, a high level of turbulence must be present.

For this reason, in this work we study the local transport through a clear air/cloud interface through DNS. As our focus is on the dynamics of the smallest scales of the flow which influence the microphysics of warm clouds, we have simulated an idealized configuration to understand, under controlled conditions, some of the basic phenomena which occur at the cloud interface over length scales of the order of few meters. In these conditions, we solve scales from few meters down to few millimeters, that is, we resolve only the small scale part of the inertial range and the dissipative range of the power spectrum in a small portion ($6\ m \times 6\ m \times 12\ m$) of the atmosphere across simplified moist-dry air interface. This allows us to investigate the dynamics of entrainment which occurs in a thin layer at the cloud top, a scale smaller then the scales explicitly resolved in large-eddy simulations of clouds (Moeng, 2000). We focus on two basic aspects of an atmospheric mixing layer: the effect of the presence of a stratification and of a turbulent kinetic energy gradient, without consider other phenomena such as wind shear, evaporation and condensation processes, and radiative cooling which are important in conditions of buoyancy reversal (Mellado, 2010; Mellado *et al.*, 2014). Therefore, our simulations have been carried out by applying the Boussinesq approximation to the Navier-Stokes momentum and energy equations together with an advective-diffusive passive scalar transport equation described in chapter 4.

The results shown in this chapter have been presented in the 32nd UIT Heat Transfer Conference (Gallana *et al.*, 2014*b*, Pisa), in the 4th International TMB Workshop (Gallana *et al.*, 2014*c*, Trieste), in the 67th Annual Meeting of the APS-DFD (Tordella *et al.*, 2014, San Francisco), in the 15th ETC Conference (Gallana *et al.*, 2015*b*, Delft) and in the 68th Annual Meeting of the APS-DFD (Gallana *et al.*, 2015*a*, Boston), and published on the Journal of Physics (Gallana *et al.*, 2014*a*) and in submission on the Journal of Fluid Mechanics (Gallana *et al.*, 2016*a*).

The work is organized as following: we firstly introduce the Boussinesq approximation in the Navier-Stokes equations in section 3.1, and we analyze briefly the new parameters in section 3.2. The details of the physical problem we have considered and of the governing equations are given in section 3.3, providing useful information about chosen parameters and initial conditions. Section 3.4 contains a selection of our main results about intermittency, energy redistribution, transports, and entrainment. Conclusion remarks are in section 3.5.

3.1 The Boussinesq approximation

In order to compute the effect of a fluid stratification we can consider the general Navier-Stokes equations with Archimede's force,

$$\begin{cases} \dfrac{\partial \rho}{\partial t} + \nabla \cdot (\rho \mathbf{u}) = 0 & \text{continuity} \quad (3.1) \\ \rho \dfrac{D\mathbf{u}}{Dt} = -\nabla p + \mu \nabla^2 \mathbf{u} - \rho \mathbf{g} + \left(\lambda - \tfrac{2}{3}\mu\right) \nabla (\nabla \cdot \mathbf{u}) & \text{momentum} \quad (3.2) \\ \rho \dfrac{dE}{dt} = \nabla \cdot (k \nabla \theta) - p \nabla \cdot \mathbf{u} + \dfrac{1}{2}\mu \|\overline{\mathbf{S}}\|^2 + \left(\lambda - \tfrac{2}{3}\mu\right) \nabla \cdot \mathbf{u} & \text{energy} \quad (3.3) \end{cases}$$

where θ is the temperature, E the internal energy per unit mass, μ is the dynamic viscosity coefficient, λ the bulk viscosity coefficient, and k the thermal conductivity coefficient. The fluid is assumed as calorically perfect, so the internal energy can be expressed in terms of temperature:

$$E = c_v \theta$$

where c_v is the constant volume specific heat. In Boussinesq approximation we consider that where the temperature varies, so do the density. In particular, the density can assumed to be constant everywhere, except where it is multiplied by the gravity acceleration $\mathbf{g}$ – so in the buoyancy term. For small variation of temperature (≈ 10 K), temperature and density are linearly dependent:

$$\frac{\rho}{\rho_0} = 1 - \alpha \left(\theta - \theta_0\right), \tag{3.4}$$

where $\alpha \approx 1/\theta_0$ is the constant cubical expansion coefficient. Moreover, μ, k, and c_v can be considered as constants in most of the real fluids.

Under these condition, the continuity equation becomes the same as in canonical incompressible flows:

$$\nabla \cdot \mathbf{u} = 0.$$

In that way also the bulk terms can be neglected. Replacing the density with the temperature, the momentum equation becomes

$$\frac{D\mathbf{u}}{Dt} = -\nabla \left(\frac{p}{\rho_0} + g x_3 \right) + \nu \nabla^2 \mathbf{u} - \alpha \mathbf{g} \left(\theta_0 - \theta\right).$$

The energy equation can be simplified with a dimensional analysis (Drazin & Reid, 1981). We can estimate the order of magnitude of the rate of viscous dissipation and the temperature total derivative considering L as the length scale, V the velocity scale, and $\Delta\theta$ the temperature scale. We have:

$$Q = \frac{1}{2}\mu \left(\frac{\partial u_i}{\partial x_j} + \frac{\partial u_j}{\partial x_i} \right) \approx \mu V^2 L^{-2}$$

$$\rho \frac{d c_v \theta}{dt} \approx \rho_0 c_v$$

$$\frac{Q}{\rho \frac{d c_v \theta}{dt}} \approx \left(\nu / c_v\right) \cdot V / L \Delta\theta.$$

For a typical gas, $\nu / c_v \approxeq 10^{-8}$, os the viscous dissipation rate can be neglected except for very large values of $V/L\Delta\theta$. The heating due to compression can be rewritten considering the continuity equation 3.1, replacing the density with the temperature, and considering that for a perfect gas $p = (c_p - c_v)\rho\theta$:

$$-p\nabla \cdot u = \alpha p \frac{d\theta}{dt} = (c_p - c_v)\rho \frac{d\theta}{dt}.$$

With these assumption, the energy equation becomes

$$\frac{d\theta}{dt} = k\nabla^2\theta$$

where $\kappa = k/\rho_0 c_p$ is the thermal diffusivity. The temperature can be decomposed into three different contribution:

$$\theta = \theta_0 + \tilde{\theta}\left(x_3\right) + \theta'\left(\mathbf{x}, t\right) \tag{3.5}$$

where

θ_0	reference temperature
$\tilde{\theta} = Gx_3$	background linear gradient
θ'	perturbation

We can substituting the temperature with this definition, and taking the linear variation inside the pressure gradient term; therefore the momentum equation becomes:

$$\frac{D\mathbf{u}}{Dt} = -\nabla\tilde{p} + \nu\nabla^2\mathbf{u} + \alpha G x_3 \mathbf{g} + \alpha\theta'\mathbf{g}$$

where the hydrostatic pressure $\tilde{p}$ is defined as

$$\tilde{p} = \frac{p}{\rho_0} + g x_3 + \frac{1}{2}\alpha g x_3$$

while the energy equation

$$\frac{D\theta'}{Dt} + u_3 G = \kappa\nabla^2\theta'$$

We can now introduce the Brunt - Väisälä frequency for the mean gradient:

$$\mathcal{N}^2 = -\frac{g}{\rho}\frac{\partial\rho}{\partial x_3} = \alpha g \frac{d\tilde{\theta}}{dx_3} = \alpha g G. \tag{3.6}$$

The final dimensional system is:

$$\begin{cases} \nabla \cdot \mathbf{u} = 0 & (3.7) \\ \dfrac{D\mathbf{u}}{Dt} = -\nabla\tilde{p} + \nu\nabla^2\mathbf{u} + \dfrac{\mathcal{N}^2}{G}\theta' & (3.8) \\ \dfrac{D\theta'}{Dt} = \kappa\nabla^2\theta' - G u_3 & (3.9) \end{cases}$$

For the adimensionalization, we can consider the following dimensionless variable:

$\hat{u} = u/U_{\mathrm{ref}}$	velocity
$\hat{x_i} = x_i/L_{\mathrm{ref}}$	lenght
$\hat{\theta} = \theta'/L_{\mathrm{ref}}G$	temperature
$\hat{t} = t \cdot L_{\mathrm{ref}}/U_{\mathrm{ref}}$	time

The dimensionless system is (we drop the hat for convenience):

$$\begin{cases} \nabla \cdot \mathbf{u} = 0 & (3.10) \\ \dfrac{D\mathbf{u}}{Dt} = -\nabla \tilde{p} + \dfrac{1}{\mathrm{Re}}\nabla^2 \mathbf{u} + \dfrac{1}{\mathrm{Fr}^2}\theta' & (3.11) \\ \dfrac{D\theta'}{Dt} = \dfrac{1}{\mathrm{RePr}}\nabla^2 \theta' - u_3 & (3.12) \end{cases}$$

where we have introduced the dimensionless parameter:

- Reynolds number Re= $\frac{U_{\mathrm{ref}}L_{\mathrm{ref}}}{\nu}$
- Froude number Fr= $\frac{U_{\mathrm{ref}}}{L_{\mathrm{ref}}\mathcal{N}}$
- Prandtl number Pr= $\frac{\kappa}{\nu}$

It is interesting to observe how the energy equation becomes formally equal to the passive scalar advection/diffusion transport shown in the previous chapter. The real difference in the Boussinesq equation is the presence of the buoyancy term as external force inside the momentum equation, and the temperature θ can be interpreted as an active scalar.

3.2 Brunt-Väisälä frequency and Froude number

We want now to understand the physical meaning of the Brunt-Väisälä frequency and the Froude number.

The Brunt-Väisälä, introduced in the previous section, is defined, in terms of density, as

$$\mathcal{N} = \sqrt{-\frac{g}{\rho_0}\frac{d\rho}{dx_3}} \tag{3.13}$$

where x_3 represent the direction on which the buoyancy force acts – so the vertical direction. The Brunt-Väisälä is a real positive number if the density decreases upward and an imaginary otherwise. For a basic stability study, we can consider the effect of a little (positive or negative) vertical displacement h of a fluid particle in a stationary flow, where the density varies only in the vertical direction. As a consequence, the fluid particle has a density related to its initial position $\rho_1 = \rho(x_3)$, and it is moved to an altitude where the density is $\rho_2 = \rho(x_3 + h)$.

It is intuitive to deduce the effects of stratification on that fluid particle. For instance, we consider an upward shift. If the density decrease upward, the fluid particle will be heavier respect to the surrounding environment (i.e. $\rho_1 > \rho_2$). The buoyancy forces push the particle downwards, through its original position. When this altitude is reached, there are no more forces, but the particle as still a downwards velocity, so the displacement becomes negative: a buoyancy force reappears, this time pushing the particle upward. The result is an harmonic motion around the original position. Instead, considering an increase of density upwards, after the first displacement the particle is pushed away respect to its stable position.

To formalize these consideration, we can consider that, in absence of motion, the momentum equation 3.8 can be simplified to an hydrostatic relation:

$$\frac{\partial p}{\partial z} = -\rho g$$

and the Lagrangian equation for the displaced fluid particle becomes

$$\frac{dw}{dt} = \frac{d^2 h}{dt^2} = \frac{q}{\rho_0}(\rho_2 - \rho_1)$$

where w is the velocity of the fluid particle. As the displacement is small, the density can varies linearly in the vertical direction, and so we can finally obtain the equation for the particle motion

$$\frac{d^2 h}{dt^2} + \mathcal{N}^2 h$$

The solution of these equation depends on the sign of $\mathcal{N}^2$. In particular we can have:

- A statistically stable fluid, $N^2 > 0$: the density decrease and the temperature increase with the altitude. The solution of the fluid particle motion is given by $h(t) = a \cdot \cos(\mathcal{N}t) + b \cdot \sin(\mathcal{N}t)$: a fluid particle oscillates around its equilibrium position if it is vertically displaced, with a frequency equal to $\mathcal{N}$.

- A statistically unstable fluid, $N^2 < 0$, the density increase and the temperature decrease with the altitude. The solution of the fluid particle motion is given by $h(t) \approxeq a \cdot \exp^{i\mathcal{N}t}$: a fluid particle moves away indefinitely from its initial position as soon as any perturbation deviate from it, with a growth factor of $i\mathcal{N}$.

In the complete system equations, the Froude number correlates the importance of the buoyancy terms with the kinetic forces. In particular, we consider the square Froude number which appears in the dimensionless momentum equation:

$$\mathrm{Fr}^2 = \frac{U}{L\mathcal{N}}.$$

The buoyancy forces becomes more and more important as $|\mathrm{Fr}^2| \to 0$. The importance of the buoyancy term depends on the temperature/density gradient (high values implies high $\mathcal{N}$), but also in case of low kinetic energy respect to the system dimension (low values of the ratio U/L).

Summing up, the more the Froude number tends to zero, the more the stratification effects take importance: in particular, we can distinguish the following case:

- $|\mathrm{Fr}^2| \gg 1$ non stratified flow: buoyancy forces are negligible respect to the other terms, and temperature behaves as a passive scalar, without feedback on the velocity field

- $Fr = O(1)$, stable stratified flow: buoyancy forces acts stabilizing the motion, suppressing the velocity fluctuations which tend to move the fluid particles from their equilibrium positions.

- $Fr = O(1)$, unstable stratified flow: buoyancy forces acts enhancing the velocity fluctuations which tend to move the fluid particles from their equilibrium positions.

- $Fr \to 0_{\pm}$, purely stratified flow: the kinematic forces are negligible respect to the buoyancy force, which drive the motion.

3.3 The stratified shearless mixing

Similarly to what done in the previous chapter, we consider the interface between two HIT (Homogeneous Isotropic Turbulence) in a $6\ m \times 6\ m \times 12\ m$ parallelepipedic domain, with different levels of kinetic energy and passive scalar. We choose that kind of domain in order to simulate the lowest part of the inertial range and the dissipative one, as shown in figure 3.2 in comparison

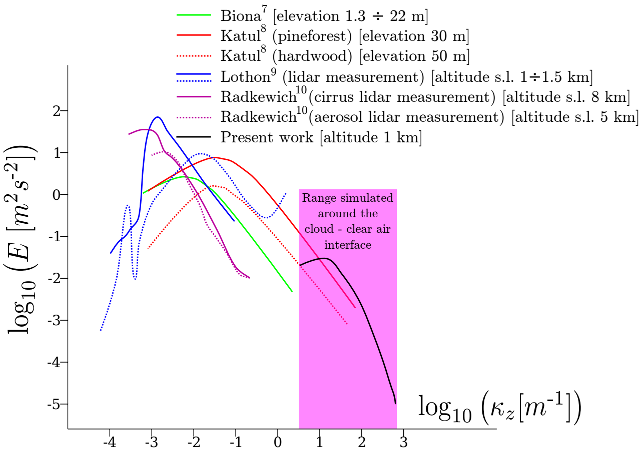

Figure 3.2. Kinetic energy spectra. Contextualization of present study (black spectra, small inertial and dissipative range) respect to spectra from in-situ atmospheric measurements Biona *et al.* (2001); Katul *et al.* (1998); Lothon *et al.* (2009); Radkevich *et al.* (2008) (colored spectra, energy injection and low wave-number inertial scales).

with in situ measurement of the atmospheric energy spectra. As shown in figure 3.3, the two HIT regions, which compose the system, interact through a mixing layer, whose initial thickness has been set of the same order of the integral scale of the turbulence background ℓ, here assumed equal to $3 \cdot 10^{-2}$ m.

The kinetic energy of the two isotropic regions (external from the mixing) have a different kinetic energy. The lower and more energetic region (that is the reference region) has a kinetic energy equal to $E_1 = 0.06\ m^2/s^2$; the root mean square of the velocity in this region is $u_{rms} = 0.2 m/s$ with an initial Taylor microscale Reynolds number number equal to $Re_lambda \approx 250$ (λ is the Taylor scale). The kinetic energy ratio between the two region is equal to 6.7. This energy ratio is comparable to the ones measured in warm clouds (see, e.g., Malinowski *et al.* (2013)) and, furthermore, it allows us to compare our results (shown in previous chapter and (Tordella & Iovieno, 2011)) and with experiments on shearless mixing (see Veeravalli & Warhaft (1989); Jayesh & Warhaft (1994)) in absence of any stratification.

As previously shown, buoyancy is taken into account through a local perturbation θ' in the profile of temperature distribution θ inside the troposphere. The Prandtl number considered is Pr$= 0.74$ (standard atmosphere, altitude of 1000 m s.l.). The initial conditions for the temperature perturbation is described in figure 3.3 and in table 3.1. The ratio between inertial and buoyancy forces is expressed by the Froude number Fr, which with these quantities can be written as

$$Fr = \frac{u_{rms}}{\ell \mathcal{N}} \qquad \mathcal{N} = \sqrt{\alpha \theta_0 \frac{\mathrm{d}\theta}{\mathrm{d}x_3}} \tag{3.14}$$

In order to characterize each simulation we consider the initial square of the Froude number Fr^2 based on the maximum gradient within the initial interface. For stable cases, the initial Fr^2 ranges from 1038.5 (negligible stratification) to 0.4 (strong stable stratification). For unstable cases (where the initial temperature perturbation gradient is negative) we consider two cases with Fr^2=-20.8 (mild unstable stratification) and -4.2 (strong unstable stratification). It is important to observe that the physical value of the Froude number changes as the system evolves: the turbulence naturally decays in time, and the temperature gradient tends to decrease as the mixing interface thickens. The first effect is dominant, as so Fr magnitude decrease in time, as shown in figure 3.4.

The water vapor is consider to be a passive scalar, neglecting effects related to condensation/evaporation, inertial particle motion, and dropplet formation – so the maximum concentration of the water vapour is much lower respect to its saturation point. We take into account it through its concentration χ, which is equal to 1 (maximum concentration) in the lower region, and to 0 in the upper region (no vapour present). Water vapour transport is modeled using an advective/diffusive equation, with a Schmidt number Sc=0.61 (standard atmosphere, altitude of 1000 m s.l.).

$\nabla_z T_{ic}$ $[Km^{-1}]$	ΔT $[K]$	$\mathcal{N}_{ic}$ $[s^{-1}]$	Fr	Fr^2	Re_b
$1.3\cdot10^{-2}$	$4.0\cdot10^{-3}$	$2.13\cdot10^{-2}$	45.57	1038.5	0.7
$2.0\cdot10^{-1}$	$6.0\cdot10^{-2}$	$5.24\cdot10^{-2}$	8.32	69.2	10.9
$6.7\cdot10^{-1}$	$2.0\cdot10^{-1}$	$1.50\cdot10^{-1}$	4.56	20.8	36.3
3.3	1.0	$3.35\cdot10^{-1}$	2.04	4.2	181.7
$3.3\cdot10^{1}$	$1.0\cdot10^{1}$	1.06	0.64	0.4	1817.2
$-6.7\cdot10^{-1}$	$-2.0\cdot10^{-1}$	/	/	-20.8	-36.3
-3.3	-1.0	/	/	-4.2	-181.7

Table 3.1. Initial stratification level parameters. $\mathcal{N}_{ci} = \sqrt{\alpha g \frac{\partial \theta}{\partial x_3}}$ is the characteristic Brunt-Väisälä frequency of initial condition. The Froude number Fr= $\frac{u'_{rms}}{\mathcal{N}_{ic}\ell}$ and the Reynolds Buoyancy number $\mathrm{Re}_b = \frac{\varepsilon \mathcal{N}^2}{\nu}$ give a measure of the order of magnitude of the buoyancy forces compared with the inertial terms (ε is the initial energy dissipation rate, ν the kinematic viscosity).

The motion is driven by the continuity 3.7, momentum 3.8 and energy balance equations 3.9 within the Boussinesq approximation, which holds for

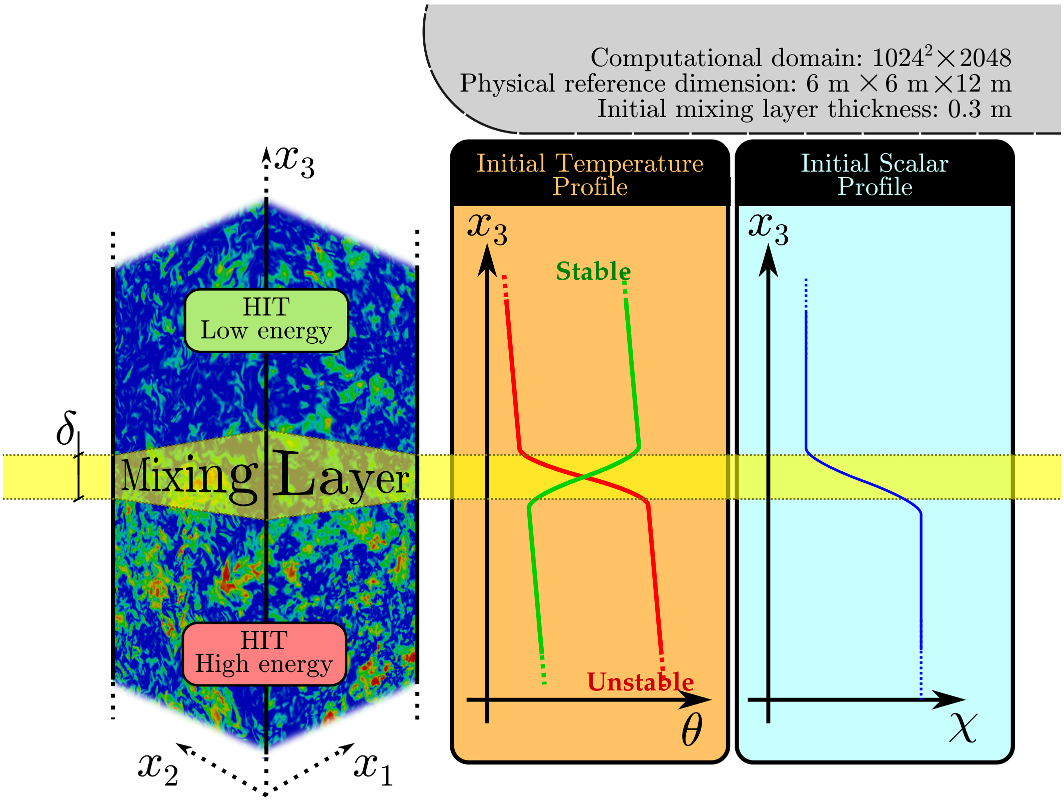

Figure 3.3. Scheme of the initial conditions. E_1 is the mean initial turbulent kinetic energy of the below the mixing (high energy region), E_2 of the above the mixing (low energy region). For the top cloud mixing here presented we consider $E_1/E_2 = 6.7$. The stratification is represented, inside the mixing, as a local temperature perturbation respect to the neutral profile; the perturbation can be both stable or unstable. The passive scalar is initially present only in the high energy region.

small temperature variations Drazin & Reid (1981)

$$\begin{aligned} \boldsymbol{\nabla} \cdot \boldsymbol{u}' &= 0 && (3.15a)\\ \frac{\partial \boldsymbol{u}'}{\partial t} + (\boldsymbol{u}' \cdot \boldsymbol{\nabla})\, \boldsymbol{u}' &= -\boldsymbol{\nabla}\frac{\tilde{p}}{\rho} + \nu \nabla^2 \boldsymbol{u}' + \alpha \boldsymbol{g} \theta' && (3.15b)\\ \frac{\partial \theta'}{\partial t} + \boldsymbol{u}' \cdot \boldsymbol{\nabla} \theta' + u_3 G &= \kappa \nabla^2 \theta' && (3.15c)\\ \frac{\partial \chi}{\partial t} + \boldsymbol{u}' \cdot \boldsymbol{\nabla} \chi &= d_\chi \nabla^2 \chi, && (3.15d) \end{aligned}$$

where, according to the definition in section 3.1, $\theta = \theta_0 + \tilde{\theta}(x_3) + \theta'(\boldsymbol{x}, t)$ is the temperature, composed by the reference constant temperature θ_0, the static component $\tilde{\theta}(x_3) = Gx_3$, and the fluctuation $\theta'(\boldsymbol{x}, t)$; $\tilde{p} = p + \alpha g x_3 \left(\theta_0 + Gx_3/2\right)$ is the total hydrodynamic pressure(p is the fluid-dynamic pressure, α the thermal expansion coefficient, g the gravity acceleration); u' is the velocity fluctuation; and χ is the vapor concentration of the air - water vapor mixture. The constant κ and d_χ are respectively the thermal and water vapor diffusivity.

Similarly to the shearless mixing presented in chapter 2, the initial conditions for the velocity field are obtained by a linear matching of two different HIT fields u_1 and u_2, that are randomly generated, respecting physical conditions imposing spectra, solenoidality, integral scale and mean kinetic energy), see Tordella & Iovieno (2006). The initial energy profile along direction x_3 is obtained coupling the fields u_1 and u_2 by using equation (3.16a). For what concenrns the scalars, the initial condition (constant along direction x_1 and x_2) is given by equations 3.16b for temperature and 3.16c for water vapor concentration, in analogy with previous work (see Tordella *et al.* (2008); Iovieno *et al.* (2014)). The equation for the initial conditions are:

$$\begin{aligned} \boldsymbol{u'}(\boldsymbol{x}, t=0) &= \boldsymbol{u_1}(\boldsymbol{x}) p_1(x_3) - \boldsymbol{u_2}(\boldsymbol{x})(1 - p_1(x_3)) && (3.16a)\\ \theta(\boldsymbol{x}, t=0) &= \Delta\theta p_2(x_3) && (3.16b)\\ \chi(\boldsymbol{x}, t=0) &= p_1(x_3), && (3.16c) \end{aligned}$$

where u_1 and u_2 are the two external HIT, $\Delta\theta$ is the initial temperature step, and the weight functions $p_1(x_3)$ and $p_2(x_3)$ are defined as:

$$\begin{aligned} p_1(x) &= \frac{1}{2}\left[1 + \tanh\left(a\frac{x_3}{L_3}\right) + \tanh\left(a\frac{x_3 - L3/2}{L_3}\right) + \tanh\left(a\frac{x_3 - L_3}{L_3}\right)\right] && (3.17a)\\ p_2(x) &= \frac{x_3}{L_3} - \frac{1}{2}\left[1 + \tanh\left(a\frac{x_3 - L_3/2}{L_3}\right)\right]. && (3.17b) \end{aligned}$$

The simulations were performed using our home produced computational code that implements a pseudo-spectral Fourier-Galerkin spatial discretization and an explicit low storage fourth order Runge-Kutta time integration scheme. Evaluation of non-linear (advective) terms is performed through the 3/2 de-aliased method Iovieno *et al.* (2001). The grid has $N \times N \times N_3$ points, with $N = 2^{10}$ and $N_3 = 2N$), for a total of 2^31 grid-points. Such grid allows to capture all the turbulent scales from the greatest (integral scale ℓ) to the smaller (Kolmogorov scale η). In order to make the simulations feasible (breaking down limitations due to computation time and memory required), the computational code uses a stencil parallelization to split the computational grid among an huge amount of processors (according to the distributed memory paradigm), and communication are performed through the MPI libraries.

The simulation were performed at the TGCC Curie supercomputer within the PRACE project n° RA07732011 for a total of 3 million cpu-hours.

3.4 Results

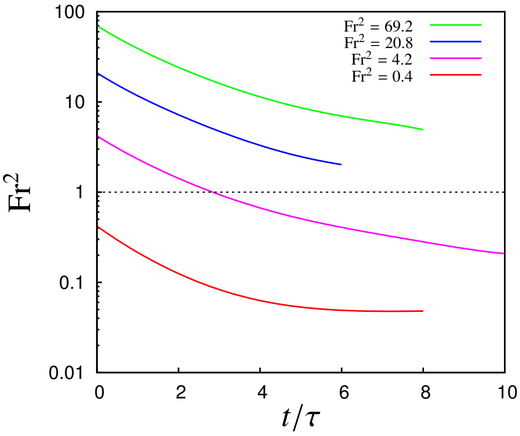

Figure 3.4. Time evolution of the instantaneous Froude number $\mathrm{Fr}^2(t)$ for the stably stratified simulations (the evolution for unstable cases is very closed to this, except for the sign). The horizontal dotted line, Fr^2=1, indicates when the buoyancy forces becomes of the same order of the kinematic forces. Relevant effect have been founded when $\mathrm{Fr}^2(t) \approx 2 \div 3$. [External MEDIA: file **2DVideo_stratificatoFr4.mp4** shows the btime evolution of scalar, vertical velocity, and dissipationin a slice of the domain for the case Fr^2=4.2.]

In this section we focus on the analysis of the simulated fields, comparing the results in different case of both stable and unstable stratification: first (...) we analyze the statistical behavior of velocity and scalar fields. The formation of kinetic energy sublayers inside the mixing region is discussed (...), as well as its effects on the transport/entrainment process (...). We finally analyze flow structure, anisotropy and small-scale dynamics (...).

A qualitative representation of the fields are reported in figure 3.5, which shows 3-dimensional visualization snapshots after 2, 4, and 6 initial eddies turnover time for three different cases – neutral stratification (Fr^2=69.2), stable stratification (Fr^2=4.2) and unstable stratification (Fr^2=-4.2). In the figure, the color is related to the passive scalar concentration, white where it is maximum ($\chi = 1$) and blue where it is absent ($\chi = 0$). The isosurfaces represent the vortices inside th flow, which are identified using the Q-criterion: it consider the local balance between shear strain rate and vorticity magnitude, defining vortices as areas where the vorticity magnitude is greater than the

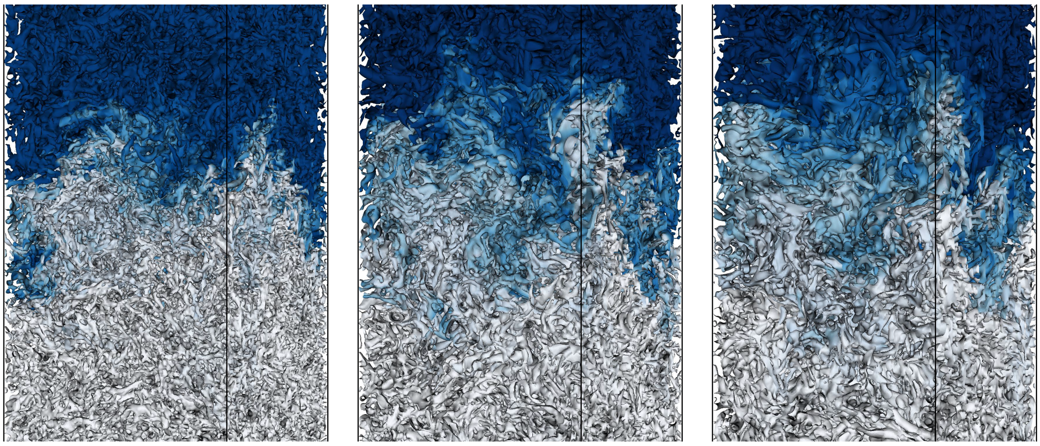

(a) Fr^2=4.2, $t/\tau = 2$ (b) Fr^2=4.2, $t/\tau = 4$ (c) Fr^2=4.2, $t/\tau = 6$

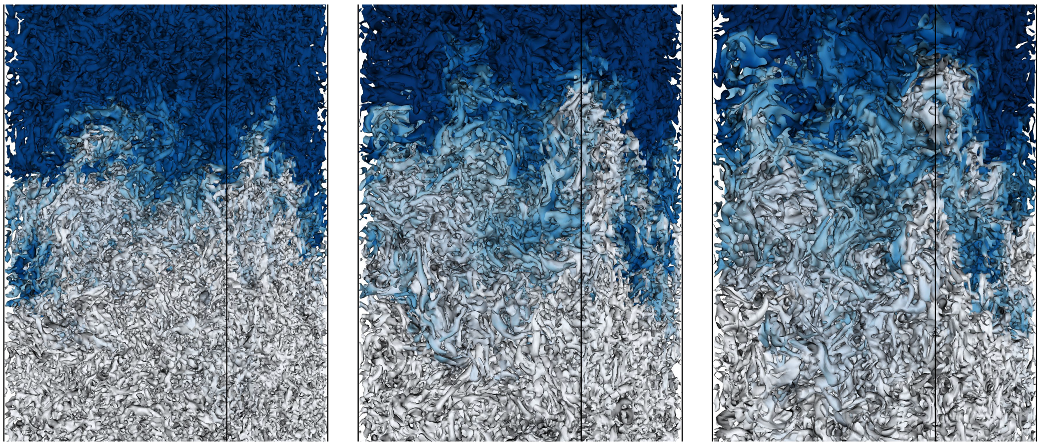

(d) Fr^2=69.2, $t/\tau = 2$ (e) Fr^2=69.2, $t/\tau = 4$ (f) Fr^2=69.2, $t/\tau = 6$

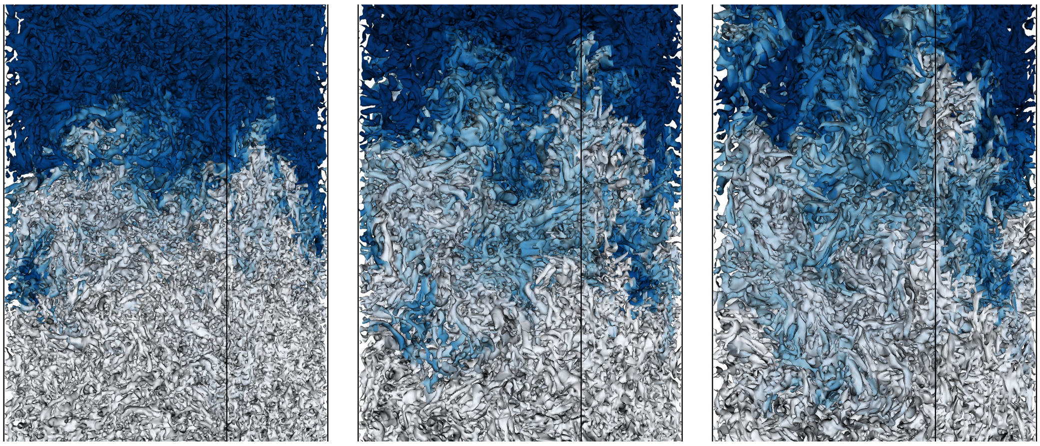

(g) Fr^2=-4.2, $t/\tau = 2$ (h) Fr^2=-4.2, $t/\tau = 4$ (i) Fr^2=-4.2, $t/\tau = 6$

Figure 3.5. Isosurfaces of the vortices edges computed using the Q-criterion (see equation 3.18)for different stratification levels after 2, 4, and 6 time-scales. Strong stable on top panels(Fr^2=4.2, panels a–c), mild stable in center panels (Fr^2=69.2, panels d–f), and strong unstable on bottom panels(Fr^2=-4.2, panels g–i). Isosurfaces are colored using the passive scalar concentration, ranging from white (maximum scalar concentration) to blue (no scalar).

magnitude of rate-of-strain. [S. Kida, H. Miura, 1998 Identification and Analysis of Vortical Structures Eur. J. Mech. B/Fluids, 471-488]. Such condition is achieved where $Q \geq 0$, with Q defined as

$$Q = \left(\|\overline{\mathbf{\Omega}}\|^2 - \|\overline{\mathbf{S}}\|^2 \right) / \left(\|\overline{\mathbf{\Omega}}\|^2 + \|\overline{\mathbf{S}}\|^2 \right) \tag{3.18}$$

where, $\overline{\mathbf{\Omega}} = 0.5 \left(\partial u_i / \partial x_j - \partial u_j / \partial x_i \right)$ and $\overline{\mathbf{S}} = 0.5 \left(\partial u_i / \partial x_j + \partial u_j / \partial x_i \right)$ are the vorticity and strain tensors respectively.

3.4.1 Spatial statistical properties

The statistics are computed by averaging the variables in the planes (x_1, x_2) normal to the mixing direction (with a sample of $2^{10} \times 2^{10}$ data-points), focusing on the variation along the vertical (non-homogeneous) direction x_3: for that reason, we define the avarage operator $\langle \bullet \rangle (x_3)$ as the mean inside a plane (x_1, x_2) at a certain value of x_3:

$$\langle \bullet \rangle (x_3) = \frac{1}{2^{20}} \sum_{i=1}^{2^{10}} \sum_{j=1}^{2^{10}} \bullet (x_{1,i}, x_{2,i}, x_3).$$

In particular, the second order moment is represented by the variance for the scalar fields θ and χ, and by the turbulent kinetic energy for the velocity field, defined as $E = \frac{1}{2} \left(\langle u_1^2 \rangle + \langle u_2^2 \rangle + \langle u_3^2 \rangle \right)$ and the high-order moments are represented by skewness and kurtosis (respectively third and fourth order moments normalized with the variance), defined as $S(\bullet) = \langle \bullet^3 \rangle / \langle \bullet^2 \rangle^{1.5}$ and $K(\bullet) = \langle \bullet^4 \rangle / \langle \bullet^2 \rangle^2$. Note that the definition of skewness and kurtosis for the passive scalar field χ sligthly differs from the one of previous equation, due to the proximity of the external regions where the variance $\langle \chi^2 \rangle$ vanishes: to prevent numerical problems, the actual definition of skewness and kurtosis are: $S(\chi) = \langle \chi^3 \rangle / \left(\langle \chi^2 \rangle + 0.005 \langle \chi^2 \rangle_{\max} \right)^{1.5}$ and $K(\chi) = \langle \chi^4 \rangle / \left(\langle \chi^2 \rangle + 0.01 \langle \chi^2 \rangle_{\max} \right)^2$, where $\langle \chi^2 \rangle_{\max}$ indicates the maximum of the variance along the direction x_3.

Looking at the statistical behavior of the turbulent kinetic energy in figure 3.6, the evolution of the system can be split in two main stages, according to the evolution of the ratio between buoyancy force and kinematic forces (which are advection and diffusion). As long as the ratio remains small, there are no significant differences with respect to a non-stratified case. On the contrary, as the stratification perturbation level become higher, buoyancy effects are no more negligible: differences are present from both a quantitative and qualitative point of view. The effects of different stratification levels are clearly visible on the turbulent kinetic energy shown in figure 3.6 for two different instants, in particular $t/\tau = 4$ in 3.6(a) and $t/\tau = 7$ in 3.6(b), where τ is the initial eddy turnover time. The time required to have the buoyancy terms comparable with other forces depends directly on the stratification intensity. When this condition is reached, initially there is a slight downward displacement of the energy gradient location, as can be observed for Fr^2=4.2 at $t/\tau = 4$ and for Fr^2=20.8 at $t/\tau = 7$. Subsequently, it can be observed the formation, in correspondence of the local temperature perturbation, of a layer with a pit of kinetic energy that grows in time (see also section 3.4.2). The presence of such sublayer deeply changes the physics of the system, because in this situation two interfaces are produced. The first interface, (which is present also in the absence of stratification), now separates the high turbulent energy region from the pit, while the second one (not present without stratification) separates the low turbulent energy region from the center of the mixing layer. Therefore, a strong stable stratification induces a physical separation between the two external regions, greatly decreasing the interaction between them. On contrary, in unstable case it can be observed an increment of the kinetic energy inside the mixing region (peak sublayer). Also in this case we can observed the formation of a secondary gradient of energy, but the position are reversed respect to the stable cases, and the secondary gradient separates the peak from the high energy region. In fact, in these cases the peak tends to be shifted toward the high energy region (while the pit was near the low energy one), and the primary gradient this time is pushed upwards (positive x_3), separating the peak from the low energy region.

Both the primary interface and (when present) the secondary one presents an intermittent behavior: figure 3.7 shows a comparison of the distribution of skewness and kurtosis after 6 time scales (respectively panels *a* and *c*), and the time evolution of the maximum and minimum values (panels *b* and *d*). In the stably stratified cases it can be observed an initial reduction of maximum values, which decay much faster respect to a non stratified case. As consequence, such fast decay leads to have low intermittency during the pit formation, with values as low as the one observed outside the mixing region (the "normal" range is represented by a gray band in panels *b* and *d* in figure 3.7). Afterwards the pit onset, each one of the two gradient of energy characterized by intermittency, and S and K quickly grow in time reaching higher values respect to the unstratified case. On contrary, in case of unstable stratification the decay of intermittency is immediately damped, and for case Fr^2=-4.2 a growth of S and K is observed after only 3 time scales. In both stable and unstable cases, the final configuration seems to be more intermittent, with values that can become even 100% greater respect to the ones in unstratified case.

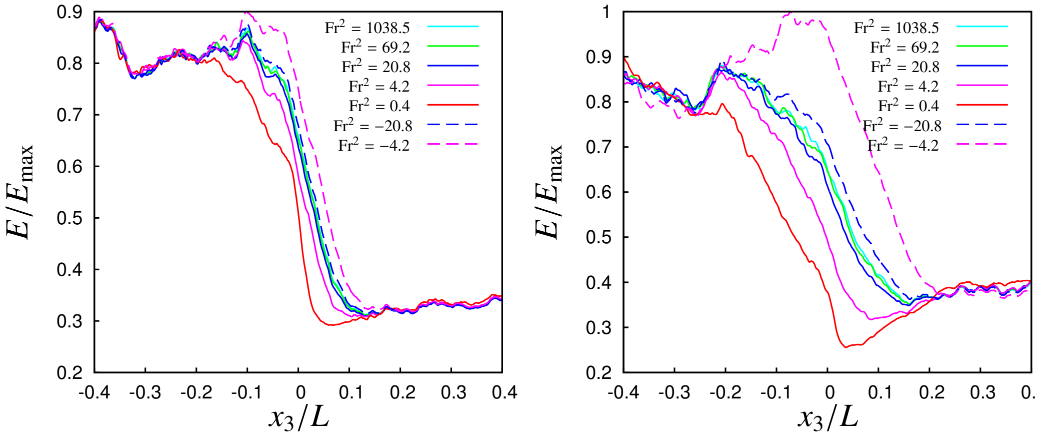

(a) Kinetic energy, $t/\tau = 3$ (b) Kinetic energy, $t/\tau = 6$

Figure 3.6. Turbulent kinetic energy along the vertical direction x_3, computed through the velocity variance in the horizontal planes $x_1 - x_2$. In the panel (a) data are taken after 4 initial eddies turnover time τ, in the panel b after 7 τ. Data are taken from simulations with different level of stable stratification represented by the reference square Froude number Fr^2. [External MEDIA: file **isosurfaceVertVel_stratifFr4.mp4** shows the behavior of vertical velocity isosurfaces for the case Fr^2=4.2 after 6 time scales.]

The statistical properties of the temperature θ and the passive scalar concentration χ, in are analogous: in fact the energy equation 3.15c that governs the transport of temperature is comparable with the advective-diffusive equation 3.15d of the passive scalar (with the Schmidt number instead of the Prandtl number). Effects on scalar fields are lower respect on the one observed in the velocity, and great variations can be observed only for very strong stratification, with Fr^2=0.4.In particular, the scalars fluctuations are damped in stable cases, and slightly enhanced in presence of unstable stratification, as can be observed in figures 3.8(a). Also The region with non-zero variance depends on the stratification level, and becomes thiner for stable cases - which indicates a smaller mixing region. It can be also observed that the shape of the mean variance along x_3 is clearly non-symmetrical respect to the center of the mixing region. These reduction become relevant after the onset of the pit of energy and are linked with the reduction of entrainment, see figure 3.8(b) for the evolution of scalar variance peak value.

For the high-order moments, scalars fields initially follow the velocity behavior, with a reduction of S and K when the stratification is stable, and a growth in unstable cases, see figures 3.8(c-e). A big difference can be observed after few time scales for stable stratification: the pit onset blocks the mixing, and the values of the high-order statistics tents to remain constant, as shown

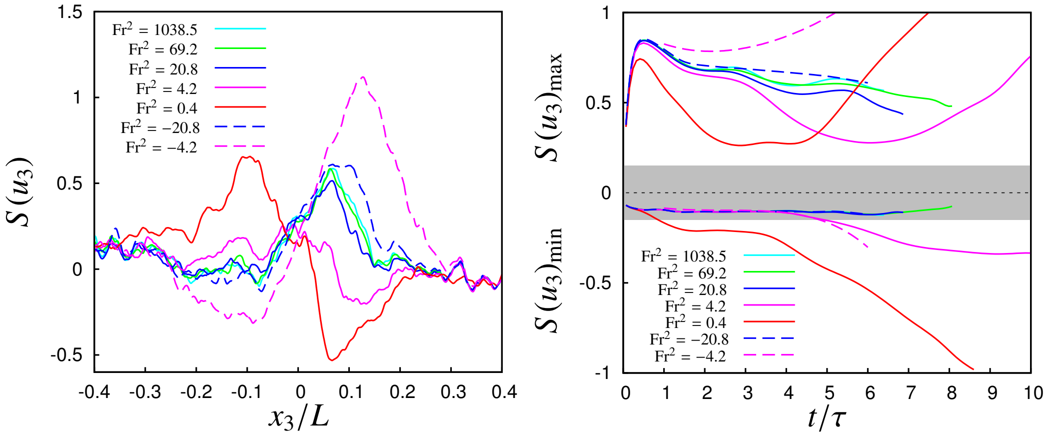

(a) Vertical velocity skewness, $t/\tau = 6$

(b) Peaks values of vertical velocity skewness over time

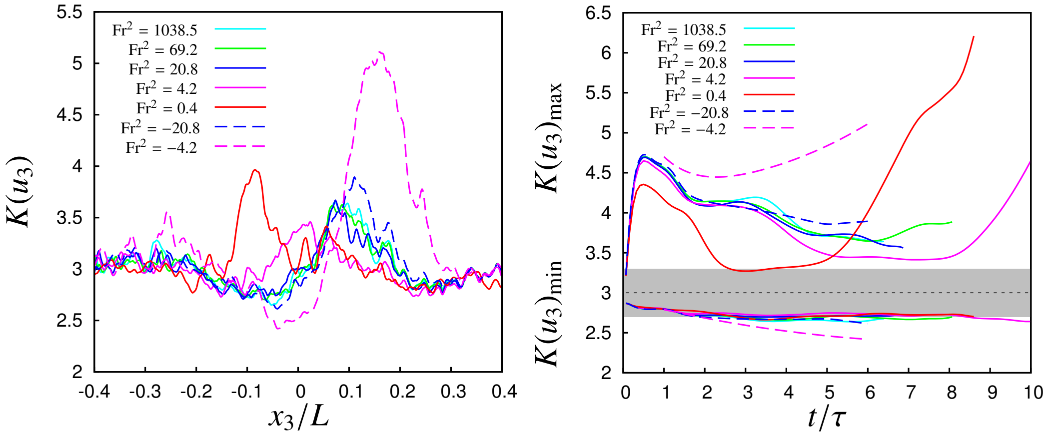

(c) Vertical velocity kurtosis , $t/\tau = 6$

(d) Peaks values of vertical velocity kurtosis over time

Figure 3.7. Vertical velocity skewness (panels a-b) and kurtosis (panels c-d) along the vertical direction x_3, computed through vertical velocity central moments in the horizontal planes $(x_1 - x_2)$ at two different instant. Data are taken after 3 initial eddies turnover time τ (panels a-c) and after 6 τ (panels b-d). The various lines come from simulations with different level of stable stratification represented by the reference square Froude number Fr^2.

in figures 3.8(d-f). As for the scalar variance, also for S and K big differences are visible only for Fr^2=0.4, while other cases shows only minor changes in the behavior.

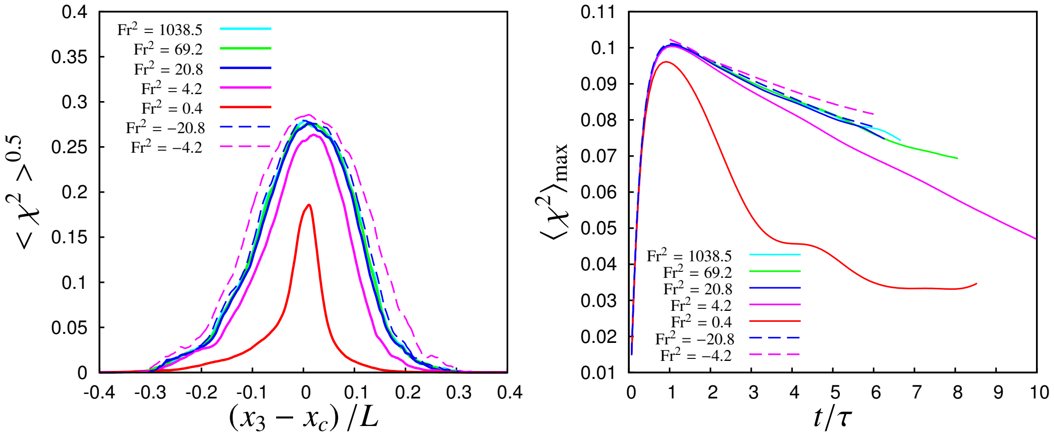

(b) $t/\tau = 6$, vapour variance (b) $t/\tau = 6$, vapour variance

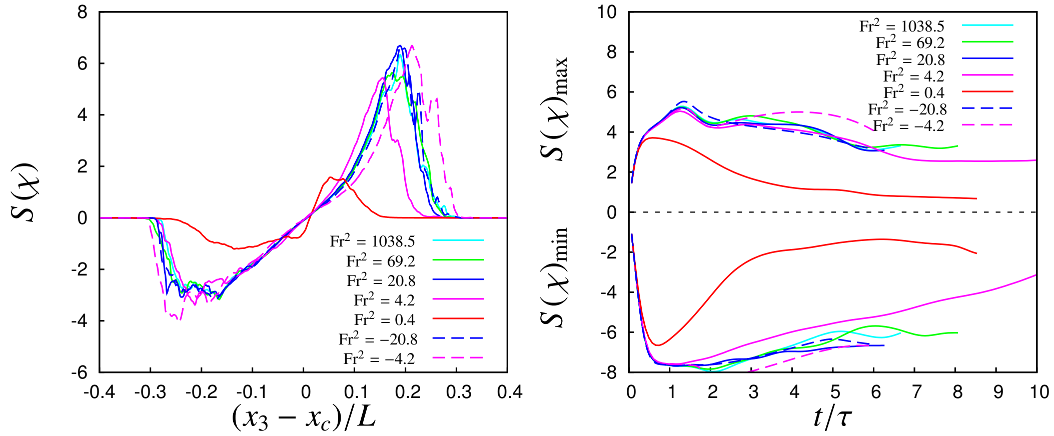

(d) $t/\tau = 6$, vapour skewness (d) $t/\tau = 6$, vapour skewness

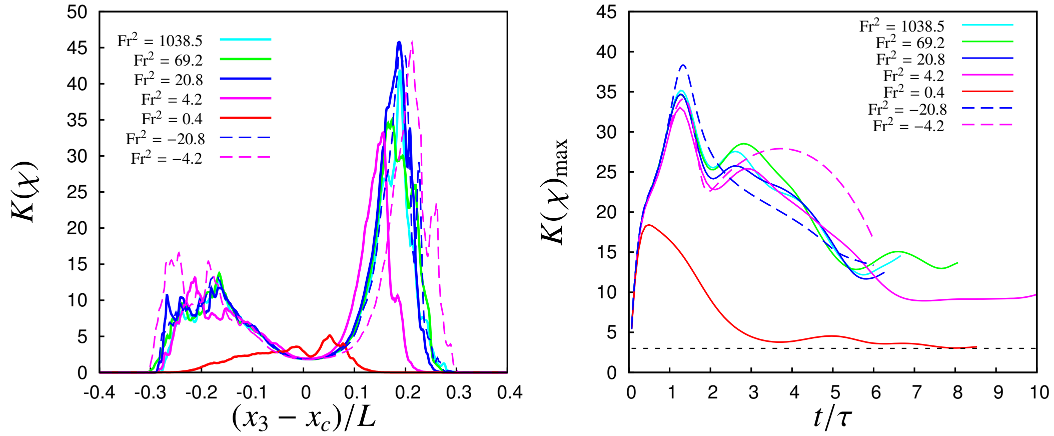

(f) $t/\tau = 6$, vapour kurtosis (f) $t/\tau = 6$, vapour kurtosis

Figure 3.8. Vapour statistics along the vertical direction x_3, computed through the central moments in the horizontal planes $x_1 - x_2$. Left panels refer to data taken after 3 initial eddies turnover time τ, while the right ones after 6 τ. Data are taken from different simulation represented by the initial square Froude number Fr^2. Panels a and b shown the vapour variance normalized with the initial vapour step, panels c and d the vapour skewness and panels e and f the kurtosis.

3.4.2 Mixing layer and energy pit/peak sublayer

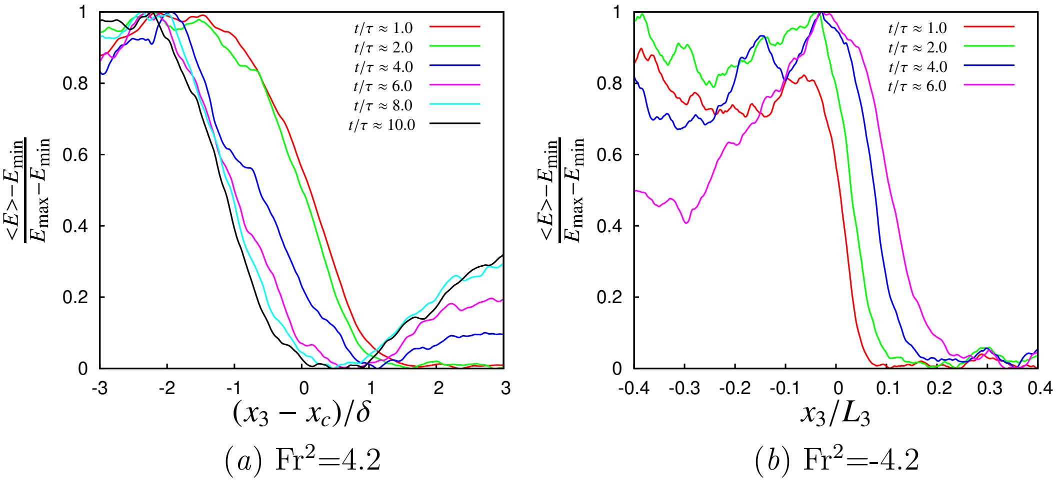

(a) Fr^2=4.2 (b) Fr^2=-4.2

Figure 3.9. Normalized kinetic energy distribution at different time instants in the case Fr^2=4.2 (panel a) and Fr^2=-4.2 (panel b). (a) – Initially all the top region (rigth part of the plot) has a value around 0, which means that there isn't a region with lower energy levels. The pit onset starts around $t/tau = 2$, and it is clearly visible at $t/\tau = 4$, when the region with values next to 0 are only in the center of the mixing layer. (b) – In this case the low energy region has always a value around 0, so there is not a region with lower energy levels. On contrary, a reduction in the high energy region is observed, which means that tially all the top region (rigth part of the plot) has a value around next to 0, which means that there isn't a region with lower energy levels. The pit onset starts around $t/\tau = 2$, and it is clearly visible at $t/\tau = 4$, when the region with values next to 0 are only in the center of the mixing layer.

As seen in section 3.4.1, when the buoyancy term becomes not negligible, it can be observe the onset of a sublayer in the center of the domain – where the initial temperature gradient is placed. In such sublayer the kinetic energy decrease faster in stable cases, and slower in the unstable ones. The formation and time evolution of such sublayers are shown in figure 3.9, where the kinetic energy is represented in the form $E_{\text{norm}} = (\langle E\rangle - E_{\min}) / (E_{\max} - E_{\min})$ where $E_{\max}$ $E_{\min}$ are respectively the maximum and the minimum of the mean kinetic energy. In unstratified condition, the normalized energy is near 0 in the low energy region, and near 1 in the high energy region.

In stable cases, the presence of the pit of energy changes the location of $E_{\min}$, which now is placed inside the pit, while $E_{\max}$ is always represented by the high energy region. As a consequence, after the pit onset, E_{norm} is approximately equal to 1 in high-energy region, 0 inside the pit and > 0 in

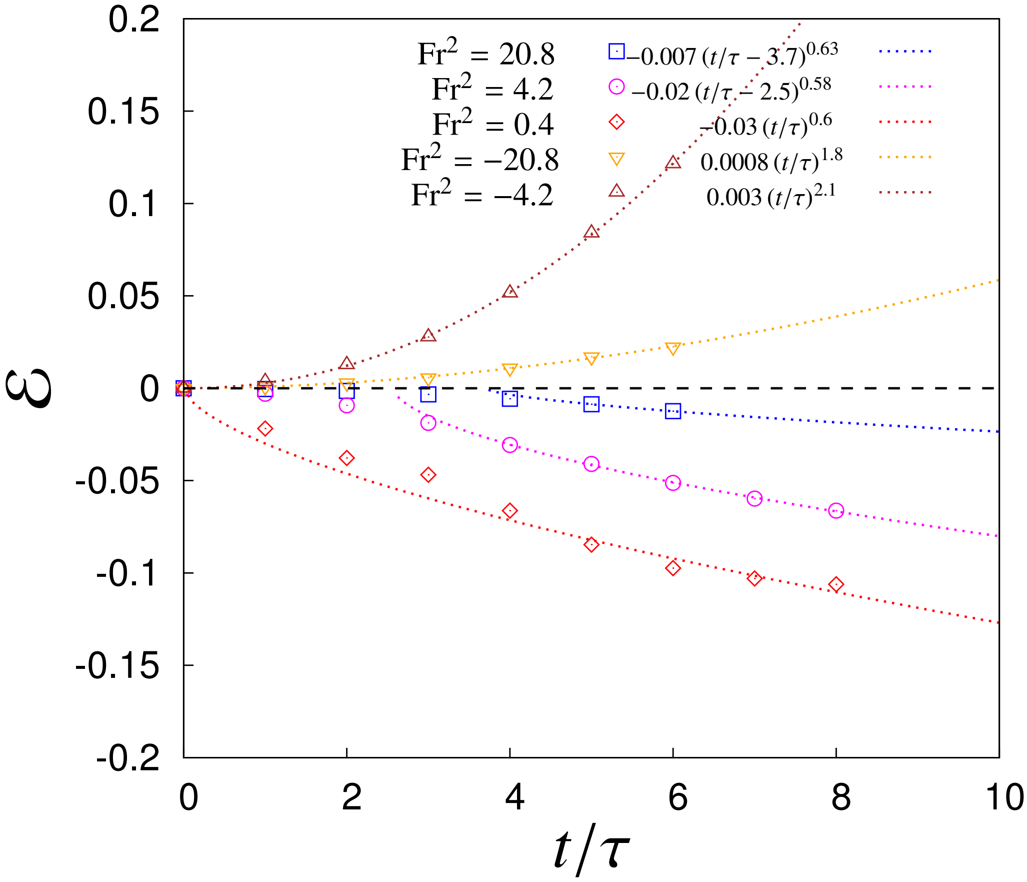

Figure 3.10. Time efolution of the energy variation $\mathcal{E}$, which is defined as the relative energy differece inside the mixing layer respect to the neutral case Fr^2=69.2 (see equation 3.19). Differences tend to follow algebraic trends: in stable cases there is a "loss" of energy inside the mixing, with an exponent is lower than 1 after an initial transition; in unstable cases the exponents is higher than 1, and the initial transition is quite absent.

the low energy region, as it can be observed in panel *a* of figure 3.9 for the case Fr^2=4.2. An opposite behavior can be observed in unstable cases after the peak onset: E_{norm} is 0 in the low energy region, 1 inside the peak sublayer, and < 1 in the high energy region.

Those different energy distribution can be viewed as kinetic energy variation inside the mixing layer of the stable/unstable stratified cases respect to the neutral case Fr^2=69.2. These "loss" or "gain" of energy can be estimated considering the relative kinetic energy variation respect to the neutral case, defined as:

$$\mathcal{E} = \frac{E_{\text{mix}} - E_{\text{mix,Fr}^2=69.2}}{E_{\text{mix}} + E_{\text{mix,Fr}^2=69.2}}, \tag{3.19}$$

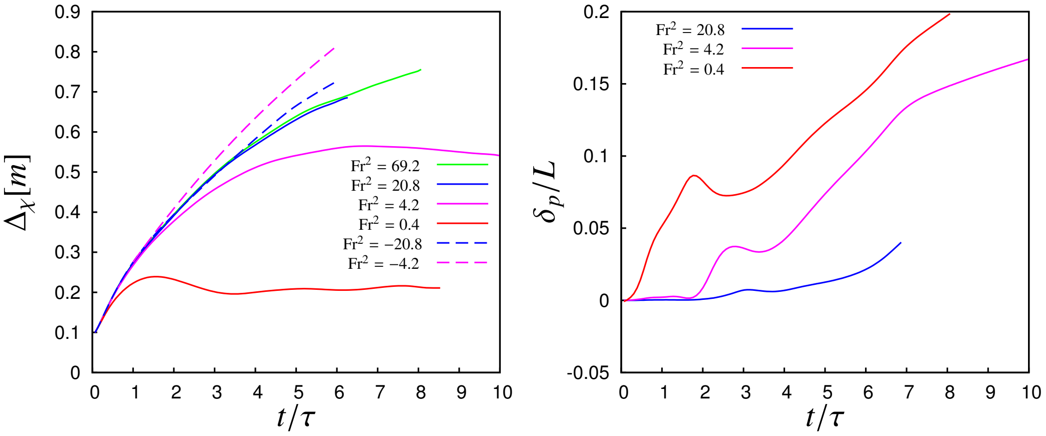

(*a*) Mixing layer thickness (*b*) Pit thickness

Figure 3.11. Panel (*a*) Mixing layer thickness evolution in time both for stable (solid lines) and unstable (dashed lines) interfaces. Definition of δ_E can be found in equation 3.20. Panel (*b*) Time evolution of the width of the kinetic energy pit. Such width is defined as region where the the kinetic energy is lower of the 80% respect to the mean value is the low energy region.

where E_{mix} and $E_{\text{mix,Fr}^2=69.2}$ are the total energy inside the mixing layer of the considered case end the neutral one respectively (see further for the mixing layer thickness δ definition). The time evolution of $\mathcal{E}$ is shown in figure 3.10. It can be seen that in presence of unstable stratification, the relative energy variation increase in time with an algebraic trend; the exponents increase with the increase of the stratification – 1.84 for Fr^2=-20.8, 2.24 for Fr^2=-4.2. In stable cases the situation is more complex: there is an initial transition phase, in which $\mathcal{E}$ decrease with exponent analogous to the one observed for unstable cases. After the initial transition, the is a damping of the grow (in module) rate of $\mathcal{E}$, which follow a different algebraic trend, with exponents lower than 1. This damping is not observed in unstable cases for the time-scale observed. Note that in case of very strong stable stratification (Fr^2=0.4) the initial transition is not present.

We define the pit sublayer as the region where the kinetic energy (averaged in $x_1 - x_2$ planes) is lower than the 80% of the mean energy inside the low energy region E_m. The width of the pit sublayer δ_p is then defined as the distance between the edges of the region identified in this way. and is represented in figure 3.11(a).

Looking at those plot,we can see that the pit of energy appears immediately in the strongest stratified case (in fact Fr^2=0.4 is already lower than 1 in initial conditions) and it continue growing in time. After the initial transition, the pit size grows nearly linearly in time, inversely proportional to the square Froude number. This is in good agreement with the hull length growth found in a stratified Rayleigh-Taylor instability simulation by Biferale *et al.* (2011) and Mellado *et al.* (2009).

A consequence given by the presence of the pit can be seen in the thickness of the mixing layer $\delta = \delta_\chi$. We estimate the thickness of the mixing layer by using the passive scalar distribution, since the complex behavior of the energy field makes it difficult to provide an unambiguous definition for a thickness of the kinetic energy mixing layer δ_E. However, in past work (see Iovieno *et al.*, 2014) it has been shown how δ_χ and δ_E are related. The mixing thickness time evolution is represented in figure 3.11 *(a)*, and defined by

$$\delta_\chi(t) = x_{\text{top}}(t) - x_{\text{bot}}(t) \tag{3.20}$$

where x_{top} and x_{bot} they are such that, considering $\Delta E(t)$ the mean difference of kinetic energy between the two external regions,

$$\langle\chi\rangle(x_{\text{top}}, t) = 0.75 \qquad\qquad \langle\chi\rangle(x_{\text{bot}}, t) = 0.25.$$

It can be seen that the thickness of the mixing layer is still growing during the pit formation. Only after a couple of time scales from the pit onset, the growing stops, with little oscillations around an asymptotic value. A different behavior is observed for unstable stratifications: in these cases the generation of the peak of energy enhance the mixing, providing a faster thickening of the layer, with greater exponents – 0.63 for Fr^2=-4.2, 0.58 for Fr^2=-20.8 – respect to the neutral case for which the exponent is 0.49.

Transport & Entrainment

The entrainment of clear air inside the cloud is an important aspect of the top cloud interface as it concurs in the evaporation/condensation of droplets inside a cloud, see Wood (2012). In any plane parallel to the interface, in absence of a mean velocity, only downward velocity fluctuations can transport clear air into the cloud. Their presence can represented by a marker function ψ that is equal to 1 where u_3 is negative, and 0 otherwise. Outside the mixing region, its mean value is approximately constant and equal to 0.5 ± 0.01, which would be observed in an homogeneous and isotropic flow. On contrary, inside the mixing layer the deviation is greater (up to $\sim \pm 0.05$), with a spatial distribution and a temporal evolution which follow somehow the ones observed in the third order moment of the velocity, see figure 3.7. Figure 3.12 (a) shows the vertical derivative of the downward flux of clear air when $F_r = 1.8$ The downward flux reduces as the flow evolves and its derivative, which represents the net

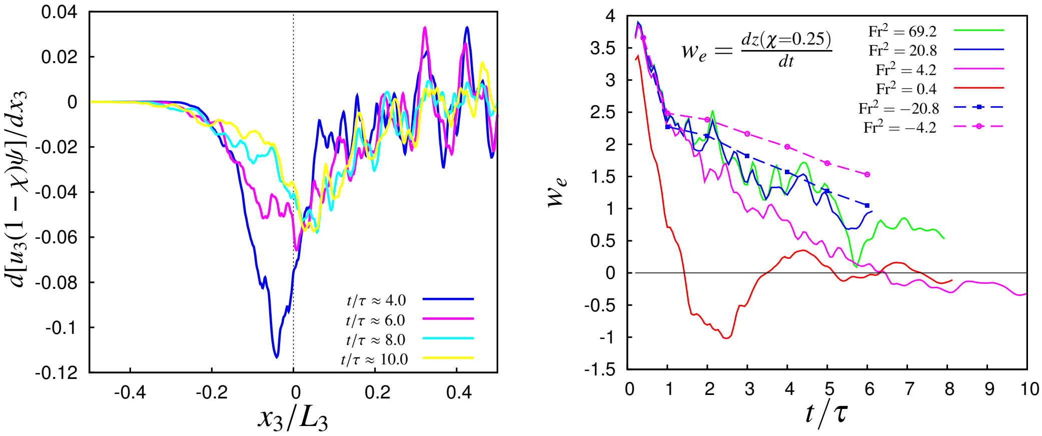

(a) $t/\tau = 4$, vapour flux (b) Entrainment velocity

Figure 3.12. Panel (a): vertical variation of the mean flux of clear air into the cloud; ψ take into account only the regions were the velocity is downward. Panel (b): time evolution of entrainment velocity w_e normalized with the high kinetic energy E_1 root mean square. w_e represent the velocity of the horizontal plane where $\chi = 0.25$. Both stable interfaces (solid lines) and unstable interface (dotted lines) are here represented.

variation of $1-\chi$ at a given instant, rapidly tends to zero inside the cloud; this implies that the entrainment of clear air is confined to a thin interfacial layer.

Since the entrainment of clear air is responsible of the growth of the cloud, it can be quantified considering the velocity with which the cloud expands. In fact, the entrainment velocity $w_e = d\langle x_{3,i}\rangle/dt$ of the cloud top interface (where $\langle x_{3,i}\rangle$ is the mean vertical position of the cloud top,obtained as the position where the mean vapor concentration is 25%) has often been used as a parameter to measure the entrainment rate, see for instance Mellado (2010); Moeng (2000).

In figure 3.12 (b), the time evolution of w_e for different levels of stratification perturbation is represented. In presence of quasi-neutral stratification, its value gradually decreases with an algebraic trend, related to the natural decay of the turbulent kinetic energy; on the contrary, when the a stable, strong stratification is present, the damping of w_e occurs much faster, and the entrainment vanishes after few times scale: note that the entrainment velocity is related to the mixing thickness (see figure 3.11): the presence of the pit of kinetic energy reduces the mixing and transport efficiency. Instead, in case of unstable stratification, the presence of the peak of kinetic energy enhance the mixing, and the entrainment velocity decays slower. As said, a different en-

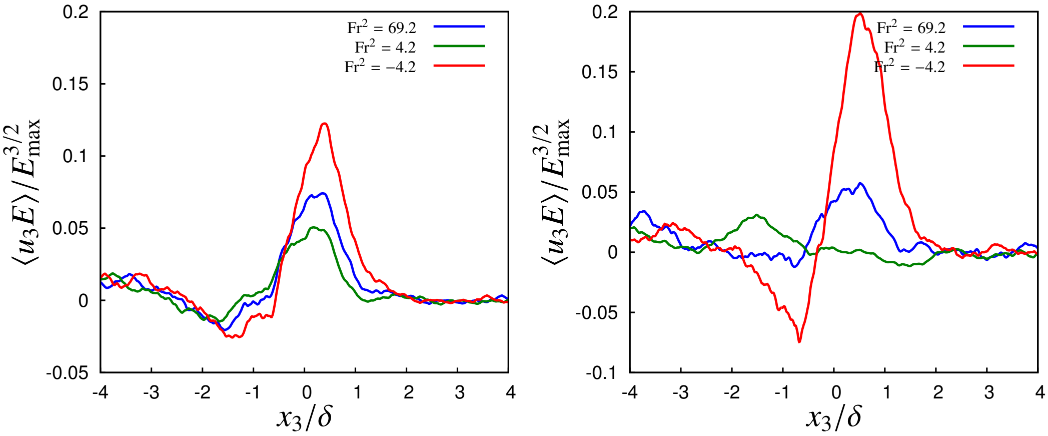

(a) $t/\tau = 3$, kinetic energy flux

(b) $t/\tau = 6$, kinetic energy flux

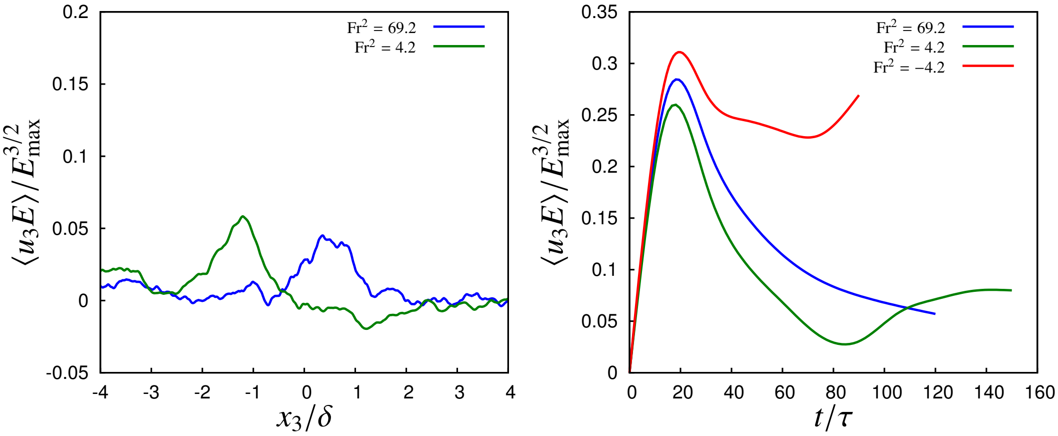

(c) $t/\tau = 8$, kinetic energy flux

(d) Maximum of flux over time

Figure 3.13. Panels $(a$–$c)$: kinetic energy fluxes along the vertical direction x_3, computed through averages in the horizontal planes $x_1 - x_2$, after 4,6, and 8 time scales respectively. Data are taken from different simulation represented by the initial square Froude number $\mathrm{Fr}^2$and normalized with the mean kinetic energy of the external high energy region. Panels d shows the trend of normalized kinetic energy flux maximum over time.

trainment determine different mixing efficiency for all the physical quantities, deeply affecting kinetic energy flux, shown in figure 3.13, and passive scalar flux, shown in figure 3.14.

Compared to neutral case, the presence stable or unstable stratification produce an initial reduction/increase of the energy flux respectively, with a maximum flux alway positioned around $x_3/\delta = 1$, see 3.13. In case of stable stratification, the flux decrease until it reaches values around zero; it can be then observed the formation of two fluxes, according to the experimental results

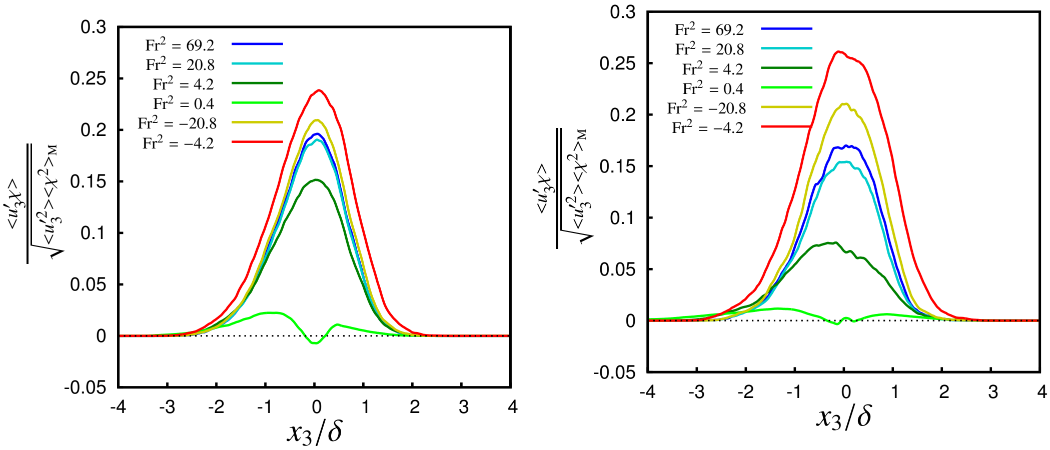

(*a*) $t/\tau = 3$, scalar flux

(*b*) $t/\tau = 8$, scalar flux

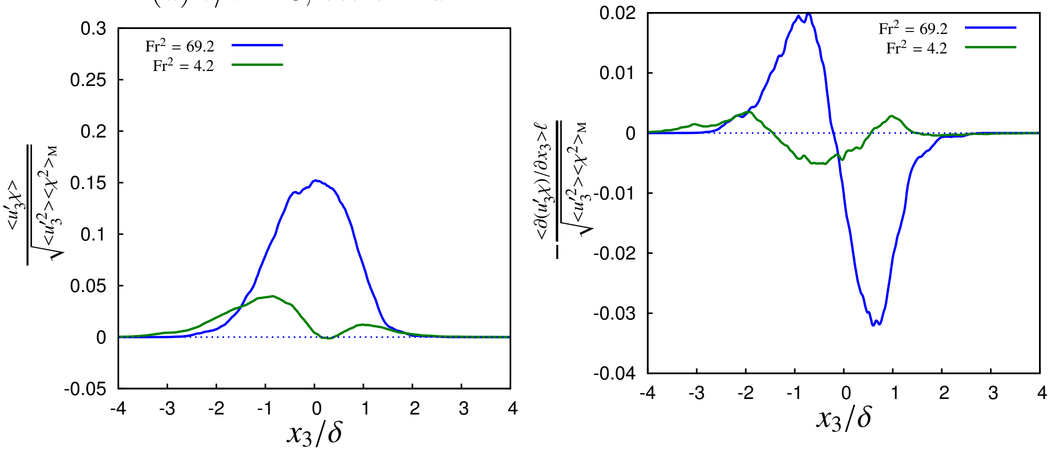

(*c*) $t/\tau = 6$, scalar flux

(*d*) $t/\tau = 8$, derivative of scalar flux

Figure 3.14. Passive scalar flux along the vertical direction x_3, computed through averages in the horizontal planes $x_1 - x_2$. Panels (*a*–*c*) refer to data taken after 4, 6, and 8 initial eddies turnover time τ. Panel (*d*) shows the derivative along the vertical direction of the scalar flux at $t/\tau = 8$, highliting the presence of two separate regions with negative derivative.

of Jayesh & Warhaft (1994). The first one, located below the pit at $x_3/\delta = -1$, is positive (upward flux), and the second one, located above the pit at $x_3/\delta = 1$, is negative (downward flow) – see figure 3.13*c* and time evolution in figure 3.13*d*. The ratio between the two flux is around 0.25 for Fr^2=4.2. In between these two, no mean flux is present: this mean that the energy tends to accumulate at the pit edge without being able to pass across it, bounding the mixing thickness to a fixed dimension. In case of unstable stratification, while the flux located at $x_3/\delta = 1$ keeps growing, it can be observed the formation of a secondary negative flux located at $x_3/\delta = -1$. In that case the energy is spread from the peak sublayer to the external region, promoting the mixing layer thickening.

A coherent behavior affects the passive scalar flux, shown in figure 3.14. The unstable stratification exalts the flux, which becomes increasingly important compared to the scalar variance, but without suffering any change in the spatial behavior, except for the magnitude: the flux is always directed towards the upper region. Instead, important differences can be found in case of stable stratification: after an initial damping, the flux become zero or even negative in the center of the mixing layer (see Fr^2=0.4 in figure 3.14(a, and see Fr^2=0.4 in figure 3.14(c), according to experimental results by Jayesh & Warhaft (1994). In particular, it can be observed the flux derivative along the vertical direction, shown in figure 3.14(d). A positive derivative can be interpreted as entrainment of clear air (passive scalar moves away), while a negative, see derivative implies a detrainment of clear air (passive scalar moves into) Ma & Warhaft (1986). In case of neutral (and unstable) stratification, the mixing acts moving the scalar upwards, where initially is not present. Under a stable stratification, there are two sub-layer with positive derivative which surround a sublayer with negative derivative: the scalar is retained within the mixing layer.

The reduction of communication between the two external region can be also observed looking at the streamline, represented in figure 3.15 for three case: neutral Fr^2=69.2, stable Fr^2=4.2, and unstable Fr^2=-4.2. All the streamlines are computed at a distance of $2\delta_0$ above (red) and below (blue) the mixing layer, after 6 initial eddy turnover time. It is possible to observe that in neutral case,where the buoyancy forces are negligible respect to the kinetic ones, streamlines from the upper side can cross the interface to reach the lower region, and viceversa. In presence of stable stratification this is no longer true: in this case the crossing of the interface becomes increasingly rare, and what is located on one side of the interface, tend to stay there. On contrary, in presence of unstable stratification, the mixture is enhanced, which means that the streamlines cross the interface more frequently.

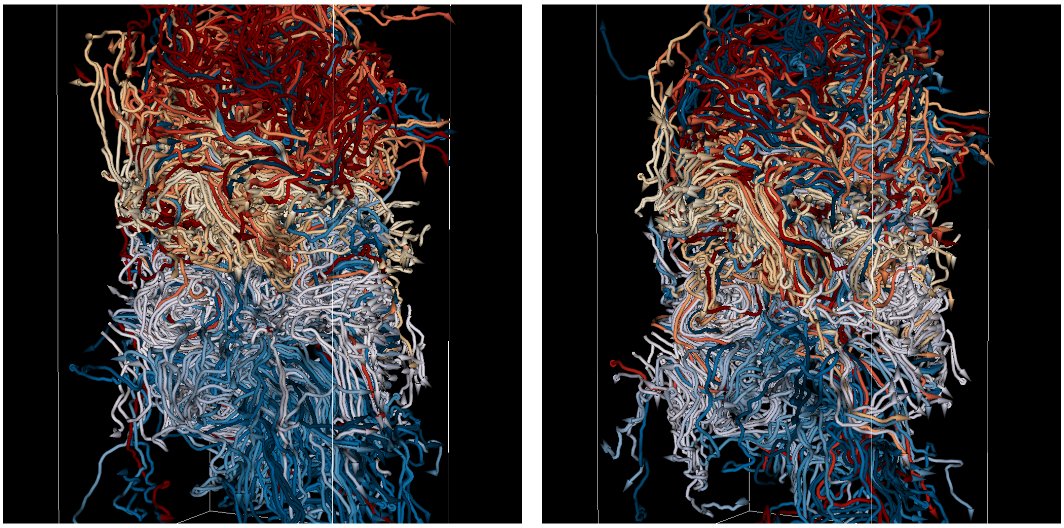

(a) Fr^2=4.2 (b) Fr^2=-69.2

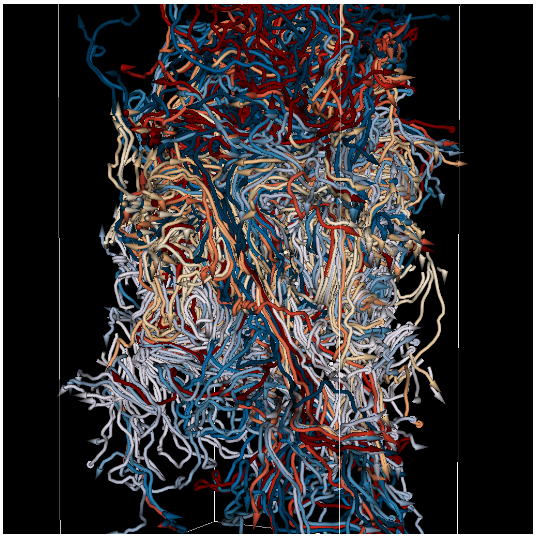

(c) Fr^2=4.2

Figure 3.15. Streamlines after 6 time scales for different stratification level – (a) Fr^2=4.2 strong stable, (b) Fr^2=69.2 neglicible stratification, (c) Fr^2=-4.2 strong unstable. The starting position of each streamline is placed at a fixed distance from above (yellow/red tubes) and below (cyan/blue tubes) the center of the interface. In panel (b), where the buoyancy forces are neglicible respect to the kinetic ones, streamlines from the upper side can cross the interface to reach the lower region, and viceversa. On the contrary in panel (a), where stable stratification effects are relevant, the crossing of the interface becomes increasingly rare: what is located on one side of the interface, tend to stay there, and the mixing process is damped. Finally, in case of unstable stratification, shown in panel (c), the mixture of red and blue line is enhanced, which means that the streamlines cross the interface more frequently.

3.4.3 Flow structure: effects on anisotropy, dissipation and spectra evolution

Anisotropy

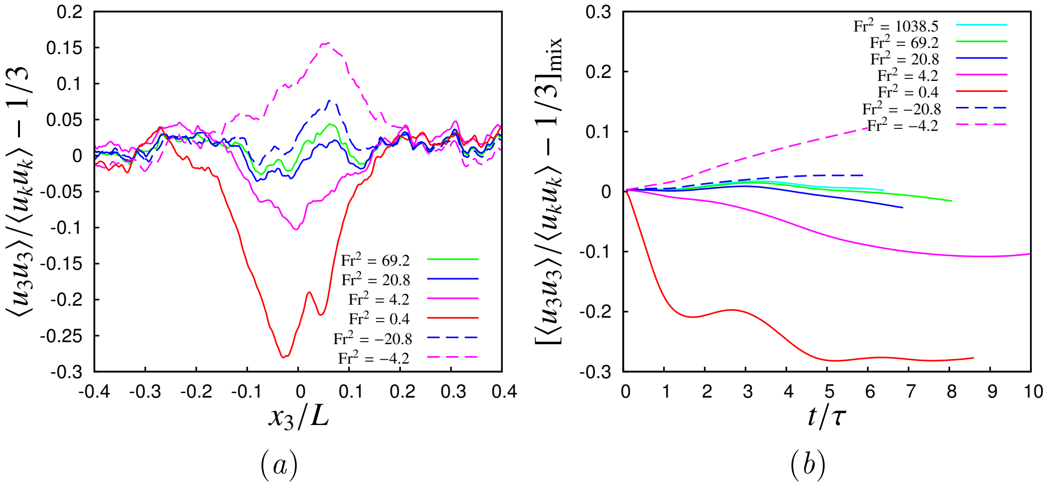

Figure 3.16. Skewness of the longitudinal derivatives. (*a*) Spatial distribution of the skeness of longitudinal derivatives normal to the mixing surface (solid lines) and parallel to the mixing interface (dashed line) and (*b*) Evolution of the mean peak value of normal derivative around $x_3/\delta \approx 1$.

Since buoyancy forces acts directly only on the vertical component of the velocity field, an anisotropic behavior is expected in the large scale range. To evaluate the large scale anisotropy, we consider the relative weight of the energy associated to the vertical velocity respect to the other components (Pope, 2000), using the ratio

$$B_3 = \frac{u_3^2}{u_1^2 + u_2^2 + u_3^2} - \frac{1}{3}.$$

Figure 3.16 shows the behavior of B_3 along the vertical direction (panel *a*), and the time evolution of the peak value in time. Under neutral stratification condition, the anisotropy in large-scale is present, but limited, with maximum deviation of the order of 5%. In presence of a stratified layer, the anisotropy becomes very strong: in particular it is possible to observe how the vertical velocity is more affected by the stratification effects respect to the other two components, in particular with a greater dumping in stable stratification ($\langle u_3^2\rangle < \langle u_{1,2^2}\rangle$) and higher energy in unstable stratification ($\langle u_3^2\rangle > \langle u_{1,2^2}\rangle$). Those difference are responsible of the different behavior in transport and fluxes observed in previous section. In figure 3.16*a* it is also possible to observe that the variation concern all the mixing layer (and not only the previous defined pit/peak of kinetic energy). In fact, together with the formation of such sublayer, it was observed a displacement of the main energy gradient, depending on whether the stratification is stable or unstable.

The small scale anisotropy of the flow can be represented by the higher moments of the first order, longitudinal derivative of the velocity components (Sreenivasan & Antonia, 1997). It is well known that HIT departs from gaussianity at small scale, and in particular the longitudinal derivative skewness $S(\partial u_i/\partial x_i) = -0.5 \pm 0.1$, with small dependency on Reynolds number (see Sreenivasan & Antonia, 1997). In previous work [Tordella *et al.* (2008); Tordella & Iovieno (2011)] it has been found that in presence of a mixing layer due to a mean kinetic energy gradient, $S(\partial u_i/\partial x_i)$ becomes no longer isotropic, showing even greater magnitude in the mixing direction ($S(\partial u_3/\partial x_3)$), and slightly lower values (in magnitude) in the parallel directions ($S(\partial u_{1,2}/\partial x_{1,2})$). The level of anisotropy depends, in addition to the Reynolds number, also from the energy gradient, see Tordella & Iovieno (2011).

The presence of buoyancy forces does not influence directly the tilting/stretching of the vortex filament: considering the vorticity equation, obtained as the curl of equation 3.15b)

$$\frac{\partial \boldsymbol{\omega}}{\partial t} + (\boldsymbol{u} \cdot \boldsymbol{\nabla})\,\boldsymbol{\omega} = (\boldsymbol{\omega} \cdot \boldsymbol{\nabla})\,\boldsymbol{u} + (\boldsymbol{u} \cdot \boldsymbol{\nabla}) + \nu \boldsymbol{\nabla} \times \nabla^2 \boldsymbol{u} + \alpha \boldsymbol{\nabla} \times (\boldsymbol{g}\theta) \tag{3.21}$$

where the compressibility stretching and the baroclinic term have been neglected according to incompressibility and Boussinesq approximation. Considering that the buoyancy forces term is a vector which has only the third component different from 0, its curl have only the first two component, which depends on the derivative along direction parallel to the mixing:

$$\alpha \boldsymbol{\nabla} \times (\boldsymbol{g}\theta) = \alpha \boldsymbol{\nabla} \times \begin{pmatrix} 0 \\ 0 \\ g\theta \end{pmatrix} = \alpha g \begin{pmatrix} \partial\theta/\partial x_2 \\ \partial\theta/\partial x_1 \\ 0 \end{pmatrix}. \tag{3.22}$$

Since a mean variation of θ occurs only along direction 3, there is no mean contribution of buoyancy to the vorticity equation and in HIT stratification does not influence the small-scale anisotropy.

This is no longer true for a mixing: in particular, it has been found that a shear-less mixing present anisotropy at small-scales, with $S(\partial u_3/\partial x_3) < S(\partial u_{1,2}/\partial x_{1,2})$ inside the mixing region, with peaks toward the lower energy region (at $(x_3 - x_c)/\delta \approx 1$). Figure 3.17 and 3.18 shows how the presence of stratification modifies the behavior of the longitudinal derivatives skewness and kurtosis. Mild stratification does not affect the small-scale anisotropy: the skewness of $\partial u_3/\partial x_3$ tends to an asymptotic value of -0.63 ± 0.02, as expected for $\mathrm{Re}_\lambda \approx 200 \div 250$ (Tordella & Iovieno, 2011; Shen & Warhaft, 2000). In case of stable stratification, all the longitudinal derivatives skewness tend to the isotropic value of 0.52, while in case of unstable stratification $S(\partial u_3/\partial x_3)$ tends to diverge, reaching values as low as -0.75, with an overgrowth of the order of 30%.

Those variations are related to the influence on mixing intensity due to the stratification. In case of stable stratification, the mixing initially is present, although it is slightly dumped respect to the neutral case: this leads to a slower formation of the anisotropic sublayer in the very initial time-scales, as can be seen in figure 3.17(b) . Afterwards, as soon as the pit appears, the mixing intensity decrease, and the small-scale anisotropy sublayer tends to disappear, behaving as if the energy gradient is not present – pointing out the idea that the exchange of information between the two outer regions becomes blocked. On contrary, in case of unstable stratification the mixing is enhanced, and the mixing layer becomes even more anisotropic at small scales, acting as if the energy gradient be greater.

Derivatives along homogeneous direction does not show peaks in the center of the mixing layer, according to the results from Tordella & Iovieno (2011), considering that the Re_λ is 250 in the present cases.

The statistical behavior of the derivative normal to the mixing layer, i.e. $\partial u_3/\partial x_3$, shows the presence of a peak inside the mixing layer, as shown in figure 3.18.

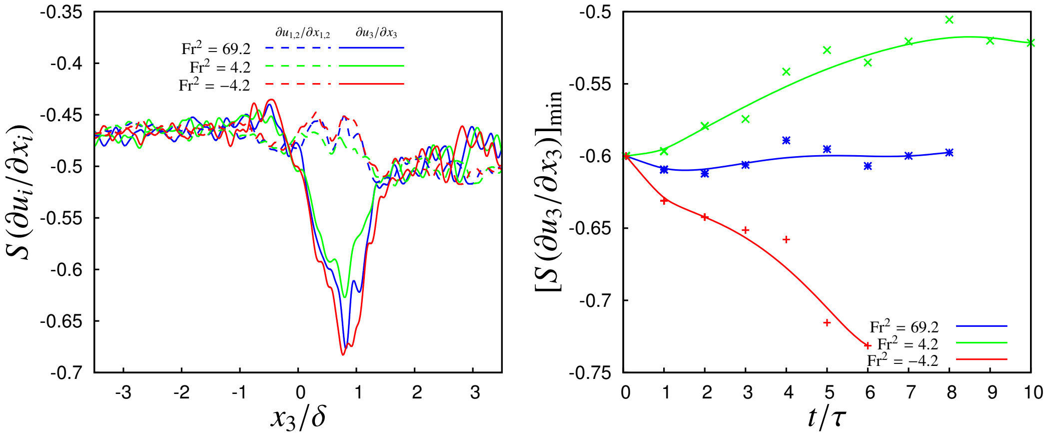

(a) (b)

Figure 3.17. Skewness of the longitudinal derivatives. (a) Spatial distribution of the skeness of longitudinal derivatives normal to the mixing surface (solid lines) and parallel to the mixing interface (dashed line) and (b) Evolution of the mean peak value of normal derivative around $x_3/\delta \approx 1$.

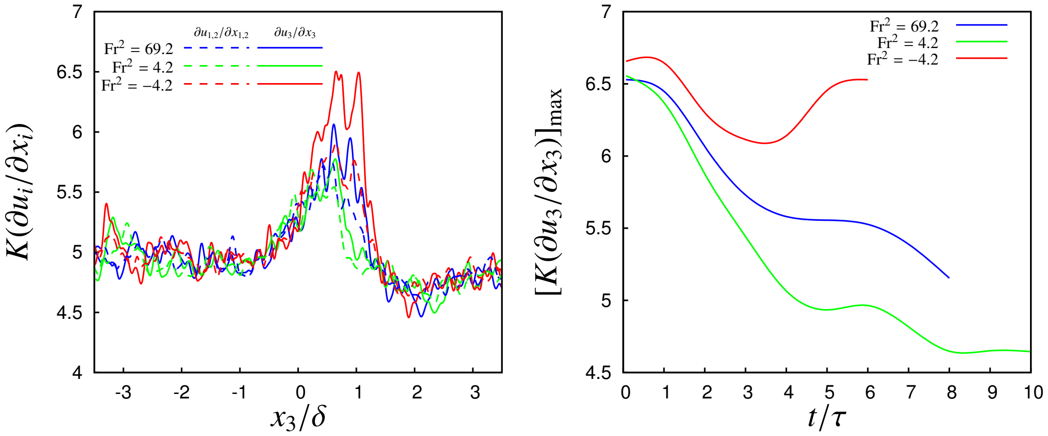

Figure 3.18. Kurtosis of the longitudinal derivatives. (a) Spatial distribution of the kurtosis of longitudinal derivatives normal to the mixing surface (solid lines) and parallel to the mixing interface (dashed line), and (b) evolution of the peak value of normal derivative around $x_3/\delta \approx 1$.

Dissipation

The dissipation rate is computed in the whole domain by using the general definition (see Tennekes & Lumley, 1972, p.64)

$$\varepsilon = \frac{1}{2}\nu\left(\frac{\partial u_i}{\partial x_j} + \frac{\partial u_j}{\partial x_i}\right)^2 . \tag{3.23}$$

In figure 3.19 the plot of the normalized turbulent dissipation rate C_ε, defined as

$$C_\varepsilon(x_3) = \frac{\langle\varepsilon\rangle\langle\ell\rangle}{\langle E\rangle^{3/2}}$$

and considering plain-averages in direction x_1, x_2.

It can be observed that the normalized dissipation rate initially has a constant value in the whole domain, equal to 0.55 ± 0.05. This means that there are not relevant differences respect to the unstratified case, actually there are not difference also in comparison with an homogeneous isotropic turbulence, as in that case C_ε tents to 0.5 for sufficiently high values of Re_λ (see Burattini *et al.*, 2005). As the buoyancy term becomes relevant, the formation of a "peak" of dissipation can be observed downstream of the mixing interface, inside the pit of kinetic energy, where C_ε reaches values as high as 0.9. In this region, the kinetic energy is damped by the stratification effects; also the dissipation is affected by the buoyancy, but to a lesser extent: as result, the dissipation becomes relatively larger in such sub layer. This can be explained considering that the stratification affects directly only the energy of the vortices, and not the spatial geometry, which is only indirectly influenced. This assumption is in agreement with the probability density function reported in figure 3.19(b), which shows how in different regions of the system the statistical behavior of the dissipative rate remains always similar inside and outside the mixing sublayers.

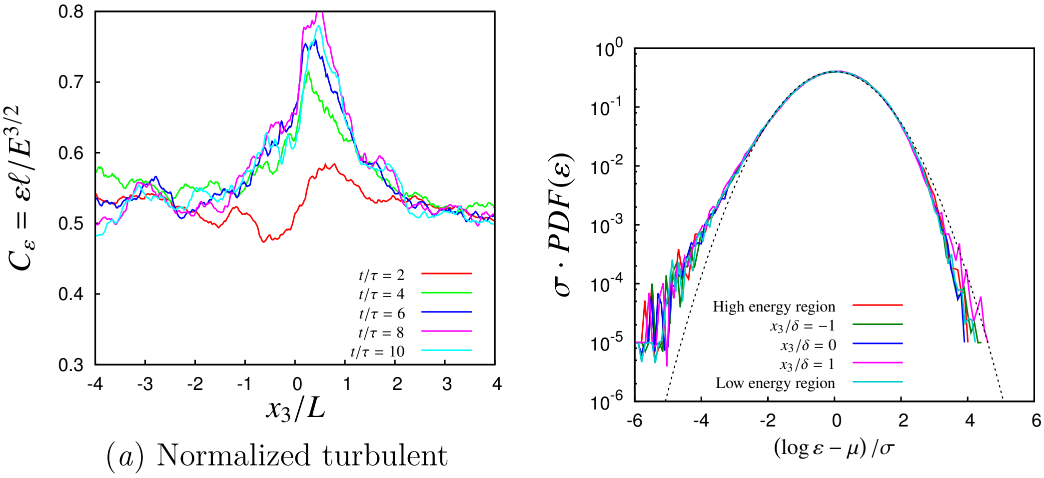

(a) Normalized turbulent dissipation rate

(b) Dissipation PDF's

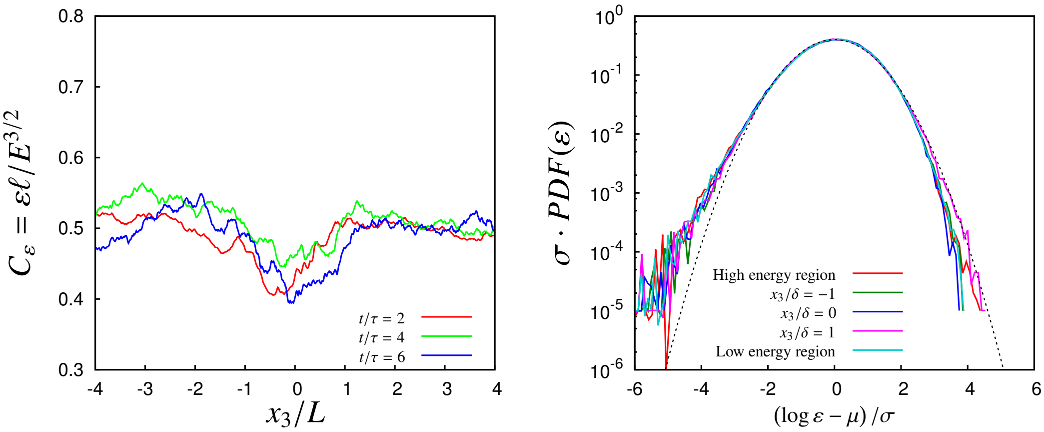

(a) Normalized turbulent dissipation rate

(b) Dissipation PDF's

Figure 3.19. (a,c) Normalized plane-averaged dissipation $C_\varepsilon = \{\epsilon\}\ell/\{E\}^{3/2}$ for the case with Fr^2=4.2 and Fr^2=-4.2 respectively. Dissipation values outside the mixing layer are near to 0.5, like for isotropic homogeneous turbulence (see Burattini *et al.*, 2005). For stable case, the normalized dissipation has a maximum in correspondence of the kinetic energy pit; for unstable case the dissipation has a minimum in correspondance of the peak of energy. (b-d) Normalized log-normal probability density function of dissipation rate in several $x_1 - x_2$ planes for case Fr^2=4.2 and Fr^2=-4.2 at $t/\tau = 6$.

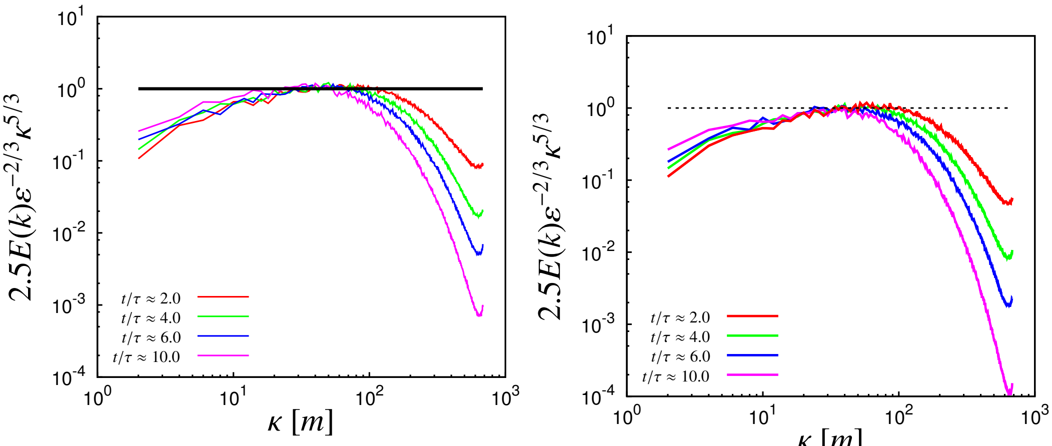

(a) High energy region ($x_3/L = -0.50$)

(b) Mixing region ($x_3/L = 0.00$)

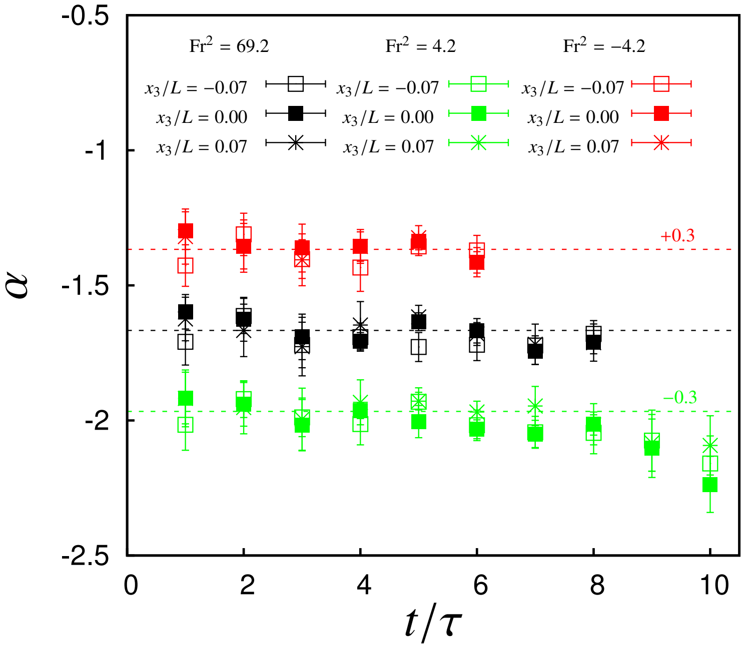

Figure 3.20. Panels (a–b)Kinetic energy spectra at different instant for the case with Fr^2=4.2. Spectra are compensateded according to the Obukov–Corrsin normalization, in which $E(\kappa) = 0.4\epsilon^{-2/3}\kappa^{-5/3}$. Panel ($a$) shows the spectra in the high energy region, while panel (b) in the centre of the mixing layer. Panel (c) Evaluation of the spectra exponent in the inertial range at different position of the vertical direction x_3. Three different stratification are represented: unstratified case (Fr^2=69.2, black), stably stratified (Fr^2=4.2, green, shifted downwards by 0.3) and unstably stratified (Fr^2=-4.2, red, shifted upwards by 0.3). The dotted lines represents the standard -5/3 Kolmogorov slope. Errorbars represent the uncertainity of the linear regression which estimate the exponent in a log-log plane.

Spectra

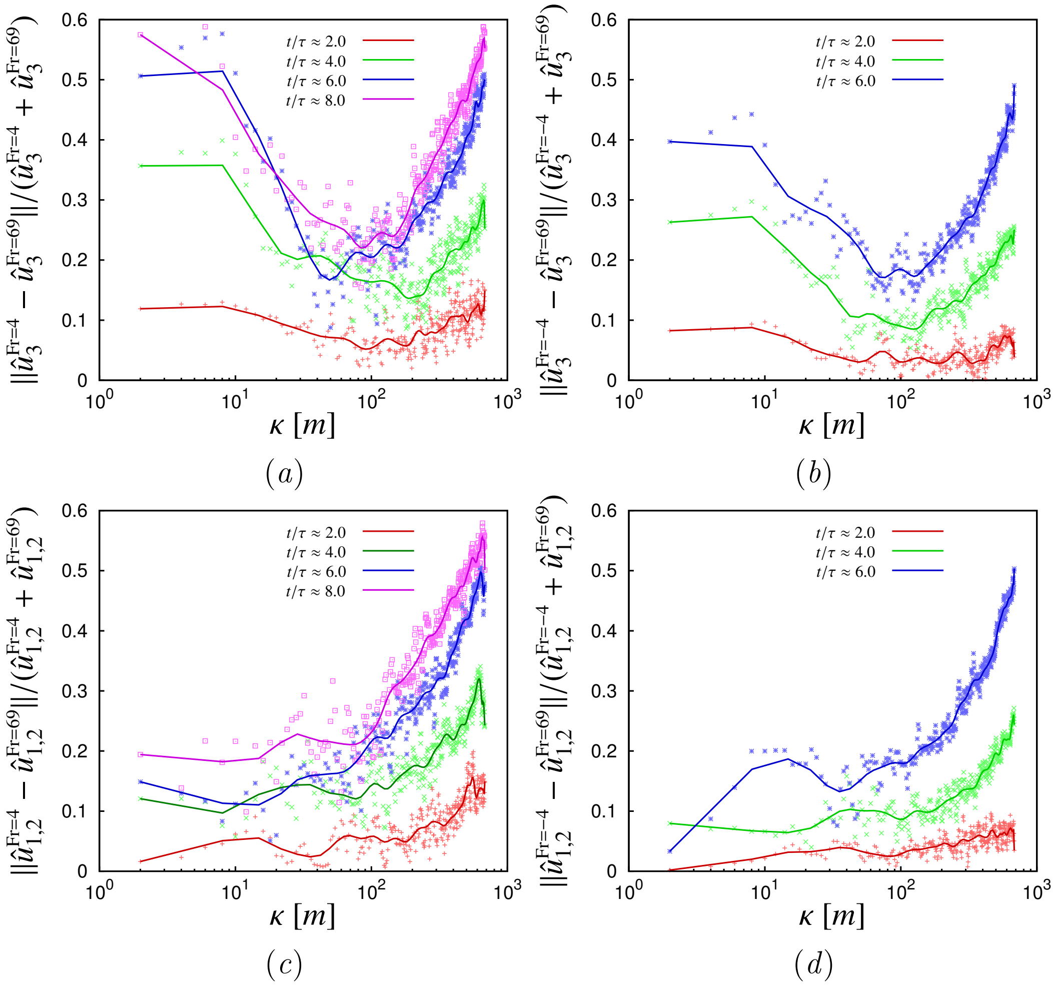

(*a*) (*b*)

(*c*) (*d*)

Figure 3.21. Comparison of 1-dimensional velocity spectra along the homogeneous directions. Panels (*a*–*b*) shows the effects on vertical velocity in presence of stable (*a*, Fr^2=4.2) and unstable (*b*, Fr^2=-4.2) stratification, in comparison with the neutral case Fr^2=69.2. Panels (*c*–*d*) shows the effects on the other two velocity components. Spectra are computed inside the mixing layer, at $x_3/\delta \approx 0.8$

Defining $\tilde{E}(\kappa)$ as Kolmogorov normalized normalized spectra for turbulent velocity:

$$\widetilde{E}(\kappa) = 2.5E(\kappa)\varepsilon^{-2/3}\kappa^{5/3} \tag{3.24}$$

The Kolmogorov -5/3 scaling is respected in the whole domain: the inertial range is very small, and its extent becomes lower than una decades for $t/\tau > 6$.

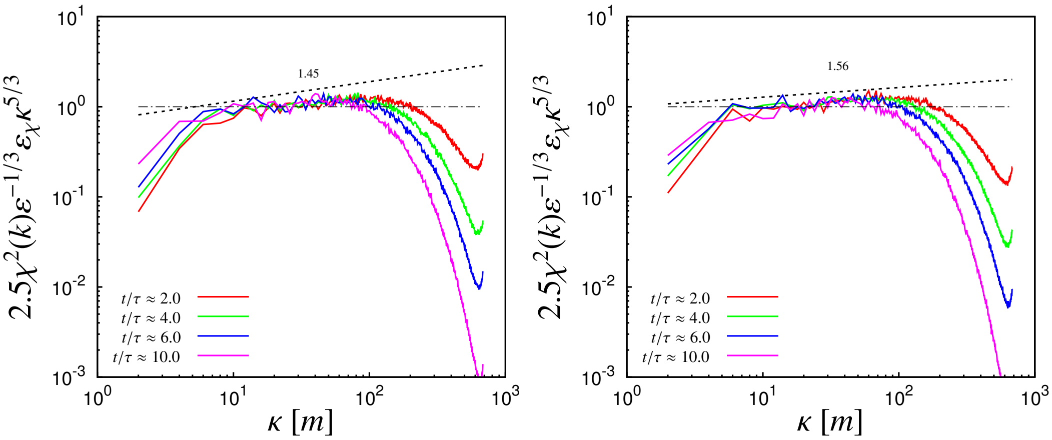

$(a)\ x_3/L_3 = -0.07$ $(b)\ x_3/L_3 = 0.00$

Figure 3.22. Passive scalar power spectra inside the mixing layer at different position along the vertical direction x_3, computed through averages in the horizontal planes $x_1 - x_2$. Data taken for the case with Fr^2=1.8.

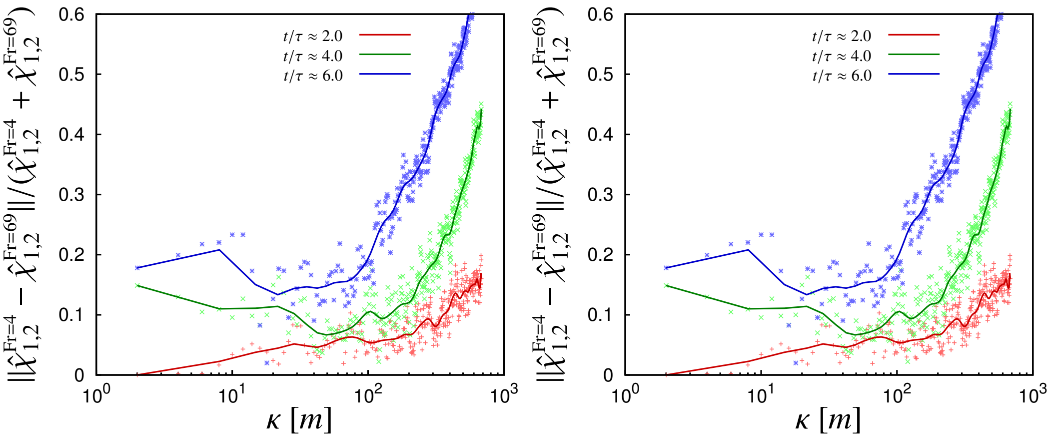

(a) (b)

Figure 3.23. Comparison of 1-dimensional passive scalar spectra along the homogeneous directions in case of stable (panel a, Fr^2=4.2) and unstable (panel b, Fr^2=-4.2) stratification, in comparison with the neutral case Fr^2=69.2. Spectra are computed in the center of the mixing layer, at $x_3/\delta \approx 0.0$

The normalized kinetic energy spectra are almost similar along the vertical direction, with little deviations due to the different Reynolds number.

They are also quasi-selfsimilar in time, with the main difference represented by a reduction of the inertial range extension due to the increase of the Kolmogorov scale - and so the dissipative range.

We synthesize the exponent evaluation in figure 3.20*c*, where exponent of the inertial range are reported in function of time time for three different stratification level (stable, unstable and neutral); the values in case of stable and unstable stratification are displaced by ±0.3 to obtain a better representation. Exponent are estimated taking advantage of the linear regression method, applied to the spectra in a log-log space. The inertial ranges are chosen minimizing the regression error, under the condition to have at least half decade in each inertial range. The error-bars in figure 3.20*c* represent the residual.

It is possible to observe that velocity spectra always tend to the Kolmogorov $-5/3$ slope, independently from position inside the mixing layer and from the stratification effects. The decrease of α for the stably stratified case at $t/\tau > 8$ is given by the absence of a well determined logarithmic scaling, since the inertial range vanishes because of the increase of the dissipative range, as previously shown in figure 3.20 (*a*).

The major influence of the presence of a stratified layer occurs outside at the edges of the inertial range. This influence can be evaluated comparing with the neutral case the 1-dimensional spectra of each velocity component inside the mixing region. To achieve this, we compute spectra $\hat{u}_i(k, x_3)$ as the average of the transform along each of the two homogeneous direction, that is

$$\hat{u}_i(k, x_3) = 0.5\langle \hat{u}_i(k_1, x_2, x_3)\rangle + 0.5\langle \hat{u}_i(x_1, k_2, x_3)\rangle \qquad k = k_1 = k_2 \qquad (3.25)$$

where the average operator $\langle \bullet \rangle$ acts along the homogneous direction on which it has not been carried out the transform. The obtained spectra are then compared to the neutral case Fr^2=69.2 considering the relative variation

$$\frac{\hat{u}_i^{\mathrm{Fr}^2=\dots} - \hat{u}_i^{\mathrm{Fr}^2=69.2}}{\hat{u}_i^{\mathrm{Fr}^2=\dots} + \hat{u}_i^{\mathrm{Fr}^2=69.2}}.$$

Results of such comparison are shown in figure 3.21 for the stable case Fr^2=4.2 (panels *a,c*) and the unstable case Fr^2=-4.2 (panels *b,d*). The fist relevant observation which can be done is the different behavior of the vertical velocity respect to the other two components: in particular, the behavior is the following.

The stratification directly acts only on larger scale of the vertical motion, generating a relative deviation from the neutral case. Such variation is negative (less energy in vertical motion) in presence of stable stratification, and positive (more energy) for unstable stratification, in agreement with what observed for large scales anisotropy. While the mixing evolves, these effects are transmitted to smaller scales through the inertial cascade, reaching the dissipative range, with the consequent effect of enhancing/dampening the dissipation rate for stable/unstable stratification respectively. In this scale range, the stratification effects are widespread to all the velocity components: as a consequence, absolute small-scale differences (and so small scale anisotropy) are dumped in presence of stable stratification, and enhanced in unstable cases, as pointed out in section 3.4.3.

Considering the scalar fields, the dimensionless spectra are defined by

$$\widetilde{\chi^2}(\kappa) = 2.5\widehat{\chi}^2(\kappa)\varepsilon^{1/3}\epsilon_\chi^{-1}\kappa^{5/3} \tag{3.26}$$

where ε_χ is the pseudo-dissipation of the temperature field. Looking at the spectra in presence of a strong stratification, shown in figure 3.22, it can be observed that the behavior is very similar to the one in absence of buoyancy effect (see section 2.4 in the previous chapter), and the spectral exponent tends to value around -1.66 after an initial transient. Differences among different stratification levels can be found in the dissipative range, in a way similar to that observed for the velocity components parallel to the mixing interface, as reported in figure **??**. Large scales and inertial range are almost unaffected by the buoyancy, while dissipative range comes to undergo an high influence, comparable to the one observed for the homogeneous velocity.

3.5 Conclusion remarks

The evolution of a shearless turbulent mixing layer obtained coupling two homogeneous isotropic turbulent field with different kinetic energy has been studied, evaluating the effects of the presence of a temperature stratification inside the mixing layer, both under stable and unstable stratification condition. It has been observed that the presence of a sufficiently intense stratification (so with a Froude square number of the order of 1) deeply changes the mixing dynamics.

First of all, it has been observed the formation of a sub-layer inside the mixing region: such sub-layer onset and evolution is strictly related to the stratification intensity and stability. In particular, under stable condition of stratification the sub-layer behaves as a pit of kinetic energy: it is characterized by lower level of energy respect to the external regions. On contrary, under unstable conditions of stratification the energy becomes higher than in the external regions with the formation of a peak of kinetic energy. The time evolution of the energy variation inside the mixing region has been quantified: it has been found that it follows and algebraic laws, with exponent which depends on the stratification intensity.

In particular, a stable stratification tends to suppress vertical motion, since fluctuations within it are inhibited by the buoyancy forces. In fact, in this condition there is a strong large-scale deviation from isotropy, with vertical component of velocity which differs from the other two: as stated, stable stratification suppress vertical motion, and the energy associated to vertical fluctuations becomes smaller compared to the other components. On contrary, in unstable conditions vertical fluctuations becomes greater respect to the other two.

As a consequence, in presence of a stable stratification follows a general damping of the mixing and its relative effects, i.e. intermittency energy/scalar transports, entrainment/detrainment, and small scale anisotropy. By contrast, unstable stratification enhance the mixing process. In particular the entrainment, which assumes an high importance in atmospheric phenomena, tends to vanish very quickly when the Froude square number becomes lower than 1 – in absence of stratification, the entrainment disappears following an inertial law, due to the natural decay of the turbulent energy.

For what concern the small-scale anisotropy, it has been found that the presence of an unstable stratification increases the differences in the statistical behavior among the longitudinal velocity derivatives. As a consequence, the compression of the fluid filaments normal to the interface is greater, due to the increased mixing intensity. In stable cases, since the mixing tends to vanish, so does the small-scale anisotropy.

Finally, it has been observed how the stratification, which acts directly on large scales of vertical direction, also influences the dissipative range of all the velocity components and scalar field, with only small effects on the inertial range, without changing the spectral indices.

Chapter 4

Numerical method

Numerical simulations have been performed considering the incompressible Navier-Stokes equation in its dimensionless form

$$\begin{cases} \nabla \cdot \mathbf{u} = 0 & (4.1) \\ \dfrac{\partial \mathbf{u}}{\partial \tilde{t}} + (\mathbf{u} \cdot \nabla)\,\mathbf{u} = -\nabla p + \dfrac{1}{Re}\nabla^2 \mathbf{u} + \mathbf{f} & (4.2) \\ \dfrac{\partial \theta}{\partial \tilde{t}} + \mathbf{u}\nabla\theta = \dfrac{1}{Sc\ Re}\nabla\theta. & (4.3) \end{cases}$$

where $\mathbf{f}$ is the sum of external forces (such as buoyancy force).

The continuity equation is used in order to explicitly compute the pressure field. In particular, applying the divergence operator on the momentum equation, and considering that time and spatial derivative can be exchanged, we have:

$$-\frac{\partial}{\partial t}\nabla \cdot \mathbf{u} + \nabla \cdot \left[\frac{1}{\mathrm{Re}}\nabla^2 \mathbf{u} - (\mathbf{u} \cdot \nabla)\,\mathbf{u} + \mathbf{f}\right] = \nabla^2 p.$$

The time-dependent term drops because of the divergence of velocity field is zero, as in equation (4.1). Reordering the remaining terms, we obtain the Poisson equation for the pressure:

$$\nabla^2 p = \nabla \cdot A'(\mathbf{u}) \tag{4.4}$$

where $A'(\mathbf{u})$ is a non-linear operator composed by the sum of convection, diffusion and external terms. Equation (4.4) can be used to evaluate the pressure in terms of velocity (and external forces), leaving as unknown the velocity field (and eventually scalar quantities).

The mathematical structure of the problem leads naturally to the adoption of a spectral discretization, and in particular to a Fourier-Galerkin method (Iovieno *et al.*, 2001). The spectral method is the most accurate method since using it to compute an infinitely smooth solution the numerical error decays exponentially rather than algebraically as the resolution is increased (Jameson *et al.*, 1981).

Acting on a discrete field, since the computation grid is equispaced, direction x_1, x_2 and x_3 will have respectively N, N and N_3 points. In spectral (Fourier) space each point will contain the value referring to the triple of wave-numbers (k_1, k_2, k_3) where

$$-N/2 \leq k_j < N/2 \quad \forall j$$

.

The expansion of the variables in a Fourier-Galerkin series can be written as wave-numbers:

$$y(\mathbf{x}, t) = \frac{1}{2\pi} \sum_{j_3=0}^{N_3-1} \sum_{j_1,j_2=0}^{N-1} \hat{y}_{\mathbf{k}}(t) \exp\left(i\mathbf{k} \cdot \mathbf{x}\right) \tag{4.5}$$

and the discretized system is given by

$$\begin{cases} \dfrac{\partial \hat{u}_i}{\partial t} = -\dfrac{k_i k_l}{k^2}\left(-Re^{-1}k^2\hat{u}_j - ik_j\widehat{u_l u_j} + \widehat{f_i}\right) - ik_j\widehat{u_i u_j} - Re^{-1}k^2\hat{u}_i + \widehat{f_i} & (4.6) \\ \dfrac{\partial \hat{\theta}_i}{\partial t} = -ik_j\widehat{u_j\theta_i} - Sc^{-1}Re^{-1}k^2\hat{\theta}_i. & (4.7) \end{cases}$$

where exponential parts have been simplified, the pressure rewritten in terms of velocity, and the summation operators omitted (each equation in fact a subsystem for the $N^2 \times N_3$ weight function). The time integration is achieved by means of low-storage Runge-Kutta 4 order scheme, designed by Jameson *et al.* (1981) found in (Canuto *et al.*, 1988, p. 287).

The aliasing problem

Aliasing problems occurs performing the multiplications required to computing the convective terms. To show how aliasing affect the products, let's consider two variables and their relationship with the physical values and the transformed one that is (for a simple demonstration, we take into account unidimensional data, those considerations are extendible in a three-dimensional data field) :

$$U_j = \sum_{k_u=-N/2}^{N/2-1} \hat{u}_{k_u} \exp(ik_u x_j) \tag{4.8}$$

$$V_j = \sum_{k_v=-N/2}^{N/2-1} \hat{v}_{k_v} \exp(ik_v x_j) \tag{4.9}$$

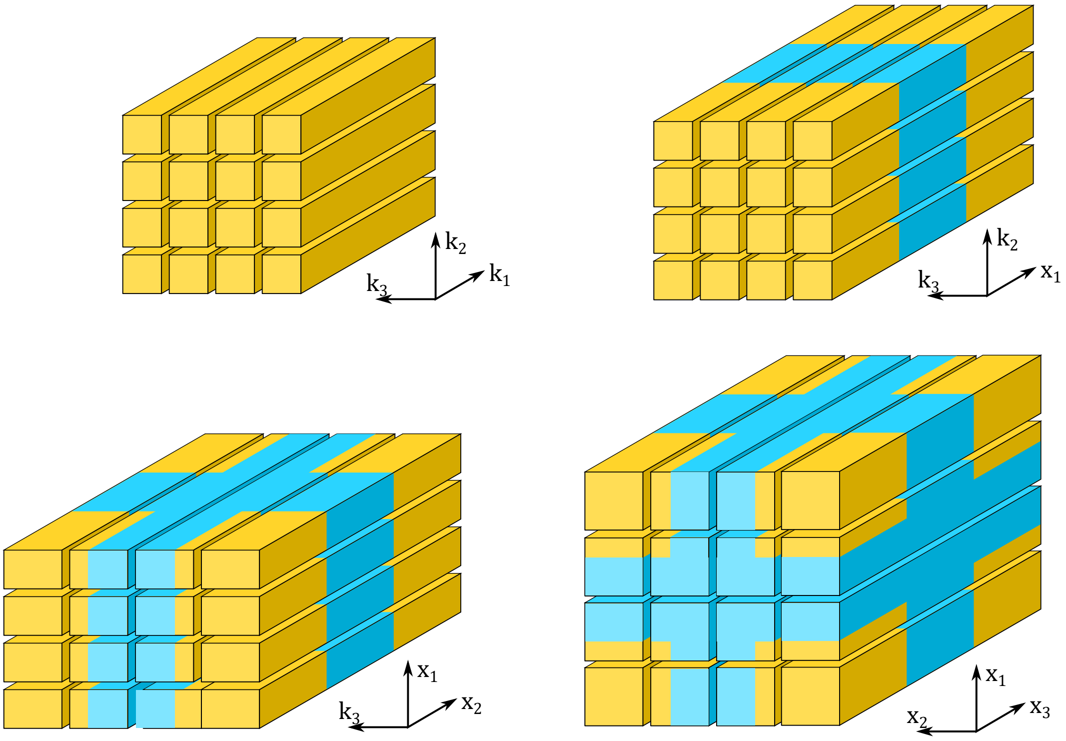

Figure 4.1. Inverse transform procedure with 16 process. The field in wave-number space (top left) is transformed into physical space (bottom right). During the process the domain is expanded by introducing dealiasing region (cyan), and transposition occurs in order to perform FFTs (see axis).

$$W_j = \sum_{k_w=-N/2}^{N/2-1} \hat{w}_{k_w} \exp(ik_w x_j). \tag{4.10}$$

If we want to compute the product $W_j = U_j \cdot V_j$, we have:

$$W_j = \sum_{k_u=-N/2}^{N/2-1} \hat{u}_{k_u} \exp(ik_u x_j) \cdot \sum_{k_v=-N/2}^{N/2-1} \hat{v}_{k_v} \exp(ik_v x_j) \tag{4.11}$$

that can be simplified joining the sum operators, and using the exponential properties

$$W_j = \sum_{k_u=-N/2}^{N/2-1} \sum_{k_v=-N/2}^{N/2-1} \hat{u}_{k_u} \cdot \hat{v}_{k_v} \exp[i(k_u + k_v)x_j) \tag{4.12}$$

Comparing this last equation with the (4.10), and we get that transform $\hat{w}_{k_w}$ is equal to the sum of the terms $\hat{u}_{k_u} \cdot \hat{v}_{k_v}$ for which $k_u + k_v = k_w$ (of course with k_w in correct range):

$$\hat{w}_{k_w} = \sum_{k_u+k_v=k_w} \hat{u}_{k_u} \cdot \hat{v}_{k_v} \qquad |k_w| \lesssim N/2 \tag{4.13}$$

Computing product in this way is not convenient, it is better compute the product in the physical space and then go back to the Fourier space(Orszag & Gottlieb, 1980). Acting like that, we can consider the anti-transformed of W_j

$$\hat{W}_{k_w} = \frac{1}{N} \sum_{N-1}^{j=0} W_j \exp(ik_w x_j) \tag{4.14}$$

Making some substitution, we get

$$\hat{W}_{k_w} = \sum_{k_u+k_v=k_w} \hat{u}_{k_u} \hat{v}_{k_v} + \sum_{k_u+k_v=k_w \pm N} \hat{u}_{k_u} \hat{v}_{k_v}$$

$$\hat{W}_{k_w} = \hat{w}_{k_w} + \sum_{k_u+k_v=k_w \pm N} \hat{u}_{k_u} \hat{v}_{k_v} \tag{4.15}$$

where the second term is so called aliasing error.

A way to eliminate aliasing, is the aliasing removal by padding (or 3/2 rule) (Canuto *et al.*, 1988, 84). The key of this de-aliasing technique is the use of discrete transforms $\tilde{u}$ with M rather than N points. Transform values are essentially the same

$$\tilde{u}_k = \begin{cases} \hat{u}_k & |k| \lesssim N/2 \\ 0 & \text{otherwise} \end{cases} \tag{4.16}$$

We get that the transformed product is

$$\tilde{W}_{k_w} = \sum_{k_u+k_v=k_w} \hat{u}_{k_u} \hat{v}_{k_v} + \sum_{k_u+k_v=k_w \pm M} \hat{u}_{k_u} \hat{v}_{k_v}. \tag{4.17}$$

Since we are interested in values for $|k_u + k_v| \lesssim N/2$, we have to guarantee that the second term will be always equal to zero for that wave-numbers. That can be done by choosing M large enough: the worst case condition(Canuto *et al.*, 1988) is when both k_u and k_v are equal to $-N/2$, so we have that

$$-\frac{N}{2} - \frac{N}{2} \leq \frac{N}{2} - 1 - M$$

and we get that

$$M \geq \frac{3N}{2} - 1. \tag{4.18}$$

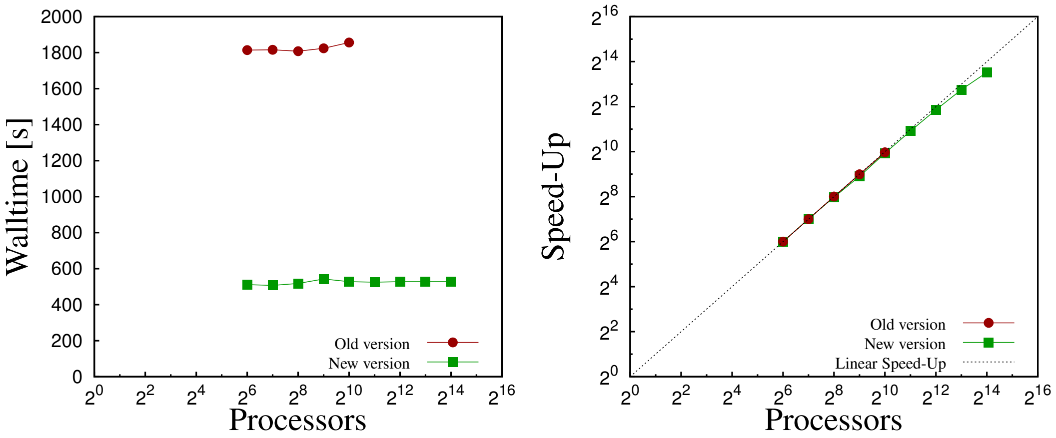

Figure 4.2. Left: walltime for a single RK4 cycle in a cubic domain with $M = 2048$. Walltime= $t \cdot n$, where t is the real time needed, and n is the number of process. Right: Speed-up of the code. Speed-Up= $n_R \frac{t_R}{t}$ where t_R and n_R are reference quantities (in this case $n_R = 64$).

Implementation and parallelization

The code is based on the TurIsMi v1.4 of the Philofluid group (www.polito.it/philofluid), released under the terms of the GNU General Public License. The new version has been implemented using Fortran 2008 standard: new features allows to design the code slightly object-oriented, increasing readability and efficiency on shared routines. Direct/inverse FFTs (Fast Fourier Transforms) are evaluated using the FFTW (Fast Fourier Transforms of the West) open-source libraries (which support the shared memory paradigm).

Parallelization is performed with an hybrid shared/distributed memory paradigm. In particular, we use a stencil parallelization (parallelization of two directions) in order to distribute the computational domain between a chosen number of process (up to $N^2/2$ – theoretical value). Distribution is performed using MPI 3.0 standard, which allows the usage of modern MPI libraries (such as OpenMPI and MPICH2).

In order to perform FFTs along a certain direction, a process needs to know the values associated to all the wave-numbers in such direction. For that purpose, matrix transpositions are mandatory in order to swap the distributed direction. During the inverse transform/transposition process (schematically represented in figure 4.1), the domain is "expanded" through the inclusion of the zero-padded antialiasing region (and viceversa is "contracted" during direct transforms). The usage of expanded domain only in physical space drammatically reduce the number of transform needed. We consider for simplicity a cubic domain, with N^3 in wavenumber space, and $M^3 = 27/8N^3$ points in physical space. Without the expansion/contraction process, the number of single FFTs required to perform a global transform is equal to $3M^2 = \frac{27}{4}N^2$. Without the expansion/contraction process, the number of single FFTs required to perform a global transform is equal to $N^2 + NM + M^2 = \frac{27}{4}N^2$, thereby saving 30% of computational time.

MPI 3.0 standard allows to implement global communication subroutine for direct/inverse domain transposition, and also for input/output routines. Global communication better exploit the potential of modern machines. In the rest of computational code. shared part of the parallelization is managed through OpenMP.

With the optimization process, the new version of the code (as shown in figure 4.2) is about 5 time faster, with a near-linear speed-up, allowing us to fully exploit the potential of the massively parallelized supercomputers.

Part II

Solar Wind and Heliosheseat Spectral analysis

Chapter 5

Solar wind analysis from Voyager probes data. Data reconstruction tecniques and application at 5 AU.

The heliosphere is characterized by the presence of a multi-scale, anisotropic fluctuations of plasma velocity and magnetic field. These fluctuations are turbulent, in the sense that they are disordered and span a broad range of scales in both space and time. The main responsible source of fluctuation is the Solar Wind which breezed all the solar system, interacting with the interstellar medium in the heliosheeth. The study of solar wind turbulence is motivated by a number of factors all keys to the understanding of the Solar Wind origin and thermodynamics.

A need that we must learn to meet to explore and surf the space is the reconstruction and interpretation of fluctuating signals coming from spacecrafts which for a number of different reasons are usually non regularly acquired on Earth or on other communicating spacecrafts (National Research Council, Decadal Strategy for Solar and Space Physics, 2013). The solar wind is characterized by a broad range of phenomena, in particular sharp changes in the flow and extreme conditions can often be met due to the crossing of the heliospheric current sheet, the presence of shocks and interaction regions between slow and fast wind streams and zones of strong density variations. Flow fluctuations are not just convected outward but show active energy cascades among the different scales. The solar wind turbulence phenomenology has been comprehensively reviewed by Tu & Marsch (1995) and Bruno & Carbone (2013).

Most studies of solar wind turbulence use data from near-Earth, with spacecrafts in the ecliptic near 1 AU (Tu & Marsch, 1995, see). Recent studies of the solar wind near 1 AU have found that fluctuations in the magnetic field can be fitted by power laws with an exponent of -5/3, while those of velocity often show an exponent of -3/2 (Podesta *et al.*, 2007). The Ulysses spacecraft provided the first observations of turbulence near the solar polar regions (see Horbury & Tsurutani, 2001); hourly-average Ulysses data show that the velocity power law exponent evolves toward -5/3 with increasing distance from the Sun, and that spectra at 1 AU are far from the asymptotic state (Roberts, 2010). In order to understand the evolution of the solar wind and its properties, it is necessary to analyze data at larger radial distances. Nowadays, only few spacecraft has reach the outer heliosphere, which are the probes Pioneer 10, Pioneer 11, Voyager 1 and Voyager 2. Pioneer mission ended before reaching the heliosheath (the craft no longer send data to earth), and Voyager 1 can provide only magnetic field data (due to an issue of the plasma-experiment). Voyager 2 can provide both plasma and magnetic field data of the heliosheath.

However, a major problem in the analysis of that data is related the presence of gaps inside the measured time-series, which typically increase with the distance and make any analysis challenging.

In this chapter the focus is on the on turbulence fluctuations in the solar wind plasma and magnetic field near the ecliptic plane, in particular in the outer solar system at about 5 astronomical units (AU) from the sun using Voyager 2 (V2) plasma and magnetic field data, and in the heliosheath, showing a preliminary spectral analysis in that region. V2 was launched in August 23, 1977 and reached a distance of 5 AU in the first half of 1979 (just before the Jupiter fly-by, V2 closest approach to Jupiter was on July 9). We use data from January 1 to June 29, 1979, day-of-year (DOY) $1 - 180$. That year V2 sampled plasma data with a resolution of 12 seconds. After that, telemetry constraints decreased data sampling first to every 96 seconds, and now every 192 seconds. An overview of the mission is reported in figure 5.1. The Voyager plasma experiment observes plasma currents in the energy/charge range $10 - 5950$ eV/q using four modulated-grid Faraday cup detectors (Bridge *et al.*, 1977). The observed currents are fit to convected isotropic proton Maxwellian distributions to derive the parameters (velocity, density, and temperature) used in this work. Magnetic field and plasma data are from the COHO web site (http://omniweb.gsfc.nasa.gov/coho/).

In 1979 data gaps are due mainly to tracking gaps; some smaller gaps are due to interference from other instruments. As a consequence, datasets from Voyager 2 are lacunous and irregularly distributed. In order to perform spectral analysis, methods for signal reconstruction of missing data should be

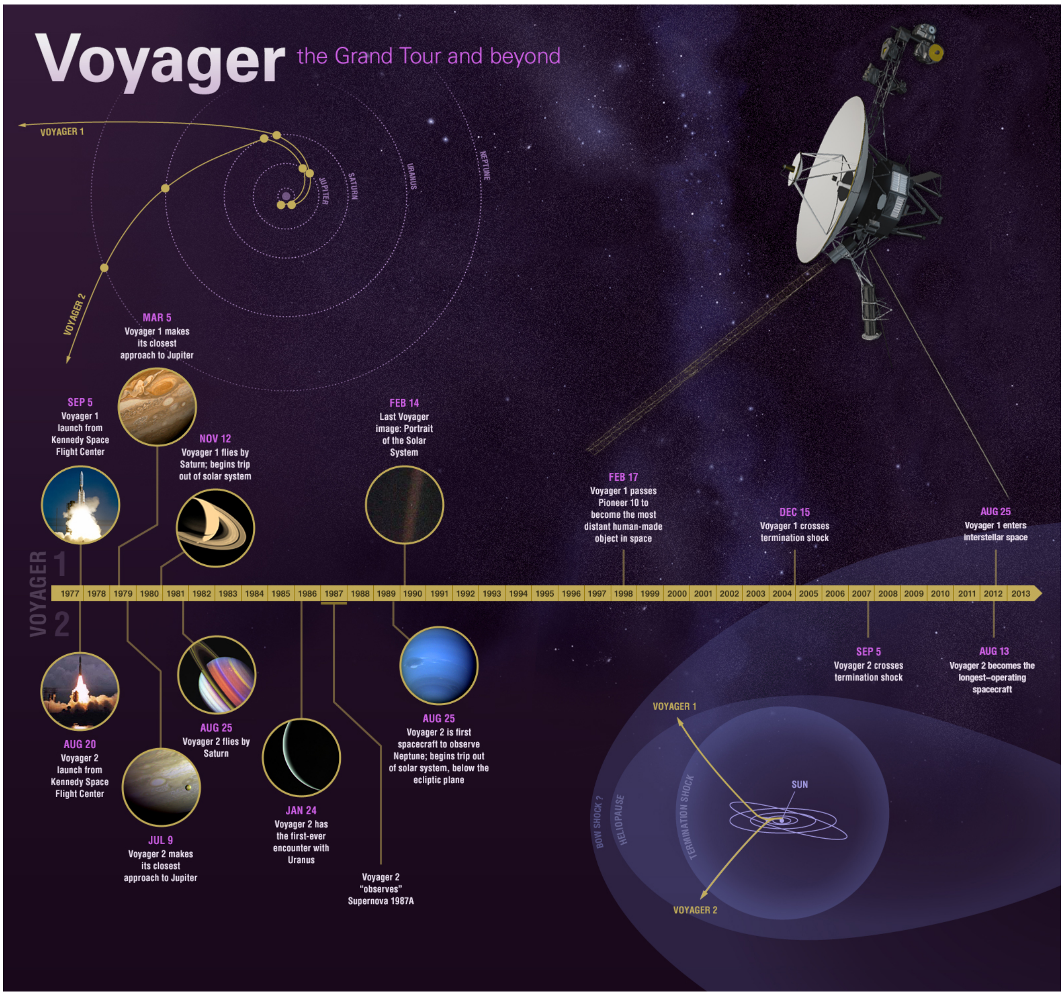

Figure 5.1. Voyager mission timeline, with indication of the path and main events that have occurred to date. Source: NASA Jet Propulsion Laboratory - Californian Institute of Technology.

implemented.

The results shown in this chapter have been presented in the 4th International TMB Workshop (Gallana *et al.*, 2014*c*, Trieste), in the 67th Annual Meeting of the APS-DFD (Tordella *et al.*, 2014, San Francisco), in the 15th ETC Conference (Gallana *et al.*, 2015*b*, Delft), in the Vortical Structures and Turbulence Conference (Fraternale *et al.*, 2015*b*, Rome), in the 14th Annual Internartional Astrophysics Conference (Fraternale *et al.*, 2015*a*, Tampa Bay), in the 68th Annual Meeting of the APS-DFD (Gallana *et al.*, 2015*a*, Boston), and in the AGU Fall Meeting (Richardson *et al.*, 2015, San Francisco), and published on the European Journal of Mechanics B/Fluids (Iovieno *et al.*, 2016), Physica Scripta (Fraternale *et al.*, 2016), and on the Journal of Geophisical Research (Gallana *et al.*, 2016*b*).

In the following section, we contextualize the physical condition of the data recorded by V2 in the solar wind, with particular focus on the average quantities and low order statistics of the solar wind physical variables. We then introduce five different signal reconstruction methods, which come from different scientific field, adapted to our aim. these methods have been verified by means of synthetic turbulent data, and by data coming from other probes (Ulysses). Those time series are spoiled by introducing the same sequence of gaps present in the Voyager 2 data. We finally applied the methods on V2 data, showing the plasma and magnetic field spectrum, with a discussion on the spectral index observed.

Parameter		Value	
$\boldsymbol{V_{SW}}$	Mean velocity	$4.54 \cdot 10^2$	km/s
$\boldsymbol{V_A}$	Alfvén velocity	$4.94 \cdot 10^1$	km/s
$\boldsymbol{E_v}$	Kinetic energy	$1.20 \cdot 10^3$	$\mathrm{km}^2/\mathrm{s}^2$
$\boldsymbol{E_m}$	Magnetic energy	$1.37 \cdot 10^3$	$\mathrm{km}^2/\mathrm{s}^2$
$\boldsymbol{E}$	Total energy	$2.57 \cdot 10^3$	$\mathrm{km}^2/\mathrm{s}^2$
$\boldsymbol{H_c}$	Cross helicity	15.8	$\mathrm{km}^2/\mathrm{s}^2$
$\boldsymbol{L_{E_v}}$	Kinetic correlation length	$3.68 \cdot 10^7$	km
$\boldsymbol{L_{E_m}}$	Magnetic correlation length	$3.75 \cdot 10^7$	km
$\boldsymbol{\lambda_v}$	Kinetic Taylor scale	$2.93 \cdot 10^7$	km
$\boldsymbol{\lambda_m}$	Magnetic Taylor scale	$2.11 \cdot 10^7$	km
$\boldsymbol{n_i}$	Numerical density	0.23	cm^{-3}
$\boldsymbol{E_T}$	Ions thermal energy	2.29	eV
$\boldsymbol{T}$	Ions temperature	$2.70 \cdot 10^4$	K
$\boldsymbol{\beta_p}$	Ions plasma beta	0.22	
$\boldsymbol{c_s}$	Ions sound speed	$1.93 \cdot 10^1$	km/s
$\boldsymbol{f_{ci}}$	Ions Larmor frequency	0.02	Hz
$\boldsymbol{f_{pi}}$	Ions plasma frequency	0.10	kHz
$\boldsymbol{f*}$	Convective Larmor frequency	0.44	Hz
$\boldsymbol{r_{ci}}$	Ions Larmor radius	$4.29 \cdot 10^3$	km
$\boldsymbol{r_i}$	Ion inertial radius	$1.58 \cdot 10^2$	km

Table 5.1. **Solar wind global parameters.** Reference parameters from the Voyager 2 recorded data. All the quantities are averages (or integral) over the whole period of 180 days. $V_A = B/sqrt\mu_0 m_i n_i$ and β_p is the ratio between thermodynamic and magnetic pressure.

5.1 1979 DAY 1-180 Voyager 2 data

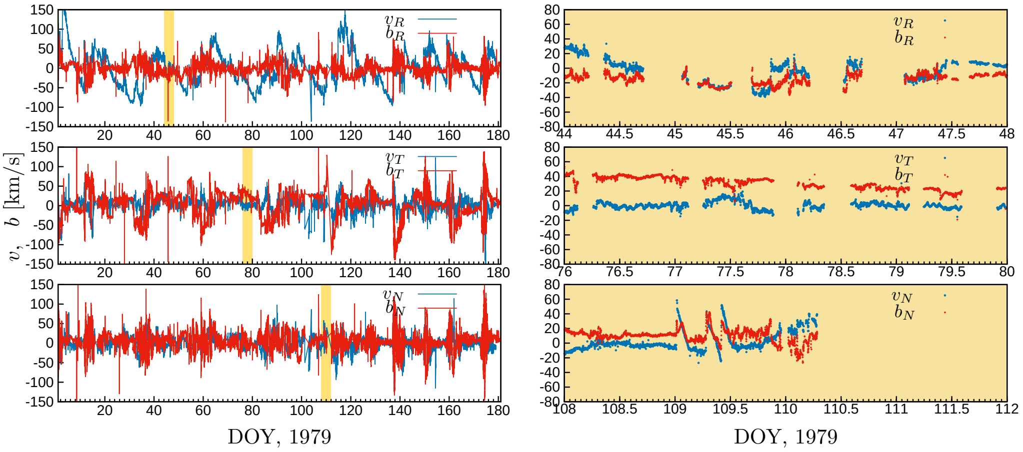

Figure 5.2. Voyager 2 1979 data. Plasma velocities (red lines) and magnetic fields (blue lines) recorded by Voyager 2 in the first 180 days of 1979, COHOWeb repository (http://omniweb.gsfc.nasa.gov/coho/. RTN Heliographic reference frame is used. The magnetic field is represented using Alfvén units. In each of the right panels a 4 days period is magnified to show the data gaps.

The dataset consists of vector plasma velocity and magnetic field data from 01/01/1979 00:00 GMT to 06/29/1979 19:00 GMT, a period of about 180 days, see figure 1 and tables 1-2. In 1979 the plasma speed and direction were sampled each 96 s, while for magnetic field the resolution of the data we use is 48 s (the actual sampling frequency is higher than 0.1 Hz).

As regards the magnetic field, the 48-s samples are averages from higher resolution measurements. The actual sampling time of the LMF Voyager magnetometer is 0.06s. From this data, 1.92s, 9.6s and 48s averages had been computed and published. As regards the plasma quantities (ion velocity, ion density, ion thermal speed), 96s is the sampling time in the period we consider. These data can be considered snapshots with a 96s cadence. In detail, the PLS instrument consists of four Faraday cups. A single measurement comes from an integration time, for each of the four detectors, which can be varied between 0.03 and 0.93 s. The time between measurements varies between 12s and 192s, in 1979 it was 96s. (Behannon *et al.*, 1977; Bridge *et al.*, 1977). It is well known that the variations in the solar wind speed reduce going outward from the Sun as fast and slow parcels push against one another. Beyond 1 AU these interaction regions form shocks and much of the solar wind at 5 AU has been shocked at least once. There is a lot of features in these time series besides turbulence (fast wind, slow wind, ejecta, shocks, sector reversals, the

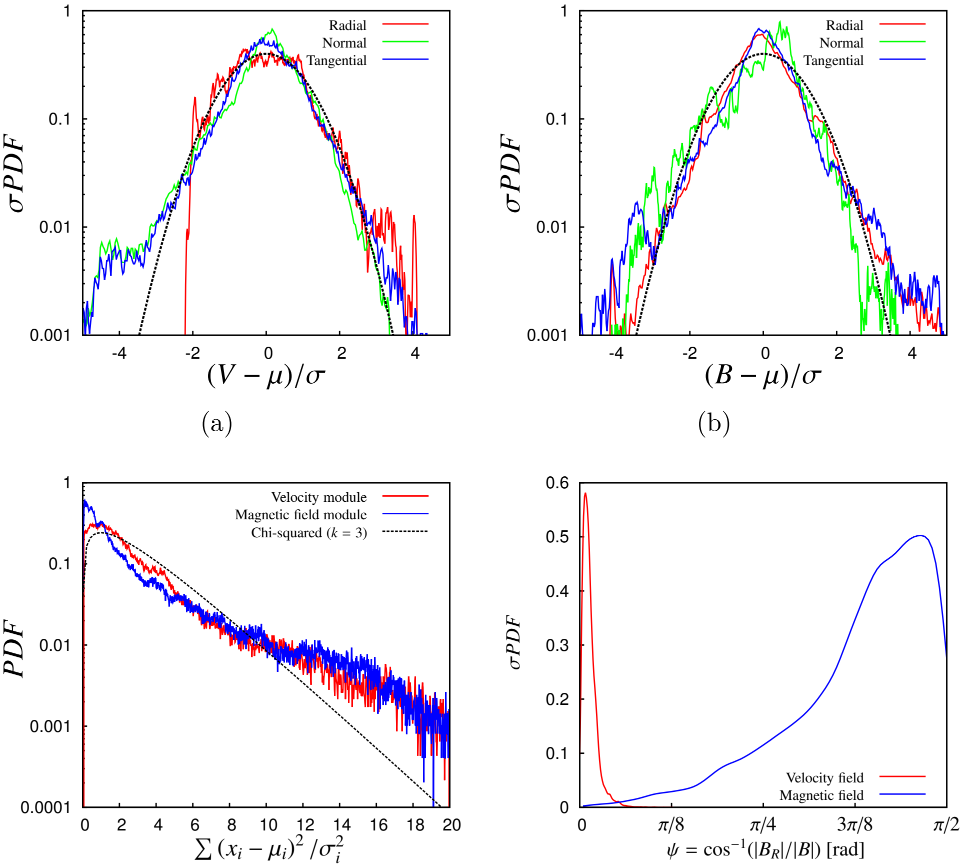

(a)

(b)

(c)

(d)

Figure 5.3. Probability density functions of the plasma velocity and magnetic field fluctuations. (a-c-b) Normalized probability density function of the plasma velocity(a) and magnetic field (b) components in the radial (red), tangential (green) and normal (blue) direction, and of their module (c), normalized as in equation 5.1. (d) Normalized probability density function of the angle ψ between the radial direction and the local velocity (red line) and magnetic (blue line) fields. The magnetic field is generally tilted 85 to 105 degrees with respect to the the radial direction.

heliospheric current sheet and its structures, etc.) and some of these features contribute Fourier power at all frequencies to the power spectral density.

A plot of the data is shown in figure 5.2, where the fluctuations of the components of plasma velocity and magnetic field in Alfvén units are represented using the RTN Heliographic reference system. The RTN system is centered at the spacecraft, the R (radial) axis is directed radially away from the Sun through the spacecraft. The T (tangential) axis is parallel to the solar equatorial plane and is positive in the direction of planetary rotation around the Sun. The N (normal) axis completes the right handed set. The right panels of the figure magnifies 4 days of data to show the typical data gap distribution.

	μ	σ^2	Sk	Ku
v_R	454	1893	0.43	3.41
v_T	3.21	252.9	-0.99	7.35
v_N	0.51	250.3	-0.36	5.80
B_R	-0.04	0.173	0.53	6.71
B_T	0.06	0.85	-0.72	10.2
B_N	0.10	0.34	-0.24	7.65
$\lvert\delta\mathbf{v}\rvert^2$	3.00	10.47	2.40	10.27
$\lvert\delta\mathbf{B}\rvert^2$	2.48	17.41	3.17	14.90

Table 5.2. Intermittency and anisotropy for the solar wind. Mean values and first three moments for the velocity and magnetic fields flucutation components and their modules; μ is the mean value, σ^2 the variance, Sk the skewness and Ku the kurtosis. Velocity are measured in km/s and the magnetic field in nT. The modules of the fluctuations are normalized on the variance, see equation 5.1, in order to be able to compare them with a chi-square distribution (standard 3-component chi-square distribution has mean 3, variance 6, skewness 1.63 and kurtosis 7).

The anisotropy of the fields can be determined by looking at the single components probability density functions (PDFs) in figure 5.3, panels (*a*-*c*). Particularly important are the differences of the radial components compared to the tangential and normal ones: a quantification of the anisotropy can be appreciated by comparing the skewness values in table 5.2. The presence of intermittency in the velocity and magnetic fields can be also observed by looking at the PDFs of the modules of the normalized vector fields, shown in figure 5.3 (*d*). The normalized vector fields are given by

$$|\delta\mathbf{x}|^2 = \sum_i^3 \frac{(x_i - \mu_i)^2}{\sigma_i^2} \tag{5.1}$$

where μ_i is the mean value and σ_i^2 the variance of the i-th component of the vector field $\mathbf{x}$. The same plot shows a three-component chi-square distribution as a reference. Intermittency occurs over a broad range of scales and seems to be slightly higher in the magnetic field data which has larger skewness and kurtosis (see table 5.2).

In order to analyze anisotropic effects from a spectral point of view, it is important to identify the wave-numbers parallel to the magnetic field $k_\parallel$ and normal to it $k_\perp$, as suggested first by Montgomery *et al.* (1987). We consider the angle ψ between the local vector field and the radial direction, defined as

$$\psi_v = \cos^{-1}\left(\frac{|v_r|}{|\mathbf{v}|}\right) \qquad \psi_m = \cos^{-1}\left(\frac{|B_r|}{|\mathbf{B}|}\right). \tag{5.2}$$

The PDFs of these angles are represented in panel (**a**) of figure 5.3: while the average plasma velocity is oriented along the radial direction (the mean angle is 0.04 ± 0.03 radiant), moving away from the sun, the magnetic field is characterized by angles close to $\pi/2$ which make it perpendicular to the radial direction as expected for a Parker spiral.

5.2 Spectral analysis of lacunous data: methods and validation with synthetic turbulence data

The data from the Voyagers suffer from increasing sparsity as the probes move outward in the solar system. There are many causes of data sparsity, noise and artificial unsteadiness in the signals, the most important of which are:

- tracking gaps due to the V2 location and due to limited deep space network availability
- interference from other instruments
- possible errors in the measurement chain (from the Faraday cups up to the data acquisition system and the signal shipping to Earth)
- the temporal sequence of the propulsion pulses (nuclear propulsion) used to control the Voyager trajectory and thrusters pulses on the spacecraft

In the period considered, the the nominal resolution of the dataset used δt_s was 96 s and 48 s for plasma and magnetic field data, respectively. For the Voyager magnetometer experiment, the 48 s data comes from averages of higher resolution data (1.92 s and 9.6 s – for a review about the Voyager MAG experiment, see Behannon *et al.* (1977)). The longest continuous (i.e. no missing data, $\delta t = \delta t_s$) data subset is ≈ 19.5 hrs. The distribution of the time interval between two consecutive available data points δt is shown in figure 5.4.

In this section we show the analysis procedure followed to perform a reliable spectral analysis and to quantify the uncertainty of the results obtained. Two sequences of synthetic turbulence (named *Synt1* and *Synt2*) have been generated from imposed three-dimensional power spectrum and random phases:

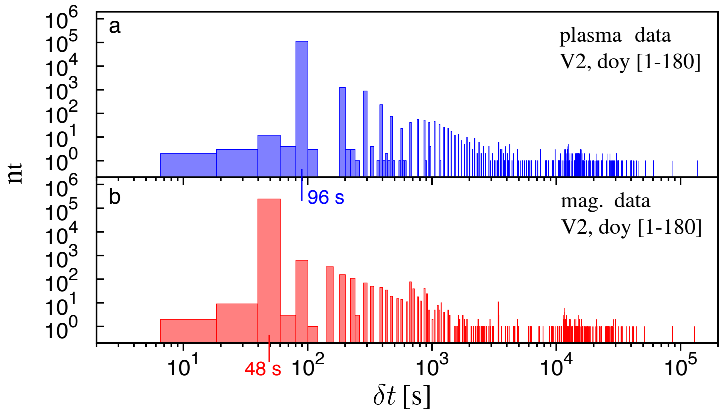

Figure 5.4. Distribution of the time interval between consecutive V2 data points (period 1979, DOY 1-180). n_t is the number of data points spaced by a time interval δt, and it is traced as a function of the interval length δt . (**a**) Plasma data (i.e. velocity, density, and thermal speed data). The sampling frequency is $\delta t_{sV} = 96$ s, so this value is the most frequent among the data. (**b**) Magnetic field data. The data resolution here is $\delta t_{sB} = 48$ s. Note that in both cases many time intervals $\delta t = \delta t_s + j \cdot \delta t_s$, with $j = 1{,}2, ...,$ characterize the data. Note also that $\delta t = \delta t_s + j \cdot \delta t_s$ represents a gap of $(j-1)$ missing data.

- *Synt 1*: contains an energy injection range and an inertial range $\rightarrow E_{3D}(n/n_0) = \frac{(n/n_0)^\beta}{1+(n/n_0)^{\alpha+\beta}}$
- *Synt 2*: contains an energy injection range, an inertial range and a dissipative range $\rightarrow E_{3D}(n/n_0) = \frac{(n/n_0)^\beta}{1+(n/n_0)^{\alpha+\beta}}\left[1 - exp(\frac{n-n_{tot}}{\gamma} + \epsilon)\right]$

where $\beta = 2$, $\alpha = 5/3$, $n_0 = 11$, $\gamma = 10^4$, $\epsilon = 10^{-1}$: the energy injection range follows a power law with exponent in the interval 2, the spectral maximum is placed at a frequency corresponding to one solar day, the inertial range extends over three and a half decades and has a power decay equal to $5 = 3$, and the dissipative range is placed around $5 \cdot 10^3$ Hz and has a maximum decay of -3. These sequences have been made sparse by giving them the same gap distribution as the 1979 Voyager 2 data. The true spectra of synt 1 and 2. The true spectra of these dataset are shown in figure 5.5, where the results from the techniques used are shown (spectral indices are always computed from a linear regression in the log-log space, using all the points of the smoothed spectra within the indicated frequency range.

We have considered five methods of spectral reconstruction. These methods come from multi-disciplinary areas, spanning from astrophysics (maximum likelihood), to classical numerical analysis, to telecommunication engineering and image processing (compressed sensing)

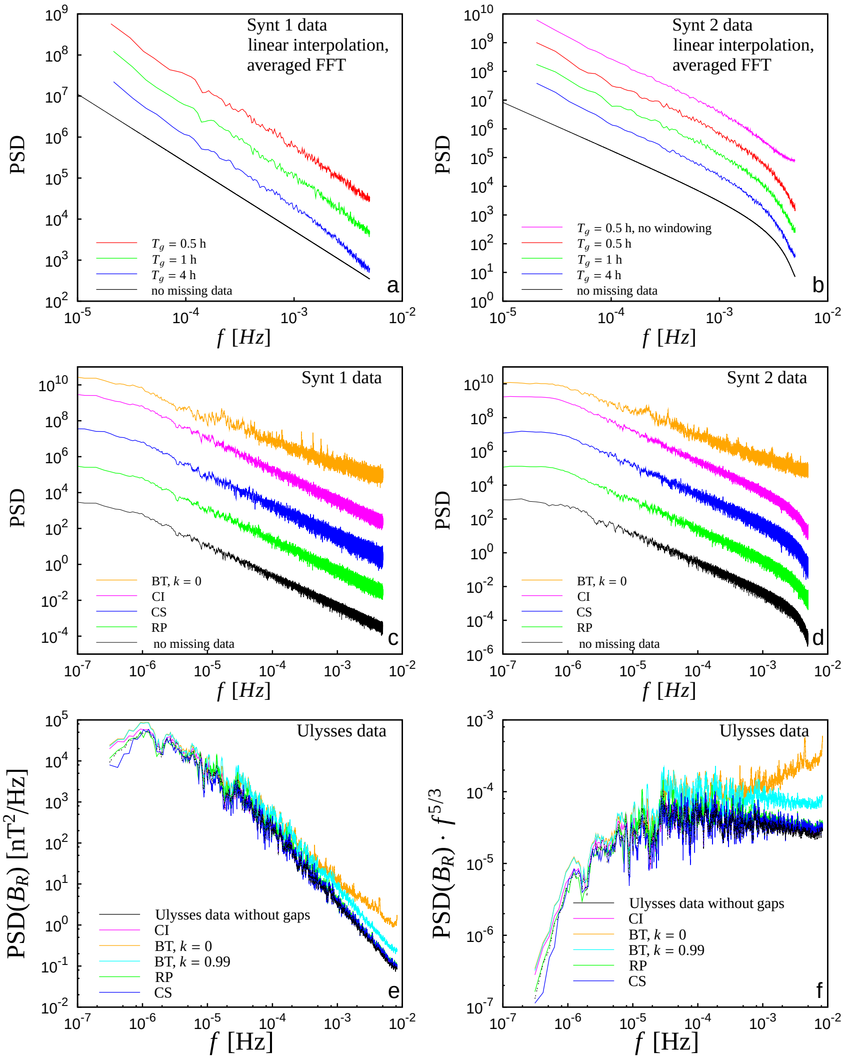

Figure 5.5. Validation on synthetic data and Ulysses measurement. (*a*, *b*) Spectra by direct FFT, with Hann windowing, on linearly interpola1ted subsets. Segments are selected so that the maximum gap length filled by the interpolation is T_g and their length is at least 12 h. Here the error lies between 0.4% ($T_g = 0.5$ h) and 2.4% ($T_g = 4$ h) in the range $f \in [10^{-5}; 10^{-3}]$. (*c*, *d*) Spectral computation in the entire period. The discrepancy of the power law exponent is below 2.5% for the last three methods (CI, RP, CS). A smoothing is applied by averaging neighboring frequencies to all curves. The energy is preserved for all spectra, but they have been shifted for clarity. (*e*, *f*) Spectrum of the radial component of magnetic field recorded by Ulysses in the period 1990, DOY 298 - 1991, DOY 45. The black lines represents the spectrum from Ulysses data. The different spectral recovery methods have been tested after having projected on the Ulysses data the same gap distribution of Voyager 2 data in 1979. Panel (*f*) shows the compensated spectrum.

Average spectra of windowed, linearly interpolated short data subsets

This first method is limited to short intervals and, therefore, does not allow a spectral reconstruction over many decades. Data are reconstructed on short subsets, taking as parameter the maximum gap allowed inside the subsets T_g. In this methodology we perform a linear interpolation to evaluate the missing data. The result is the average on the spectra computed on those interpolated subset. A windowing technique (Hann window) is necessary to eliminate noise effect ($\approx 1/f$) due to segmentation. To preserve the total energy a factor of 2.66 is applied to the squared Fourier coefficients. The low-pass behavior of the interpolator results in a steepening of the spectrum, especially in the high frequency range, and becomes much more evident as T_g increases. For *Synt1*, the relative error on the spectral index α lies between 1.9% ($T_g = 0.5$ hrs) and 5.4% ($T_g = 4$ hrs) in the range $f \in [10^{-5}, 10^{-3}]$ Hz, while in the last frequency decade it increases up to 8% for $T_g = 0.5$ hrs. For *Synt2*, the discrepancy lies between 0.4% ($T_g = 0.5$ hrs) and 2.4% ($T_g = 4$ hrs) in the range $f \in [10^{-5}, 10^{-3}]$ Hz. Notice, that a similar teatment was used by Bellamy *et al.* (2005) where the focus was on large ensemble of "short" spectra from observation periods of about 13 h with maximum missings of 10%.

Blackman-Tukey method

The second method we implement is the Blackman & Tukey (1958) method (BT, in the following), since it has been widely used in solar-wind analysis, see e.g. the works by Matthaeus & Goldstein (1982); Leamon *et al.* (1998); Smith *et al.* (2006*a*,*b*); Joyce *et al.* (2010); Borovsky & Denton (2010); Joyce *et al.* (2012). This method is based on the fact that the autocorrelation function and the power spectral density (PSD) are Fourier transform pairs. The strength of this procedure is that it overcomes, in principle, the problem of nonuniform time distribution. Indeed, the two-point correlation function is obtained by direct application of its definition:

$$C_{ij}^X = \langle X_i(t) X_j(t+\tau) \rangle \rightarrow C_{ij}^X = \frac{1}{N-r} \sum_{n=1}^{N-r} X_i(n) X_j(n+r) \tag{5.3}$$

where indexes i and j represents the components of the vector $\mathbf{X}$ and $\tau = r\Delta t$ in the discrete case. In the general case, on the data $\mathbf{X}$ a linear prewhitening is applied before evaluating the spectra:

$$X_i = X_i'(t) - k \cdot X_i'(t + \Delta t)$$

where $\mathbf{X}'$ is the original data, and k is a prewhitening parameter. In the case of missing data, the unknown values can just be ignored, and they don't contribute to the sum (5.3). The BT method evaluates the two-point correlation in this way:

$$C^X_{ij}(r) = \frac{1}{N(r)} \sum_{n=1}^{N(r)} X_i(n)X_j(n+r)p(n,r) \quad \text{with} \quad r = 1, ...N/2 \tag{5.4}$$

$$N(r) = \sum_{n=1}^{N} p(n,r) \tag{5.5}$$

$$p(n,r) = \begin{cases} 1 & \text{if } (n) \text{ and } (n+r) \text{ exist} \\ 0 & \text{if } (n) \text{ or } (n+r) \text{ does not exist} \end{cases} \tag{5.6}$$

Afterwards, the PSD is then computed by means of a FFT after an (optional) tapered cosine window. Finally, if the prewhitening has been applied, the spectra need a postdarkening process, multiplying the computed PSD with a transfer function:

$$Y(f) = Y'(f) \cdot [1 + f^2 - 2kcos(\omega\Delta t)]$$

Spectra computed in this way are shown in figure 5.5(c,d) , orange curves. For the gap amount and distribution of the data we consider, BT does not lead to an accurate spectral estimation. The reason for this resides in the slow convergence of the correlation function, that is highly affected by the sparsity of data when it is computed using (5.4). The correlations result oscillates, with the same periodicity as the counter $N(r)$. The resulting spectra show - for the high data sparsity here considered - non-physical peaks and biased values of the spectral decay slope, see the orange curves in figure 5.5. For *synt1*, the error in the slope is 15.4% for $f \in [10^{-5}, 5 \cdot 10^{-4}]$ Hz, and 38% for $f \in [5 \cdot 10^{-4}, 5 \cdot 10^{-3}]$ Hz. For *synt2*, which has a steeper spectrum in this last frequency range, the error goes up to 72%. We conclude therefore that the basic BT method is not suitable for solar-wind data with $> 25\%$ missings (at least if the number of points is about 10^5). It should be noted that in all the works cited above, the BT method is shown to work greatly for contiguous datasets or for datasets with at most 10% gaps. Typically, the prewhitening/postdarkening operation is associated to BT, in order to prevent spectral leakage due, e.g., to local trends (see Rosenblatt (1965); Keisler & Rhyne (1976)).

Correlation on linearly interpolated data

The third method we test is still based on the two-point correlation function. In this case correlations are computed on linearly interpolated data in the entire 180 days period. For gap distribution of V2 data, we see that the linear interpolation improves the convergence of the correlation function. The resulting power spectra are the pink curves in figure 5.5 (c, d). The linear interpolator has a low-pass effect, leading to a leakage of energy from the higher to the lower frequencies of the spectrum, but in this case this effect is very limited. This is also confirmed by the application of a prewhitening filter, which has no sensible effect on the result. The error in the spectral indices is below 3% for any frequency range.

Maximum likelihood reconstruction

The fourth procedure is a maximum likelihood data recovery method. This reconstruction is non-deterministic, but it is constrained by the true data where these are available. A complete description of the technique is given by Rybicki & Press (1992) and an application can be found in Press & Rybicki (1992). The recovery is based on an estimation of the two-point correlation function and it also allows to account for noise in data. We used the same correlations computed for the previous method. In this case the size of filled gaps T_g is a parameter to be chosen, and the goodness of the correlation function allows us to recover the full sequence. Notice indeed, that the largest gap is about 45 hrs, while the correlation function is quite accurate even for much larger time lags, which allows recovery of the 180 days period. Results are shown in figure 5.5(c,d), green curves. This procedure is computationally more expensive than the others, but it improves the spectral estimation in the high frequency range by reducing the low-pass effect of the linear interpolator of the previous method. Also in this case the discrepancy from the correct spectral slope is below 3 %.

Compressed-sensing

The last method we show performs a spectral recovery without data interpolation, and it is called *compressed sensing* (CS in the following, Donoho (2006); Candes *et al.* (2006*a*,*b*)). Results are shown in figure 5.5 (c, d), blue curves. CS is a recent theory that provides guarantees for the reconstruction of (exactly or approximately) sparse signals, namely signals with many null (or approximately null) components, from linear, compressed measurements. In mathematical terms, CS studies the underdetermined linear system $A\mathbf{y} = \mathbf{x}$, where A is matrix of size $m \times n$ with $m < n$, and $\mathbf{y}$ and $\mathbf{x}$ have consistent dimensions. The available data vector $\mathbf{x}$ is then a linear compression of the unknown $\mathbf{y}$, which is assumed to be sparse. CS theory provides conditions that make such problems well posed, that is, with a unique solution. In particular, much effort has been devoted to study which families of sensing matrices A guarantee the possibility of recovery. Among these, partial Fourier matrices (say, discrete Fourier transform matrices with missing rows) have been recently studied (see, e.g., Rudelson & Vershynin (2006); Duarte & Eldar (2011); Xu & Xu (2015)), motivated in particular by the applications in medical imaging problems such as MRI (Lustig *et al.*, 2008). In the mentioned works, theoretical guarantees on partial Fourier matrices for CS are provided, in terms of the number of necessary measurements and positioning of the missing rows. In this work we formulated the problem as a Basis Pursuit and obtained the numerical solution through the SPGL1 solver for sparse problems (see van den Berg & Friedlander (2007) for theoretical and practical details). SPGL1 is suitable for the Fourier framework, as it deals with complex variables. Moreover, it allows us to cope with data of large dimension, since the sensing matrix A can be defined as function instead of explicitly storing the whole matrix. The relative error in the spectral slope for these methods is below 2.5%, in the range $f \in [10^{-6}, 5 \cdot 10^{-3}]$ Hz of *Synt1*, and $f \in [10^{-6}, 10^{-3}]$ Hz of *Synt2*.

Genetic Optimization

This optimization works in couple with the previous method, and it is useful to obtain a mean behavior of a spectral field. It works generating a stochastic set of model spectra, then an optimization process let this set to converge on the solution, comparing the datafield associated to the model spectrum with the original data (Koza, 1992). The comparison is achieved by projecting the gaps of original data on the computed ones, and then minimizing the discrepancy between the spectra obtained from these two dataset, through the usage of an arbitrarily chosen technique among the previous. In particular, we have use this kind of optimization in couple with the Correlation method on interpolated data. Even if this technique is pointless for data at 5 AU, when the number of gaps increase it becomes an excellent tool to have an idea of the mean behavior of the power spectra.

5.3 Power law spectra at 5 AU.

The spectra obtained for each component of magnetic field and plasma velocity and for their relevant energy are represented in figure 5.6. All the recovery methods converge at similar spectral indices and can be considered equivalent. In what follows we have chosen to present here the results given by the correlation method with linear interpolation.

It should be noted that, by applying the Taylor frozen-flow hypothesis, the

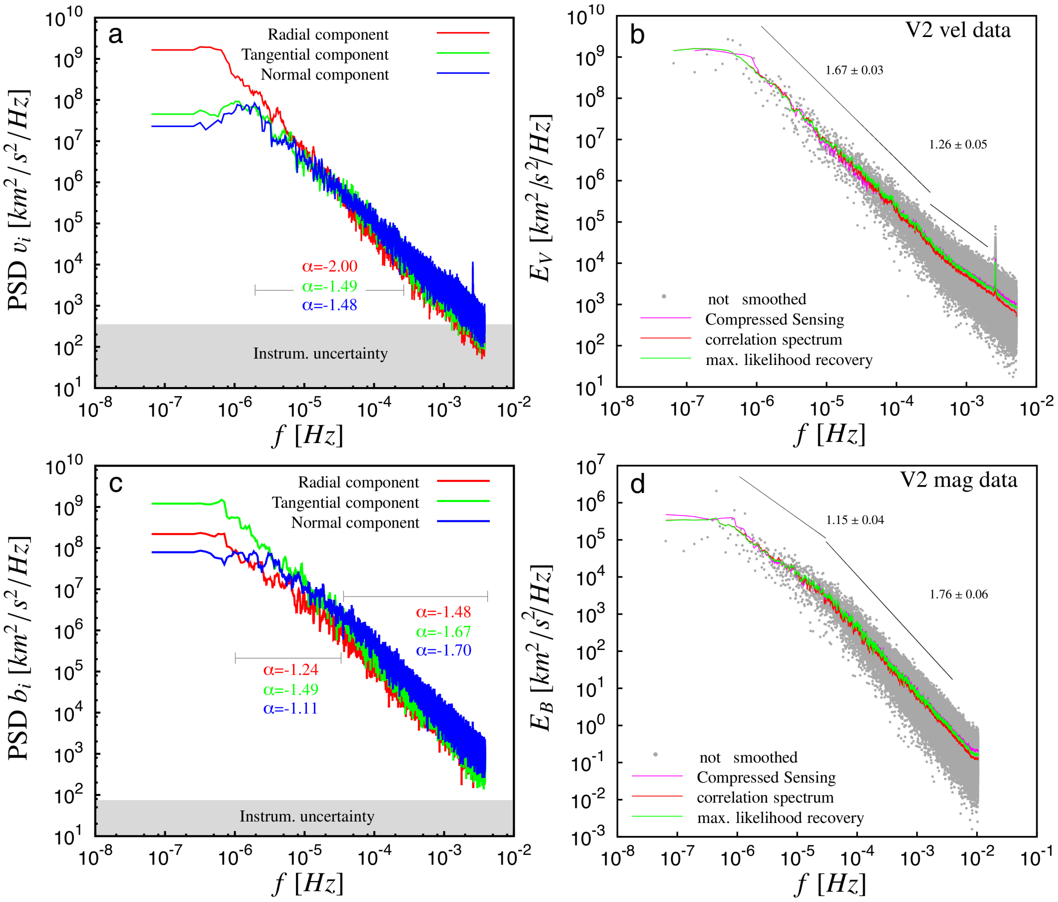

Figure 5.6. Voyager 2 spectra, 1979, DOY 1–180.(**a**): Spectra of the velocity plasma components computed by the correlations method with linear interpolation. (**b**): Spectrum of the plasma kinetic energy. Three methods of analysis (compressed sensing, correlation spectrum with linear interpolation and Rubycki & Press maximum likelihood recovery) are compared. (*c* - **d**): Same as (a) and (b) for the magnetic field. The grey bands in panels (a) and (c) indicate the instrumental uncertainty. The grey curve in panels (b) and (d) represents the unsmoothed spectrum by means of interpolated correlations. The spectral exponents are reported in table 5.3.

frequency can be converted to radial wave-numbers: the wavenumber space is he preferred space where the turbulence cascade among different physical scales is pictured. Considering an inertial regime, the energy E and the wavenumber k satisfy the law $E(k) \propto k^{\alpha}$. The values of α depend on the way the energy is transferred among the inertial scales. The turbulent energy transfer rate is defined (Zhou *et al.*, 2004) as $\varepsilon = u_k^2/\tau_{sp}$, where $u_k(k) = (kE(k))^{1/2}$ is the velocity associated to a given eddy, $\tau_{sp}(k) = \tau_{nl}^2(k)/\tau_t(k)$ is the spectral

f range	v_R	v_T	v_N	E_v
$10^{-6} \div 4 \cdot 10^{-4}$	-2.00	-1.49	-1.48	-1.67
$4 \cdot 10^{-4} \div 5 \cdot 10^{-3}$	-1.18	-1.26	-1.48	-1.33

f range	B_R	B_T	B_N	E_B
$10^{-6} \div 3 \cdot 10^{-5}$	-1.06	-1.46	-0.85	-1.21
$3 \cdot 10^{-5} \div 5 \cdot 10^{-3}$	-1.56	-1.72	-1.77	-1.72

f range	b_R	b_T	b_N	E_b
$10^{-6} \div 3 \cdot 10^{-5}$	-1.24	-1.49	-1.11	-1.34
$3 \cdot 10^{-5} \div 5 \cdot 10^{-3}$	-1.48	-1.67	-1.70	-1.65

Table 5.3. Solar Wind spectral exponents from Voyager 2 data at 5 AU. The maximum error on spectral indexes is about 0.07; b is the magnetic field in Alfvén units. For the velocity field, exponents in the higher frequency range are computed neglecting the peak present at $f = 2.6\ mHz$.

transfer time, $\tau_{nl}(k) = (ku_k)^{-1}$ is the characteristic eddy turnover time, and τ_t the time scale of the triple correlation function. Time τ_t may depend on any relevant turbulent parameter and the wavenumber k, depending on the dominant phenomenology.

We consider two classical phenomenological interpretation for plasma physics:

- The strain-dominated MHD turbulence, characterized by the direct interaction among vortices having similar wavenumbers. Adopting the Kolmogorov's concept of independence of widely separated wavenumbers in the inertial range, the MHD motion is comparable to a classical hydrodynamics motion in which the energy power law has been determined by dimensional analysis Kolmogorov (1941); Marsch & Tu (1989). In this case the time scale of the transfer function is equivalent to the eddy turnover time, and so the relation between E and k is given by $E(k) \sim \varepsilon^{2/3} k^{-5/3}$.

- The sweep-dominated MHD, characterized by the direct interaction of vortices which can have very different wave-number. In particular, a big vortex sweeps oppositely the small ones, depending on their polarity. In that case, correlations decay with an effective lifetime determined by propagation of structures at the Alfvén time scale, $\tau_A(k) = (V_A k)^{-1}$, see Iroshnikov (1963) and Kraichnan (1965), which yields the -3/2 slope.

Looking at the power spectra of each component of the velocity field, shown in panel **a** of figure 5.6 and resumed in table 5.3, the behavior of the system at low frequencies ($f < 4 \cdot 10^{-4}$) shows that the exponent is steeper for the radial component rather than the other two. In particular, the spectral index in the radial direction is $\alpha_{v_R} \approx -2.00$. At high frequencies, the situation is reversed and the spectral index of the radial component is $\alpha_{v_R} \approx -1.18$, smaller than the other two ($\alpha_{v_T} \approx -1.28$, $\alpha_{v_N} \approx -1.48$). Considering the power spectrum of the kinetic energy, the exponent found is $\alpha_{E_k} \approx -1.67$ in the low frequency domain. At high frequencies, the situation is reversed and the spectral index of the radial component is $\alpha_{v_R} \approx -1.18$, smaller than the other two ($\alpha_{v_T} \approx -1.28$, $\alpha_{v_N} \approx -1.48$). Considering the power spectrum of the kinetic energy, the exponent found is $\alpha_{E_k} \approx -1.67$ in the low frequency domain. Such a value is consistent with the Kolmogorov hydrodynamic theory for isotropic turbulence. In the high frequency range, for $f \in [3 \cdot 10^{-4}, 2 \cdot 10^{-3}]$ the fit gives the value of $\alpha_{E_k} \approx -1.33$.

The magnetic field components (fig.7 c) present a very different phenomenology with respect to the plasma velocity: for each component the spectra have higher exponents in the high frequency range ($f > 3 \cdot 10^{-5}$) and they tend to become flatter at low frequencies, as shown in figure 5.6 (*c*-*d*) and in tables 5.3. Moreover, an anisotropic behavior is also observed both at high and low frequencies: in particular, the radial component is always lower than the tangential one. The normal component, instead, has a spectral index analogous to the radial one a low frequencies (for $f < 3 \cdot 10^{-5}$, considering Alfvén units, $\alpha_{b_R} \approx -1.24$ and $\alpha_{b_N} \approx -1.11$, when $\alpha_{b_T} \approx -1.49$), while it becomes similar to the tangential exponent at high frequencies (for $f > 3 \cdot 10^{-5}$, considering Alfvén units, $\alpha_{b_T} \approx -1.67$ and $\alpha_{b_N} \approx -1.70$, when $\alpha_{b_T} \approx -1.48$). The spectral exponent for the magnetic energy is $\alpha_{E_m} \approx -1.65$ at high frequencies, as predicted by the Kolmogorov law (fig.7 d). At low frequencies the exponents drop to values around $\alpha_{E_m} \approx 1.34$.

Spectra trend is visible in figure 5.7, where spectra have been smoothed using a gaussian kernel smoother, defined as

$$\overline{X}(\kappa) = \frac{\sum_{\kappa^*} K(\kappa,\kappa^*) X(\kappa^*)}{\sum_{\kappa^*} K(\kappa,\kappa^*)} \qquad K(\kappa,\kappa^*) = \exp\left(\frac{\kappa-\kappa^*}{2b(\kappa)}\right) \qquad b(\kappa) \propto \kappa \quad (5.7)$$

where X is the original spectra and $\overline{X}$ the smoothed one. Note that the peak in kinetic spectra visible at the frequency $f = 2.6\ mHz$ is associated to the data acquisition frequency – indeed, it is a harmonic of the sampling frequency $f_s = 10.4$ mHz. It is not an artifact of the signal reconstruction methods, since such a peak does not show up in the test cases of figure 5.5. Moreover it is most evident in the tangential and normal velocity components, while it is not present in the magnetic field.

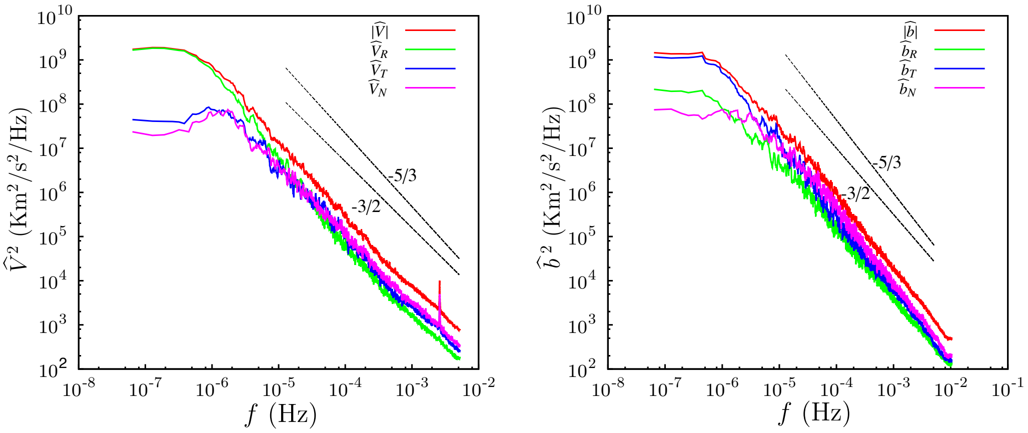

Figure 5.7. Plasma velocity and magnetic fields components and module power spectra. In this plot a variable gaussian smoothing is used, allowing to qualitatively compare the mean trend of the different components.

Spectra presented here are in good agreement with those found by Matthaeus & Goldstein (1982) (magnetic spectral index of -1.7 at high frequencies for Voyager 1 data at about 5 AU) and Klein *et al.* (1992) (magnetic spectral index of -1.17 at low frequencies and -1.88 at high frequencies for Voyager 1 data at 4 AU), where an analysis for V1 spectra of magnetic modules respectively at 5 and 10 AU can be found for frequencies ranges from 10^{-7} Hz to 10^{-4} Hz.

However, caution must be taken before adopting the Kolmogorov interpretation because, especially at large scales, since a given spectral power low can represent different phenomenology of solar wind, such as fast wind/slow wind interaction, ejecta, shocks, sector reversals, heliospheric current sheet, etc. In order to distinguish effects due to the turbulent fluctuations from some of the other phenomenologies, a method to remove jumps due to shock or harmonic behavior as been implemented (Burlaga *et al.*, 1989; Roberts & Goldstein, 1987). The condition for which a point is considered a jump point is that:

$$|\langle X\rangle_{-1h} - \langle X\rangle_{+1h}| > H \cdot \min(\langle X^2\rangle_{-1h}, \langle X^2\rangle_{+1h})$$

where $\langle X\rangle(t)$ and $\langle X^2\rangle(t)$ represent the local mean and standard deviation computed on a 5 hours periods, respectively. The subscripts indicates that these quantities are evaluated 1 hour before or after the jump point, and H is a multiplier, for which Roberts & Goldstein (1987) suggest a value of 20 so that jumps cover about the 8% of the data. In the present case we chose $H = 10$ in order to reach a jump fraction equal to 7%. The jump points are then linearly interpolated, obtaining a "jump series". The difference between the complete data-set and the jump series provides the "fluctuation series". Results are shown in panel (a) of figure 5.8.

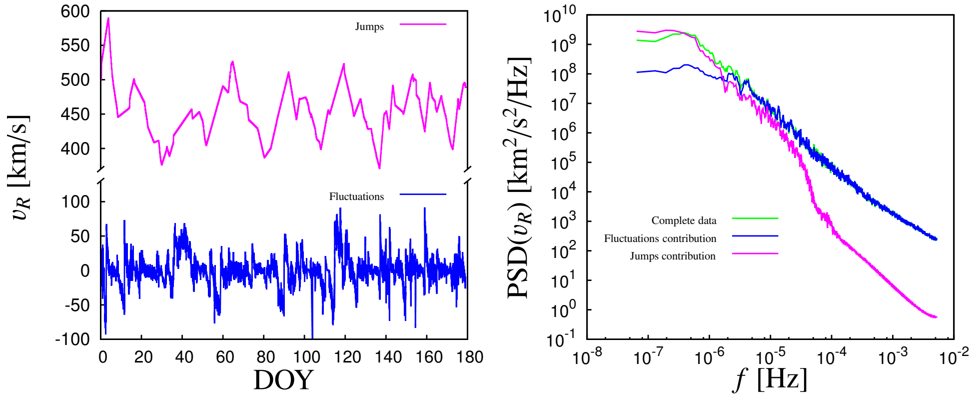

Figure 5.8. Panel (a) Jump (pink) and fluctuation (blue) series of V2 radial velocity, as identified by the Roberts & Goldstein criterion. Panel (b) Power spectra of total radial velocity (green), contribution of fluctuations (blue), and contribution of jumps (pink).

As shown in panel (b) of figure 5.8, the contribution to the global spectrum is mainly due to the fluctuations for frequencies greater than $4 \cdot 10^{-6}$ Hz (which corresponds to a period of 3 days, so about 0.75 AU), and it is still present a subdivision between two different spectral index (around -2 at medium frequencies, and -1.2 at high frequencies – separation frequency is $4 \cdot 10^{-4}$ Hz). For frequencies lower than $4 \cdot 10^{-6}$ Hz, the contribution to the global spectrum is mainly due to discontinuities and other local trends.

5.4 Magnetic and Cross helicities

Since the seminal paper by Moffatt (1969), the concept of helicity has been used as a tool to describe the structure of a fluid or plasma flow. From a mathematical point of view, the helicity density associated with two vector fields $\mathbf{X}$ and $\mathbf{Y}$ is defined as the scalar product between the two vector, $\mathbf{X} \cdot \mathbf{Y}$; the integral of such quantity in the whole domain gives the total helicity. Helicity is a pseudoscalar quantity, that is, it changes sign switching from a right-handed to a left-handed frame of reference.

In plasma physics, magnetic and cross helicity represent important quantities in the analysis, since represent two of the so called “rugged” invariants, together with the total energy density of the field $e = u^2 + b^2$, where $b = b/(\mu_0 \rho)$ is the magnetic field in Alfv'enic units. In a similar way, the kinetic helicity is a material invariant of the flow in an inviscid (neutral) fluid, which is a direct consequence of Kelvin's theorem. Magnetic and cross helicity densities are defined, respectively, as

$$h_m = \mathbf{A} \cdot \mathbf{B}. \tag{5.8}$$

$$h_c = \mathbf{u} \cdot \mathbf{B}. \tag{5.9}$$

where $A = \nabla \times B$ is the potential field.

From a geometric point of view, the cross-helicity gives a measure of the degree of linkage of the vortex and magnetic flux tubes within the flow. In fact, considering the simplest archetypical sketch of figure 5.9, where the two fields are concentrated in two thin untwisted closed tubes which are intertangled, the helicity is equal to $2n\Gamma_1\Gamma_2$, where n is the number of linking or winding of the two tubes, and Γ_1 and Γ_2 are the flows across the two tubes. Although, in general, a generic field cannot be simply decomposed into a finite number of simple non-overlapping flux tubes, this simple sketch helps to understand the helicity significance. Therefore, a normalized helicity gives the measure of the knottedness of the first field tube(s) with the second field tube(s).

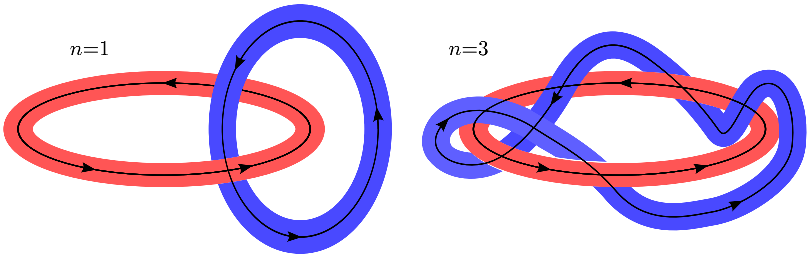

Figure 5.9. Sketch of a configuration of linked vortex/magnetic tubes with different number of windings n, that produce a non-zero helicity. Kinetic helicity: red and blue tubes are vorticity tubes. Magnetic helicity: red and blue tubes are magnetic tubes. Cross-Helicity: the red tube is a vortex tube and the blue tube is a magnetic tube (or the opposite).

For what concerns the physical meaning, both quantities H_m and H_c, as well their densities, are zero in a mirror-symmetric system and non-zero values can appear only when this symmetry is broken in the flow.Because the value of these inviscid (ideal flow) invariants cannot be modified by nonlinear terms, they constrain the overall dynamics and, therefore, their value and spectral distribution can give valuable information on the dynamics of turbulence in the solar wind.

The magnetic helicity plays a central role in the dynamo effect, the so-called α-dynamo. In fact, the presence of a magnetic field without reflectional symmetry, that is, with a non-zero magnetic helicity, generates fluctuations of the magnetic field, which, to first order approximation, are proportional to the helicity (Moffatt & Tsinober (1992); Moffatt (1978); Yokoi (2013)). Compared to the magnetic energy, which appears to be transferred to the small scale fluctuations, magnetic helicity presents an inverse cascade, that is, it cascades toward the larger scales of the flow (see Alexakis *et al.* (2007)). As a consequence, magnetic helicity is depleted much more slowly than energy in a freely evolving flow, while in a forced flow small-scale helical forcing can produce large-scale magnetic fields.

The turbulent cross-helicity is directly related to the coupling coefficients for the mean vorticity in the electromotive force and for the mean magnetic-field strain in the Reynolds stress tensor Yokoi (2013). This relationship suggests that the cross-helicity is important where inhomogeneities in the flow and in the magnetic field appear. Since such large-scale structures are ubiquitous in astrophysical phenomena, cross-helicity is expected to play a role in such flows. In the presence of cross-helicity, the mean vortical structures contribute to the electromotive force: the generation of magnetic field due to this effect is called the cross-helicity dynamo (or β-effect). In fact, in presence of a large scale vortical motion, the turbulent cross-helicity contributes to the electromotive force aligned with the large-scale vorticity. Provided that the velocity and magnetic field fluctuations are correlated, a contribution to the electromotive force parallel (when $h_c > 0$) or antiparallel (when $h_c < 0$) to the mean vorticity arises Yokoi & Balarac (2011). Moreover, more recently direct numerical simulations of magnetohydrodynamic turbulence have shown that, in association with high values of the cross-helicity, a blocking effect on the spectral transfer of energy is observed and results in energy accumulation in the system. This is concomitant with an increase of the exponent of the spectrum with the cross-helicity level. The spectral exponent increases toward the limiting value of 2 (Mizeva *et al.*, 2009).

The magnetic and cross-helicity spectra have been computed from single point measurement by the Voyager 2 spacecraft using data interpolation to reconstruct the missing values shown in section 5.2. While the cross-helicity can be directly computed from raw data (both plasma velocity and magnetic field are available), the evaluation of the magnetic helicity is more difficult, since the potential field $\mathbf{A}$ is not directly measured. For that purpose, we applied the formulae first proposed by Matthaeus *et al.* (1982); Matthaeus & Goldstein (1982) to deduce the magnetic helicity and cross-helicity spectra from the Fourier transforms of the velocity-magnetic field correlations. For the magnetic helicity of the fluctuations

$$\hat{h}_m(\kappa) = \frac{2}{\kappa}\mathrm{Im}\left(S_{TN}(\kappa)\right), \tag{5.10}$$

where S_{TN} is the Fourier transform of the correlation between the tangential and normal components of the magnetic field ($S_{TN}(\kappa) = \frac{1}{2\pi}\int C_{TN}(r)\mathrm{e}^{i\kappa r}\mathrm{d}r$, with $C_{TN}(r) = \langle b'_T(x) b'_N(x+r)\rangle$), while the cross-helicity of the fluctuations is computed as the Fourier transform of the correlation $u'_R b'_R + u'_T b'_T + u'_N b'_N$ between the velocity and magnetic fields. Only the assumption of homogeneity is necessary but no assumption of isotropy is made in obtaining the one-dimensional energy and helicity spectra.

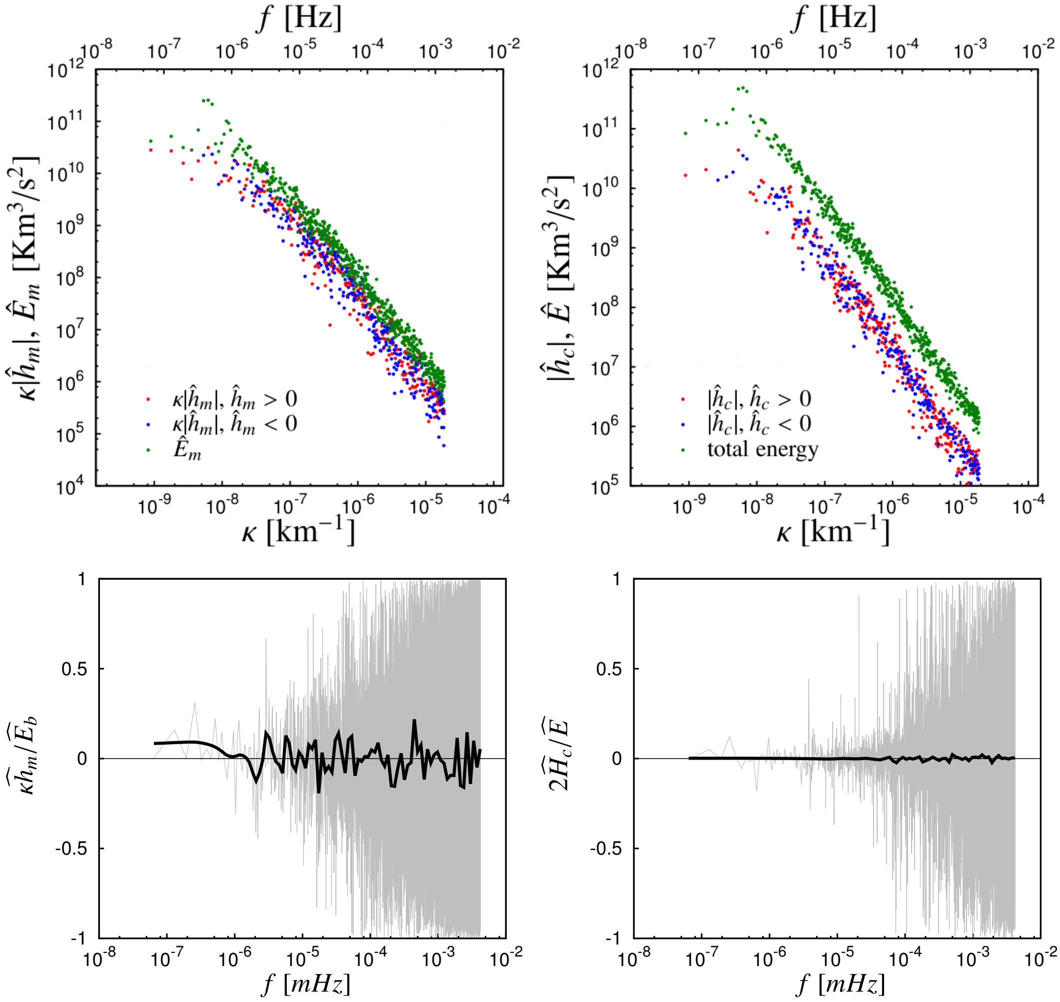

Figure 5.10. (Panels a-b) Power spectra of the magnetic helicity density and of the magnetic energy $\left\langle b'_j b'_j \right\rangle/2$ in Alfvén units (a) and of the cross helicity density and of the total energy $\left\langle b'_j b'_j \right\rangle/2 + \left\langle u'_j u'_j \right\rangle/2(b)$. For graphic clarity for frequencies above 10^{-6} Hz, not all the points of the spectra. (Panels c-d) Normalized magnetic helicity $\sigma_m = \kappa\hat{h}_m/E_m$ (c) and normalized cross-helicity $\sigma_c = \hat{h}_c/E$ (c). The thick line indicates the cumulative relative helicity.

A closer look at the scale dependence of the cross-helicity can be obtained by looking at its one-dimensional power spectrum. The cross-helicity spectrum can take both positive and negative values. The sign of the cross-helicity spectrum often indicates the propagation of Alfvénic waves outwards from the sun (positive helicity) (Matthaeus *et al.*, 1982; Matthaeus & Goldstein, 1982), as also contemplated by Belcher & Davis (1971), but periods with mixed helicity sign can appear. In our data, see figure 5.10, there is no preferred sign in any part of the cross-helicity spectra, whose modulus shows a fair power law scaling with an exponent equal to -1.59, close to the spectral exponent of the total energy spectrum, -1.62 during 1979. The number of frequencies with positive and negative values is comparable at all scales, and they balance: the integral cross-helicity can be estimated as 15.8 $\mathrm{km}^2/\mathrm{s}^2$, much lower than the total energy of 2640 $\mathrm{km}^2/\mathrm{s}^2$. The normalized cross-correlation is less than 1% at all frequencies, and therefore the two fluctuating fields are very mildly correlated.

Similar to the spectrum of the cross-helicity is the spectrum of the magnetic helicity, which has also a power law range with exponent -2.66, see panels (a) 5.10, shows almost an equipartition positive and negative values throughout the inertial range of the spectrum. The exponents of the magnetic energy spectrum in the same range of frequencies are -1.63 and -1.80, respectively (notice that in the ordinate the quantity $\kappa\hat{h}_m$ is represented). This result implies that the relative magnetic helicity of each scale, given by the ratio $\kappa\hat{h}_m(\kappa)/\hat{E}_m(\kappa)$, slowly decreases as $\kappa^{-0.03}$ in the observed frequency range. The sign of the normalized magnetic helicity $\kappa\hat{h}_m/E_m$ is positive at largest scales, and tends to change sign frequently at smaller scales. If we consider all the wave numbers, this value is relatively small, and equal to 0.135 (mainly due to the very first point). It is known that magnetic helicity can change sign and have opposite signs at the largest and smallest scales in magnetohydrodynamic system, an effect of the inverse cascade and its conservation. As a general comment, the weak values of the normalized magnetic helicity can be considered a signature of the negligible injection of helicity in the solar wind at the equatorial plane because the presence of the inverse cascade of helicity makes the helicity dissipation much lower than the dissipation of energy, thus the magnetic helicity remain almost constant throughout the system.

	P1 (SH)	P2 (UH)	P3 (SH)	P4 (UH)	**Total**
V_{SW} [km/s]	153.2	159.2	164.0	143.7	**152.3**
V_A [km/s]	65.7	52.3	60.25	58.9	**60.2**
E_v [km^2/s^2]	1511.8	1365.4	2210.1	1626.0	**1943.8**
E_m [km^2/s^2]	2498.7	1527.4	2226.0	1376.4	**1894.7**
E [km^2/s^2]	4010.5	2892.8	4436.1	3002.4	**3838.5**
n_i [dm^{-3}]	2.16	1.71	1.17	1.14	**1.38**
T [K]	$15.4{\cdot}10^4$	$16.7{\cdot}10^4$	$9.6{\cdot}10^4$	$5.5{\cdot}10^4$	$\mathbf{9.8{\cdot}10^4}$
β_p	2.43	3.59	1.36	0.69	**1.48**
c_s [km/s]	1021.4	1119.2	997.7	803.6	**928.5**
f_{ci} [Hz]	0.0018	0.0014	0.0013	0.0013	**0.0014**
f_{pi} [Hz]	9.05	8.53	7.08	6.98	**7.62**
$f*$ [Hz]	0.037	0.029	0.041	0.046	**0.040**
r_{ci} [km]	4142	5517	4037	3138	**3778**
r_i [km]	5542	5812	6975	7043	**6576**

Table 5.4. Reference parameters from the Voyager 2 recorded data. All the quantities are averages (or integral) over the indicated periods. Symbols are the same as in table 5.4

5.5 Power spectra law in the heliosheath: preliminary results

V2 has crossed the termination shock entering in the heliosheath in August 2007 (Richardson *et al.*, 2008). In this region, many are the observations not yet completely understood, as pointed out by Richardson & Decker (2014); Opher (2015). One of these is the difference in the flux of energetic ions (from about 40 KeV suprathermal ions to Galactic Cosmic Rays, >1 GeV) and electrons (from about 50 keV to >100 MeV) observed by V2 and its twin probe, Voyager 1 (V1) (Hill *et al.*, 2014). In particular, while the particle profiles at V1 were almost constant in the period 2007-2012, at V2 large variations up to a factor of 100 were recorded. According to Hill *et al.* (2014), possible physical interpretations to explain the enhancement or depression of energetic particle intensity are related to the Helioshperic Current Sheet (HCS) maximum latitudinal extensions. These northern and southern boundaries enclose the so called sectored heliosheath region (SHS), where the magnetic field changes polarity as the HCS is crossed, according to the Parker spiral structure (Parker, 1958). At higher North/South latitudes, outside the sector region, the heliosheath is unipolar (UHS). Traveling at a latitude of about 30° South, V2 is thought to have crossed different times the boundary of the SHS, and a correlation

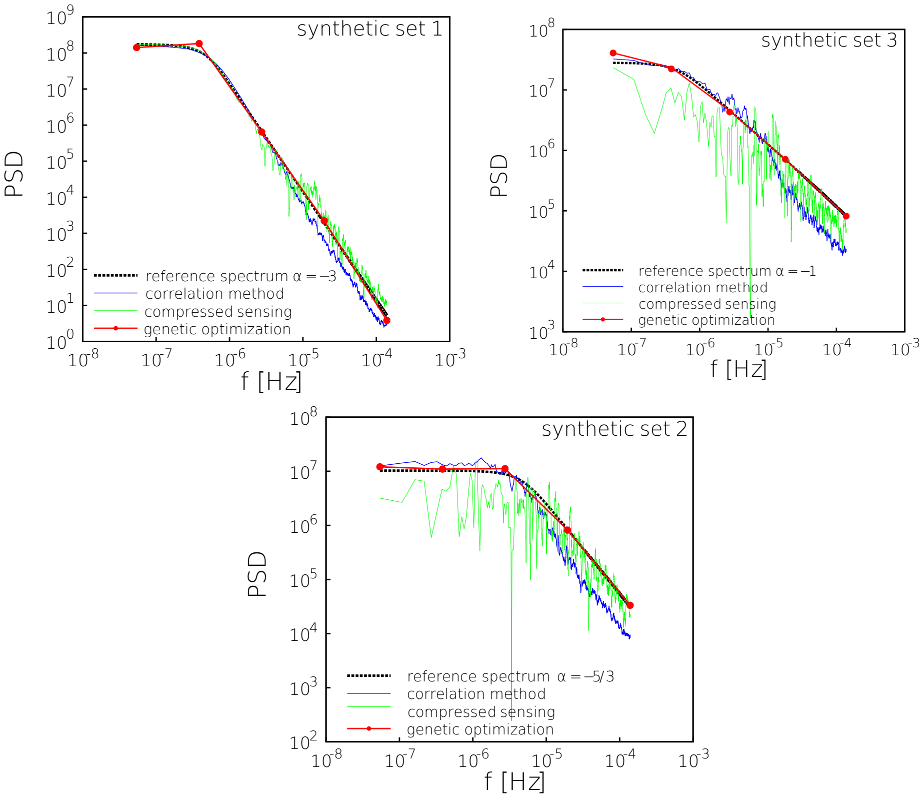

Figure 5.11. Comparison of three reconstruction methods (correlation, compressed sensing and genetic optimization) on synthetic dataset. The synthetic dataset have been made spare by giving them the distribution as the 2009 V2 data.

was found between the energetic particles flux at V2 and the alternating of unipolar, high-latitude, and sectored, low-latitude, heliosheath zones. Different particle transport properties are expected in these regions. Opher *et al.* (2011) suggested that in the sectored region the magnetic field was not laminar but chaotic, with the sector structure being replaced by a sea of nested magnetic islands. Spectral analysis can be a helpful instrument to characterize the velocity/magnetic field (turbulent?) fluctuations in different heliosheath regions (sectored/unipolar). In particular, in this very preliminary analysis, it has been taken into account the hourly averaged data of the V2 data in the period that ranges between September 2007 (about 83 AU from the sun) and June 2010 (about 92 AU from the sun). According to the works of Hill *et al.* (2014); Opher (2015), in this time-range we have found 2 periods of SHS, and 2 of USH:

- **P1** *SHS* September 2007 – January 2008

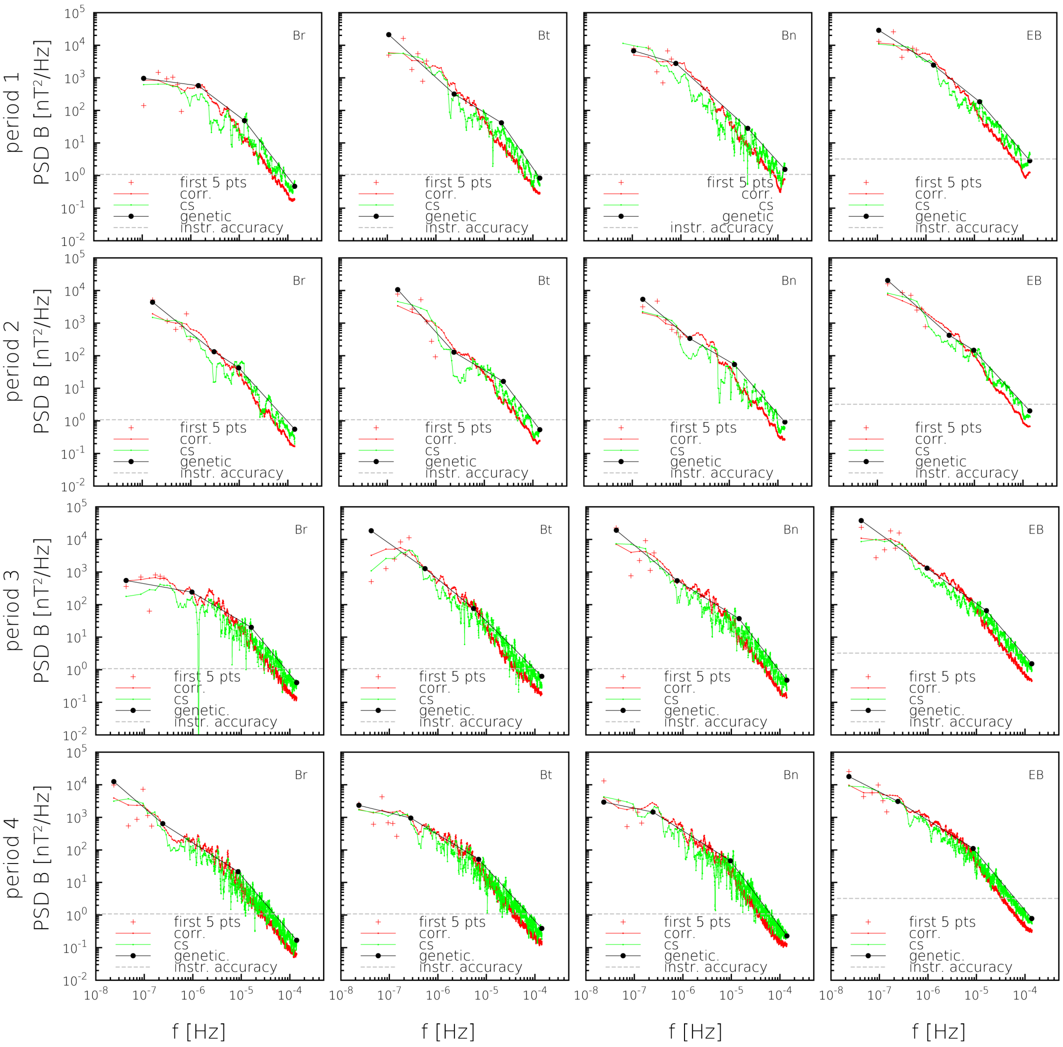

Figure 5.12. Magnetic field power spectra in the heliosheath for the four selected periods. The first three columns shows the behaviour of the magnetic field components (respectively B_r, B_t and B_n), while in the last column the magnetic energy is represented. Spectra are computed on hourly averaged dataset. The horizontal dashed lines represent the instrumental accuracy.

- **P2** *UHS* January 2008 – March 2008
- **P3** *SHS* March 2008 – February 2009
- **P4** *UHS* February 2009 – June 2010

In the considered period the data gaps problem is worsened, since about 70% of data are lost (tracking issues, noise, instrumental interferences and

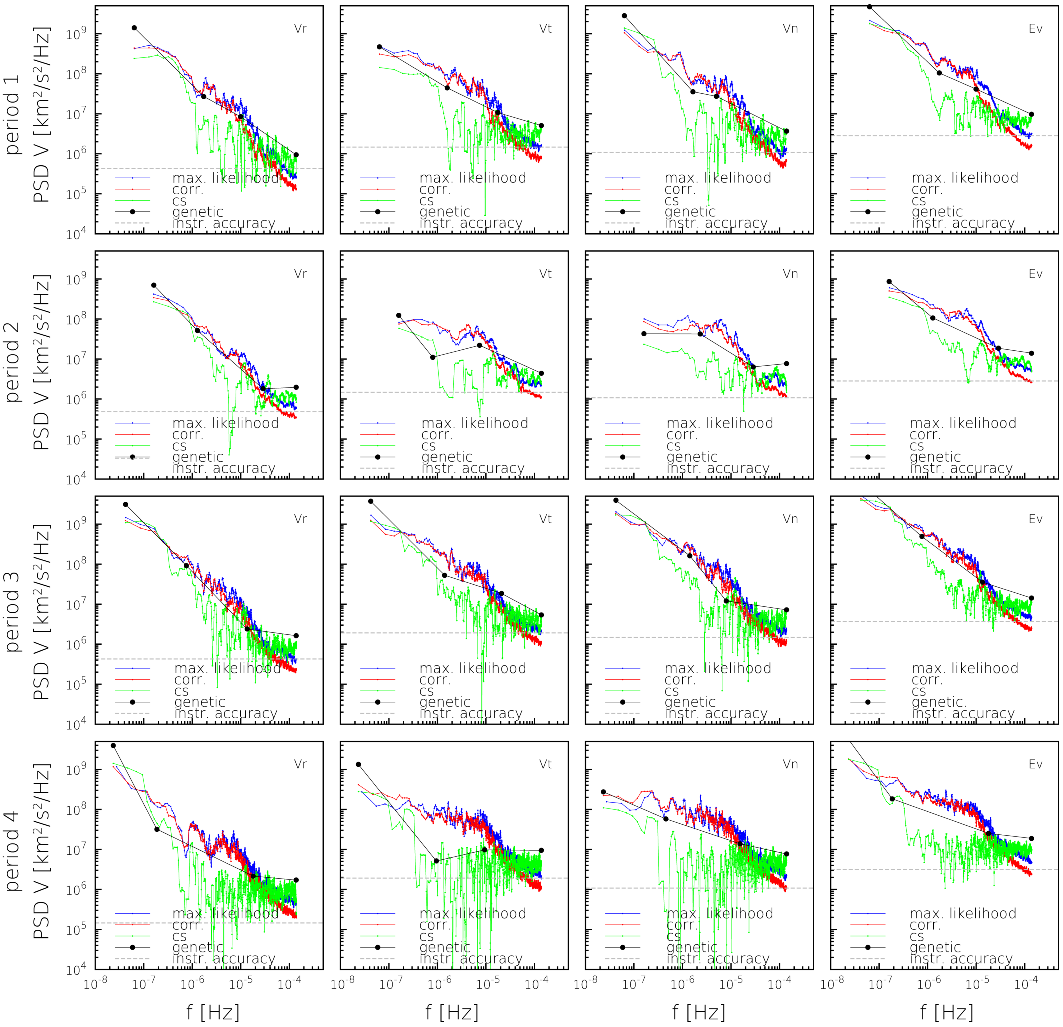

Figure 5.13. Velocity field power spectra in the heliosheath for the four selected periods. The first three columns shows the behaviour of the magnetic field components (respectively u_r, u_t and u_n), while in the last column the magnetic energy is represented. Spectra are computed on hourly averaged dataset. The horizontal dashed lines represent the mean instrumental accuracy.

other reasons). Figure 5.11 shows the test of the methods on synthetic data with different spectral index. All the methods achieve the correct mean spectral index, but the great sparsity generates different issues: correlation methods tends to underestimate the power spectra at high frequencies, compressed sensing is very noisy and genetic interpolation could just give information about the mean trend.

The results of the methodology are shown in figure 5.13 for the plasma velocity field, and in figure 5.12 for the magnetic field. A major problem in the velocity field analysis is the big uncertainty of the data, due to a poor instrumental accuracy, which is equal to 0.5% of the instantaneous velocity module, and it is not constant in time (see http://omniweb.gsfc.nasa.gov). Because of that, velocity spectral behavior cannot be sufficiently accurate to reach a statistical characterization of the different periods, since only in the low frequency range of radial velocity the methods converge to the same solution.

For what concerns the magnetic field, the instrumental accuracy is ±0.03 nT, giving the possibility to evaluate the spectral index. These spectral index are reported in table 5.5. In particular, it has been found that the spectral exponents are isotropic and near to -1 for frequency lower than 10^{-5} Hz (estimation obtained from the Correlation method), and becomes anisotropic at higher frequency, with values which ranges from -1.6 to -1.9 (estimation obtained from genetic optimization and compress sensing). The behavior seems not to be influenced by HSH/USH region, at least in the scale range considered. Further investigation are required, using the high-resolution data or improving the quality of the plasma velocity data.

	$f < 10^{-5}$				$f > 10^{-5}$			
period	B_R	B_T	B_N	$\|B\|$	B_R	B_T	B_N	$\|B\|$
P1	-0.91	-1.40	-1.36	-1.30	-1.83	-1.91	-1.66	-1.74
P2	-1.38	-1.33	-1.30	-1.33	-1.63	-1.92	-1.69	-1.70
P3	-1.00	-1.19	-1.11	-1.13	-1.62	-1.60	-1.83	-1.74
P4	-1.20	-1.16	-1.09	-1.13	-1.73	-1.63	-1.85	-1.77

Table 5.5. Spectral indices of the various magnetic components and module in the heliosheeth. Indices has been computed via linear regression in the log-log plane. At low frequencies ($< 10^{-5}$) results achieved with compress sensing method has been used, while at high frequencies the estimation is based both on the Genetic Optimization and the Compress Sensing.

5.6 Conclusions

In this chapter we have analyzed and tested methods with the aim of evaluate the spectral behavior of gapped time-series. The methods have been tested with the aim of compute solar wind spectra in different regions of the heliosphere. Procedures have been validated by testing five different data recovery methods (windowed averaged Fourier transforms of short data subsets, linearly interpolated over short gaps, Blackman-Tukey method, linear interpolation plus two-points correlations, and maximum likelihood recovery and compressed sensing) both on synthetic data which mimic the behavior of the well-known homogeneous and isotropic turbulence system and on a continuous time series of solar-wind measurements from 1 AU, to which data gaps have been added. In particular, the two test bases have been made lacunous by projecting the same gap distribution as in the 1979 first semester V2 plasma data Taking advantage of such methods, it has been possible to compute the power spectra of the solar slow wind and magnetic field at 5 AU at low latitude from Voyager 2 measurements, determining spectra for a frequency range extending over five decades ($10^{-7} - 10^{-2}$ Hz). This extended range, much wider than in any other previous study at this distance, allows to observe the changes in the spectral slopes providing informations on the structure of the solar wind.

The plasma velocity spectrum presents an intermediate frequency range with a power law decay exponent of about - 2 for the radial component and of about -1.5 for the tangential and normal components up to $f = 3 \cdot 10^{-4}$ Hz, while some flattening occurs at higher frequencies. The magnetic spectrum shows a change of spectral index at about $f = 5 \cdot 10^{-5}$ Hz, in agreement with Ulysses data near the ecliptic at 4.8 AU. Above this frequency the slope is -1.76 ± 0.06 and remains constant in the whole range of observed frequencies. We can therefore conclude that the inertial range extends at least from $f = 5 \cdot 10^{-5}$ to $f = 5 \cdot 10^{-3}$ Hz. The variation of the spectral index can be due to the presence of anisotropies with relevant effects of the parallel sweeping due to the large scale magnetic fluctuations. In fact, the anisotropy appears to be significant at frequencies below $f = 10^{-5}$ Hz, when most of the energy tends to be concentrated into the radial component of the velocity fluctuations and in the tangential component of the magnetic field fluctuations.

Alfvénic fluctuations do not appear to play a significant role, indeed the normalized cross helicity is globally below 1%, because positive and negative values, corresponding to outward and inward propagating fluctuations, respectively, are equally distributed along the frequency range. The magnetic helicity shows a small positive polarization of the magnetic field, due to the contribution of the slowest fluctuations.

In the last part it has been shown some preliminary results on data inside the heliosheath, where the solar wind interacts with the interstellar medium, and the system is characterized by the alternation of region with constant and varying polarity. The spectral analysis could be helpful to understand differences between such regions, but while it has been possible to reach a first estimation of the spectral indices of the magnetic field, no significant differences has been found. Further analysis on high-resolution data are required in order to point out differences in the spectral behavior.

Chapter 6

General conclusion

To conclude, in this thesis we have analyzed two different flows, which belong to different physical contexts, but characterized by the presence of multi-scale inhomogeneous fluctuations, to which is associated a strong anisotropy, and by the presence of effects related to stratification / mixing.

In the first part we have performed a set numerical experiments, considered a shear-less mixing layer obtained through the coupling of two homogeneous isotropic turbulent fields as initial condition, observing its evolution during the natural decay. The simulation has been performed with our home-produced computational code, which allows us to take advantage of the modern massively parallelized machines.

We have mainly focused on two aspects of the mixing: the behavior of a passive scalar transported through the interface, and the influence of a thermal stratification.

For the passive scalar, it has been observed that the mixing thickness (both of the scalar and self-diffusion of the velocity) follow the same temporal evolution: in particular the growth is faster in two dimensions. A relevant result obtained concerns the presence of two intermittent fronts in the scalar field. These fronts are located at the edges of the mixing region, moving away from the initial position of the interface as the mixing thickness increase, with a deeper penetration in the high energy region. Such intermittency is not limited to the large scales, but involves also the small scales. As shown by the simulation of a simple wavy perturbations of the interface, we have found that this behavior is not specific to the turbulent transport, instead it is a general dynamic characteristic of the chosen scalar field initial condition. The inertial range energy scaling is close to k^{-3} (for 2D cases) and $k^{-5/3}$ (for 3D cases), while the passive scalar tends to $k^{-1.7}$ (for 2D cases) and $k^{-5/3}$ (for 3D cases). Nevertheless, at the end of the transient evolution (10 time scales) in all cases we found an exponent value which is closer to the three dimensional $k^{-5/3}$

forward cascade than to the two dimensional k^{-1} Batchelor's scaling.

The influence of a thermal stratification inside the mixing layer has been investigated, taking into account both stable and unstable configurations. We have analyzed the dynamics of the velocity field and of unsaturated water vapor transport (represented as a passive scalar). Different levels of stratification have been considered, and it was found that a sufficiently intense stratification (so with a Froude square number of the order of 1) deeply changes the mixing dynamics. As a general consideration, we have observed that a stable stratification damp all the mixing effects, while an unstable condition tends to enhance the process. This is due to the formation of a sublayer inside the mixing region, characterized of a level of kinetic energy lower/higher than in the external regions, which can be interpreted respectively as pit (for stable)/peak (for unstable) of kinetic energy. In these sublayers a great deviation from large-scale isotropy is observed. We have observed that the entrainment (which in neutral condition decrease following an exponential law) vanish very quickly when the Froude square number reaches values of the order of 1. A qualitatively similar behavior has been observed also for other physical quantities (such as fluxes, small-scale anisotropy, etc.). From a spectral point of view, it has been found that the stratification acts directly on the large-scales of the vertical velocity, but the influence can be found in the dissipative range of all the physical variables – both in any of the velocity components and passive scalars.

In the second part we have carried out an analysis on the Voyager 2 data in order to characterize, from a statistical and spectral point of view, the solar wind. The biggest problem faced regards the data sparsity of the measured time-series. Various techniques for spectral analysis have been implemented and tested both on synthetic turbulence dataset and on solar wind data at 1 astronomical unit. Exploiting such methods, the solar wind at 5 astronomical units has been first analyzed, determining spectra for a frequency range extending over five decades ($10^{-7} - 10^{-2}$ Hz). Thanks to such extended range, we observed the changes in the spectral slopes both in the plasma velocity than in magnetic field. We have found an anisotropic behavior in the large scales of velocity field, with a greater spectral index in the radial component. A more isotropic behavior has been observed at higher frequencies ($f = 3 \cdot 10^{-4}$ Hz), with lower spectral index. Also the magnetic spectrum shows a change of spectral index at about $f = 5 \cdot 10^{-5}$ Hz, in agreement with Ulysses data near the ecliptic at 4.8 AU. We have therefore concluded that the inertial range extends at least from $f = 5 \cdot 10^{-5}$ to $f = 5 \cdot 10^{-3}$ Hz. These variations are probably related to the anisotropy of the physical system, since alfvénic fluctuations do not appear to play a significant role, indeed the normalized cross helicity is globally below 1%, because positive and negative values are equally distributed along the frequency range. We have then started the analysis of heliosheath data (around 90 astronomical units, where the solar wind interacts with the interstellar medium, and the system is characterized by the alternation of region with constant and varying polarity). In this region the data sparsity is very poor (only about 30% of data available), but it was possible to estimate the spectral indices of the magnetic field considering hourly averaged data. Further analysis on high-resolution data are required in order to better characterize the whole spectral behavior.

Bibliography

Alexakis, A., Mininni, P. D. & Pouquet, A. 2007 Turbulent cascades, transfer, and scale interactions in magnetohydrodynamics. *New J. Physics* **9**, 298.

Antonia, R. A., Anselmet, F. & Chambers, A. J. 1986 Assessment of local isotropy using measurements in a turbulent plane jet. *J. Fluid Mech.* **163**, 365–391.

Behannon, K. W., Acuna, M. H., Burlaga, L. F., Lepping, R. P., Ness, N. F. & Neubauer, F. M. 1977 Magnetic field experiment for voyagers 1 and 2. *Space Sci. Rev.* **21** (3), 235–257.

Belcher, J. W. & Davis, L. 1971 Large-amplitude Alfvén waves in the interplanetary medium. *J. Geophys. Res.* **76**, 3534–3563.

Bellamy, B. R., Cairns, I. H. & Smith, C. W. 2005 Voyager spectra of density turbulence from 1 au to the outer heliosphere. *J. Geophys. Res.* **110** (A10).

van den Berg, E. & Friedlander, M. P. 2007 Spgl1: A solver for large-scale sparse reconstruction. Http://www.cs.ubc.ca/labs/scl/spgl1.

Biferale, L., Mantovani, F., Pozzati, F., Sbragaglia, M., Scagliarini, A., Schifano, F., Toschi, F. & Tripiccione, R. 2011 Numerical simulations of Rayleigh-Taylor front evolution in turbulent stratified fluids. *Philos. T. Roy. Soc. A* **369** (1945), 2448–2455.

Biona, CB, Druilhet, A, Benech, B & Lyra, R 2001 Diurnal cycle of temperature and wind fluctuations within an African equatorial rain forest. *Agric. Forest Meteor.* **109** (2), 135–141.

Blackman, R. B. & Tukey, J. W. 1958 *The measurement of power spectra*. Dover Publications.

Borovsky, J. E. & Denton, M. H. 2010 Solar wind turbulence and shear: A superposed epoch analysis of corotating interaction regions at 1 au. *J. Geophys. Res.* **115**.

Bos, W. J., Kadoch, B., Schneider, K. & Bertoglio, J. P. 2009 Inertial range scaling of the scalar flux spectrum in two-dimensional turbulence. *Phys. Fluids* **21**, 115105.

Brethouwer, G., Hunt, J. C. R. & Nieuwstadt, F. T. M. 2003 Microstructure and lagrangian statistics of the scalar field with a mean gradient in isotropic turbulence. *J. Fluid Mech.* **474**, 193–225.

Bridge, H. S., Belcher, J. W., Butler, R. J., Lazarus, A. J., Mavretic, A. M., Sullivan, J. D., Siscoe, G. L. & Vasyliunas, V. M. 1977 The plasma experiment on the 1977 voyager mission. *Space Sci. Rev.* **21**, 259–287.

Bruno, R. & Carbone, V. 2013 The the solar wind as a turbulence laboratory. *Living Rev. Solar Phys.* **10** (2).

Burattini, P., Lavoie, P., Agrawal, A., Djenidi, L. & Antonia, R. A. 2006 Power law of decaying homogeneous isotropic turbulence at low reynolds number. *Phys. Rev. E* **73**, 066304.

Burattini, P., Lavoie, P. & Antonia, R. A. 2005 On the normalized turbulent energy dissipation rate. *Phys. Fluids* **17**, 098103.

Burlaga, L. F., Mish, W. H. & Roberts, D. A. 1989 Large-scale fluctuations in the solar wind at 1 AU: 1978–1982. *J. Geophys. Res.* **94** (A1), 177–184.

Candes, E. J., Romberg, J. K. & Tao, T. 2006*a* Robust uncertainty principles: exact signal reconstruction from highly incomplete frequency information. *IEEE T. Inform. Theor.* **52** (2), 489–509.

Candes, E. J., Romberg, J. K. & Tao, T. 2006*b* Stable signal recovery from incomplete and inaccurate measurements. *Commun. Pure Appl. Math.* **59** (8), 1207–1223.

Canuto, C., Hussaini, M.Y., Quaternoni, A. & Zang, T.A. 1988 *Spectral Methods in Fluid Dynamics*. Springer Verlag.

Celani, A., Cencini, M., Vergassola, M., Villermaux, E. & Vincenzi, D. 2005 Shear effects on passive scalar spectra. *J. Fluid Mech.* **823**, 99–108.

Chung, D. & Matheou, G. 2012 Direct numerical simulation of stationary homogeneous stratified sheared turbulence. *J. Fluid Mech.* **696**, 434–467.

Danaila, L. & Antonia, R. A. 2009 Spectrum of a passive scalar in moderate Reynolds number homogeneous isotropic turbulence. *Phys. Fluids.* **21**, 111702.

Danaila, L., Antonia, R. A. & Burattini, P. 2012 Comparison between kinetic energy and passive scalar energy transfer in locally homogeneous isotropic turbulence. *Physica D* **241**, 224–231.

Davies Wykes, Megan S. & Dalziel, Stuart B. 2014 Efficient mixing in stratified flows: experimental study of a rayleigh-taylor unstable interface within an otherwise stable stratification. *J. Fluid Mech.* **756**, 1027–1057.

Di Savino, S, Gallana, L, Iovieno, M & Tordella, D 2013 Transient formation of the passive scalar spectrum at a turbulent interface. In *Proceedings of the XXI AIMETA Conference*. Turin, Italy.

Donoho, D. L. 2006 Compressed sensing. *IEEE T. Inform. Theory* **52** (4), 1289–1306.

Donzis, D. A. & Yeung, P. K. 2010 Resolution effects and scaling in numerical simulations of passive scalar mixing in turbulence. *PhysicaD* **239**, 1287–1287.

Drazin, P. & Reid, D. 1981 *Hydrodynamic stability*. Cambridge (UK): Cambridge University Press.

Duarte, M.F. & Eldar, Y.C. 2011 Structured compressed sensing: From theory to applications. *IEEE T. Signal Proces.* **59** (9), 4053–4085.

Emran, M. S. & Schumacher, J. 2008 Fine-scale statistics of temperature and its derivatives in convective turbulence. *Journal of Fluid Mechanics* **611**, 13–34.

Fernando, HJS 1991 Turbulent mixing in stratified fluids. *Ann. Rev. Fluid Mech.* **23**, 455–493.

Fraternale, F., Gallana, L., Iovieno, M., Fosson, S., Magli, E., Tordella, D., Opher, M. & Richardson, J. D. 2015*a* Spectral analysis in the solar wind and heliosheath. In *Proceedings of the 14th Annual Internartional Astrophysics Conference*. Tampa Bay, FL, USA.

Fraternale, F., Gallana, L., Iovieno, M., Opher, M., Richardson, J. D. & Tordella, D. 2016 Turbulence in the solar wind: spectra from voyager 2 data at 5 au. *Phys. Scripta* **91** (2), 394–401.

Fraternale, F., Gallana, L., Iovieno, M., Richardson, J. D. & Tordella, D. 2015*b* Solar wind plasma: turbulence signature in voyager 2 1979 spectra. In *Proceedings of the Vortical Structures and Turbulence Conference*. Rome, Italy.

Frisch, U. 1995 *Turbulence: the legacy of A.N. Kolmogorov*. The address: Cambridge University Press.

Gallana, L., De Santi, F., Di Savino, S., Iovieno, M., Richiardone, R. & Tordella, D. 2015*a* Energy and water vapor transfer in a turbulent stratified environment. In *Proceedings of the 68th Annual Meeting of the APS Division of Fluid Dynamics*. Boston, MA, USA.

Gallana, L., De Santi, F., Di Savino, S., Iovieno, M. & Tordella, D. 2015*b* Entrainment temporal evolution across stably and unstably stratified vapor/clear air interfaces. In *Proceedings of the 15th European Turbulence Conference*. Delft, Netherlands.

Gallana, L, Di Savino, S, De Santi, F, Iovieno, M & Tordella, D 2014*a* Energy and water vapor transport across a simplified cloud-clear air interface. *J. Phys.: Conf. Series* **547** (1), 012042.

Gallana, L., Di Savino, S., De Santi, F., Iovieno, M. & Tordella, D. 2014*b* Intermittency layers associated to turbulent interfaces. In *Proceedings of the 9th European Fluid Mechanics Conference*. Rome, Italy.

Gallana, L., Di Savino, S., De Santi, F., Iovieno, M. & Tordella, D. 2014*c* Turbulent transport at a simplified clear air/cloud interface. In *Proceedings of the 4th International Conference Turbulent Mixing and Beyond Workshop*. Trieste, Italy.

Gallana, L, Di Savino, S, De Santi, F, Iovieno, M & Tordella, D 2016*a* Energy and scalar transport in a stratified turbulent shearless mixing. *under submission on J. Fluids Mech.* .

Gallana, L, Fraternale, F, Iovieno, M, Fosson, S, Magli, E, Richardson, J D, Opher, M & Tordella, D 2016*b* Voyager 2 solar plasma and magnetic field spectral analysis for intermediate data sparsity. *under pubblication on J. Geo. Res.* **55** (2), 394–401.

Gill, A. E. 1982 *Atmosphere-Ocean Dynamics*. Academic Press, New York, 662pp.

Gleick, J. 1987 *Chaos: making a new science*. New York, USA: Penguin Book New York.

Gotoh, T., Nagaki, J. & Kaneda, Y. 2000 Passive scalar spectrum in the viscous-convective range in two-dimensional steady turbulence. *Physics of Fluids* **12**, 155–168.

Gotoh, T., Watanabe, T. & Suzuki, Y. 2011 Scalar flux in a uniform mean scalar gradient in homogeneous isotropic steady turbulence. *Journal of Turbulence* **12**, 1–27.

Hansen, A. E., Marteau, D. & Tabeling, P. 1998 Two-dimensional turbulence and dispersion in a freely decaying system. *Phys. Rev. E* **58**, 7261–7271.

Hill, ME, Decker, RB, Brown, LE, Drake, JF, Hamilton, DC, Krimigis, SM & Opher, M 2014 Dependence of energetic ion and electron intensities on proximity to the magnetically sectored heliosheath: Voyager 1 and 2 observations. *Astroph. J.* **781** (2), 94.

Holzer, M. & Siggia, E. D. 1994 Turbulent mixing of a passive scalar. *Phys. Fluids* **6**, 1820–1837.

Horbury, Tim S & Tsurutani, Bruce 2001 Ulysses measurements of waves, turbulence and discontinuities. *The Heliosphere Near Solar Minimum: The Ulysses perspective, edited by: Balogh, A., Marsden, RG, and Smith, EJ, Springer-Praxis Books in Astrophysics and Astronomy, Springer, London, UK* pp. 167–227.

Hunt, J. C. R., Kaimal, J. C. & Gaynor, J. E. 1988 Eddy structure in the convective boundary-layer - new measurements and new concepts. *Q. J. Royal Met. Soc.* **114**, 827–858.

Iovieno, M., Cavazzoni, C. & Tordella, D. 2001 A new technique for a parallel dealiased pseudospectral Navier-Stokes code. *Comp. Phys. Comm.* **141**, 365–374.

Iovieno, M., Di Savino, S., De Santi, F. & Tordella, D. 2012 Intermittency layers associated to turbulent interfaces. In *Proceedings of the 9th European Fluid Mechanics Conference*. Rome, Italy.

Iovieno, M., Di Savino, S., Gallana, L. & Tordella, D. 2014 Mixing of a passive scalar across a thin shearless layer: concentration of intermittency on the sides of the turbulent interface. *J. Turb.* **15** (5), 311–334.

Iovieno, M, Gallana, L, Fraternale, F, Richardson, J D, Opher, M & Tordella, D 2016 Cross and magnetic helicity in the outer heliosphere from voyager 2 observations. *Eur. J. Mech. B/FluidsS* **55** (2), 394–401.

Iroshnikov, P. S. 1963 Turbulence of a conducting fluid in a strong magnetic field. *Sov. Astron.* **7**, 566–571.

Jameson, A., Schmidth, W. & Turkel, E. 1981 Numerical solution of the Euler equations by finite volume methods using Runge-Kutta time stepping schemes. *AIAA J.* .

Jayesh & Warhaft, Z. 1994 Turbulent penetration of a thermally stratified interfacial layer in a wind-tunnel. *J. Fluid Mech.* **277**, 23–54.

Joyce, C. J., Smith, C. W., Isenberg, P. A., Gary, S. P., Murphy, N., Gray, P. C. & Burlaga, L. F. 2012 Observation of bernstein waves excited by newborn interstellar pickup ions in the solar wind. *Astroph. J.* **745**, 112–120.

Joyce, C. J., Smith, C. W., Isenberg, P. A., Murphy, N. & Schwadron, N. A. 2010 Observation of bernstein waves excited by newborn interstellar pickup ions h+ and he+ as seen by voyager at 4.5 au. *Astroph. J.* **724**, 1256–1261.

KATUL, GG, GERON, CD, HSIEH, CI, VIDAKOVIC, B & GUENTHER, AB 1998 Active turbulence and scalar transport near the forest-atmosphere interface. *J. Appl. Meteor.* **37** (12), 1533–1546.

KEISLER, S. R. & RHYNE, R. H. 1976 An assesment of prewhitening in estimating power spectra of atmospheric turbulence at long wavelengths. *Nasa Technical Note* **D-8288**, 1–54.

KIMURA, Y. & HERRING, J. R. 1996 Diffusion in stably stratified turbulence. *Ann. Rev. Fluid Mech.* **328**, 253–269.

KLEIN, LW, MATTHAEUS, WH, ROBERTS, DA & GOLDSTEIN, ML 1992 Evolution of spatial and temporal correlations in the solar-wind - observations and interpretation. In *Solar Wind seven* (ed. E Marsch & R Schwenn), *COSPAR Colloquia Series*, vol. 3, pp. 197–200. 3rd COSPAR Colloquium on Solar Wind Seven, Goslar, Germany, Sep. 16-20, 1991.

KOLMOGOROV, A. N. 1941 The Local Structure of Turbulence in Incompressible Viscous Fluid for Very Large Reynolds' Numbers. In *Dokl. Akad. Nauk SSSR*, , vol. 30, pp. 301–305.

KOZA, J. R. 1992 *Genetic programming: on the programming of computers by means of natural selection*. MIT Press Cambridge.

KRAICHNAN, R. H. 1965 Inertial-range spectrum of hydromagnetic turbulence. *Phys. Fluids* **8**, 1385–1387.

KRAICHNAN, R. H. 1974 Convection of a passive scalar by a quasi-uniform random straining field. *J. Fluid Mech.* **64**, 737–762.

KRAICHNAN, R. H. 1994 Anomalous scaling of a randomly advected passive scalar. *Phys. Rev. Lett.* **72**, 1016–1019.

LEAMON, RJ, SMITH, CW, NESS, NF, MATTHAEUS, WH & WONG, HK 1998 Observational constraints on the dynamics of the interplanetary magnetic field dissipation range. *J. Geophys. Res.* **103** (A3), 4775–4787.

LEE, S. K., BENAISSA, A., DJENIDI, L., LAVOIE, P. & ANTONIA, R. A. 2012 Scaling range of velocity and passive scalar spectra in grid turbulence. *Phys. Fluids.* **24**, 075101.

LIN, J. T. & PAO, Y. K. 1979 Wakes in stratified fluids. *Ann. Rev. Fluid Mech.* **11**, 317–338.

LOTHON, MARIE, LENSCHOW, DONALD H. & MAYOR, SHANE D. 2009 Doppler Lidar Measurements of Vertical Velocity Spectra in the Convective Planetary Boundary Layer. *Bound. Lay. Meteor.* **132** (2), 205–226.

Lustig, M., Donoho, D.L., Santos, J.M. & Pauly, J.M. 2008 Compressed sensing mri. *Signal Processing Magazine, IEEE* **25** (2), 72–82.

Ma, B.K. & Warhaft, Z. 1986 Some aspects of the thermal mixing layer in grid turbulence. *Phys. Fluids* **29**, 3114–3120.

Malinowski, S. P., Gerber, H., Jen-La Plante, I., Kopec, M. K., Kumala, W., Nurowska, K., Chuang, P. Y., Khelif, D. & Haman, K. E. 2013 Physics of Stratocumulus Top (POST): turbulent mixing across capping inversion. *Atmos. Chem. Phys.* **13** (24), 12171–12186.

Marsch, E. & Tu, C.Y. 1989 Dynamics of correlation-functions with elasser variables for inhomogeneous mhd turbulence. *J. Plasma Phys.* **41**, 479–491.

Matthaeus, W. H. & Goldstein, M. L. 1982 Measurement of the rugged invariants of magnetohydrodynamic turbulence in the solar wind. *J. Geophys. Res.* **87** (NA8), 6011–6028.

Matthaeus, W. H., Goldstein, M. L. & Smith, C. W. 1982 Evaluation of magnetic helicity in homogeneous turbulence. *Phys. Rev. Letters* **48** (18), 1256–1259.

Mellado, Juan Pedro 2010 The evaporatively driven cloud-top mixing layer. *J. Fluid Mech.* **660**, 5–36.

Mellado, Juan Pedro, Stevens, Bjorn & Schmidt, Heiko 2014 Wind Shear and Buoyancy Reversal at the Top of Stratocumulus. *J. Atmos. Sci.* **71** (3), 1040–1057.

Mellado, Juan Pedro, Stevens, Bjorn, Schmidt, Heiko & Peters, Norbert 2009 Buoyancy reversal in cloud-top mixing layers. *Quart. J. Roy. Meteor. Soc.* **135** (641), 963–978.

Mizeva, I. A., Stepavov, R. A. & Frik, P. G. 2009 The cross-helicity effect on cascade processes in MHD turbulence. *Doklady Physics* **54** (2), 93–97.

Moeng, CH 2000 Entrainment rate, cloud fraction, and liquid water path of PBL stratocumulus clouds. *J. Atmos. Sci.* **57** (21), 3627–3643.

Moffatt, H. K. 1969 The degree of knottedness of tangles vortex lines. *J. Fluid Mech.* **36**, 117–129.

Moffatt, H. K. 1978 *Magnetic field generation in electrically conducting fluids*. Cambridge University Press.

Moffatt, H. K. & Tsinober, A. 1992 Helicity in laminar and turbulent flows. *Annu. Rev. Fluid Mech.* **24**, 281–312.

Montgomery, D, Brown, MR & Matthaeus, WH 1987 Density fluctuation spectra in magnetohydrodynamic turbulence. *J. Geophys. Res.* **92** (A1), 282–284.

Mydlarski, L. & Warhaft, Z. 1998 Passive scalar statistics in high peclet number grid turbulence. *J. Fluid Mech.* **358**, 135–175.

Opher, M 2015 The heliosphere: What did we learn in recent years and the current challenges. *Space Sci. Rev.* pp. 1–20.

Opher, M., Drake, J. F., Swisdak, M., Schoeffler, K. M., Richardson, J. D., Decker, R. B. & Toth, G. 2011 Is the magnetic field in the heliosheath laminar or a turbulent sea of bubbles? *Astroph. J.* **734** (1).

Orszag, S.A. & Gottlieb, D. 1980 *Approximation Methods for Navier-Stokes Problems*. Springer Verlag.

Parker, E. N. 1958 Dynamics of the interplanetary gas and magnetic fields. *Astrophys. J.* **128**, 664–676.

Podesta, J. J., Roberts, D. A. & Goldstein, M. L. 2007 Spectral exponents of kinetic and magnetic energy spectra in solar wind turbulence. *Astrophys J.* **664**, 543–548.

Pope, S.B. 2000 *Turbulent Flows*. Cambridge University Press.

Press, W. H. & Rybicki, G. B. 1992 The time delay of gravitational lens 0957+561. i. methodology and analysis of optical photometric data. *Astroph. J.* **385** (2, 1), 404–415.

Pumir, A. 1994 A numerical study of the mixing of a passive scalar three dimensions in the presence of a scalar gradient. *Phys. Fluids* **6**, 2118–2132.

Radkevich, A., Lovejoy, S., Strawbridge, K. B., Schertzer, D. & Lilley, M. 2008 Scaling turbulent atmospheric stratification. III: Space-time stratification of passive scalars from lidar data. *Quart. J. Roy. Meteor. Soc.* **134** (631, B), 317–335.

Richardson, JD & Decker, RB 2014 Voyager 2 observations of plasmas and flows out to 104 au. *Astrophys. J.* **792** (2), 126.

Richardson, J. D., Belcher, J., Tordella, D., Fraternale, F., Gallana, L. & Iovieno, M. 2015 Voyager 2 observations of plasma in the heliosheath. In *Proceedings of the AGU Fall Meeting*. San Francisco, CA, USA.

Richardson, J. D., Liu, Y. & Wang, C. 2008 Solar wind structure in the outer heliosphere. *Adv. Space Res.* **41** (2), 237–244.

Roberts, D. A. 2010 Evolution of the spectrum of solar wind velocity fluctuations from 0.3 to 5 au. *J. Geophys. Res.* **115**.

Roberts, D. A. & Goldstein, M. L. 1987 Spectral signatures of jumps and turbulence in interplanetary speed and magnetic-field data. *J. Geophys. Res.* **92** (A9), 10105–10110.

Rosenblatt, H. M. 1965 Spectral analysis and parametric methods for seasonal adjustment of economic time series. *Working paper - U. S. Bureau of the Census* **23**, 235–257.

Rudelson, M. & Vershynin, R. 2006 Sparse reconstruction by convex relaxation: Fourier and gaussian measurements. In *2006 40th Annual Conference of Information Sciences and Systems, Vols. 1-4*, pp. 207–212. Princeton Univ, Dept Elect Engn; IEEE Informat Theory Soc, 40th Annual Conference on Information Sciences and Systems (CISS), Princeton, NJ, Mar. 22-24, 2006.

Rybicki, G. B. & Press, W. H. 1992 Interpolation, realization, and reconstruction of noisy, irregularly sampled data. *Astroph. J.* **398**, 169–176.

Schumacher, J. & Sreenivasan, K. R. 2005 Statistics and geometry of passive scalars in turbulence. *Physics of Fluids* **17**, 1–19.

Shen, X & Warhaft, Z 2000 The anisotropy of the small scale structure in high Reynolds number (R(lambda)similar to 1000) turbulent shear flow. *Phys. Fluids* **12** (11), 2976–2989.

Shraiman, B. I. & Siggia, B. I. 2000 Scalar turbulence. *Nature* **405**, 639–646.

Smith, C. W., Hamilton, K., Vasquez, B. J. & Leamon, R. J. 2006*a* Dependence of the dissipation range spectrum of interplanetary magnetic fluctuations upon the rate of energy cascade. *Astroph. J. Lett.* **645** (1, 2), L85–L88.

Smith, C. W., Vasquez, B. J. & Hamilton, K. 2006*b* Interplanetary magnetic fluctuation anisotropy in the inertial range. *J. Geophys. Res.* **111** (A9).

Sreenivasan, K.R. 1996 The passive scalar spectrum and the obukhov-corrsin constant. *Phys. Fluids* **8**, 189–196.

Sreenivasan, K. R. & Antonia, R. A. 1997 The phenomenology of small-scale turbulence. *Ann. Rev. Fluid Mech.* **29**, 435–472.

Tennekes, Hendrik & Lumley, John Leask 1972 *A first course in turbulence*. Cambridge (Mass.), London: M.I.T. Press.

Tong, C. R. & Warhaft, Z. 1994 On passive scalar derivative statistics in grid turbulence. *Phys. Fluids* **6**, 2165–2176.

Tordella, D., Gallana, L., De Santi, F., Di Savino, S., Iovieno, M. & Richiardone, R. 2014 Turbulent transport across an interface between dry and humid air in a stratified environment. In *Proceedings of the 67th Annual Meeting of the APS Division of Fluid Dynamics*. San Francisco, CA, USA.

Tordella, D. & Iovieno, M. 2006 Numerical experiments on the intermediate asymptotics of the shear-free turbulent transport and diffusion. *J. Fluid Mech.* **549**, 429–441.

Tordella, D. & Iovieno, M. 2011 Small scale anisotropy in the turbulent shearless mixings. *Phys. Rev. Lett.* **107**, 194501.

Tordella, D. & Iovieno, M. 2012 Decaying turbulence: what happens when the correlation length varies spatially in two adjacent zones. *Physica D* **242**, 270–281.

Tordella, D., Iovieno, M. & Bailey, P. R. 2008 Sufficient condition for gaussian departure in turbulence. *Phys. Rev. E* **77**, 016309.

Tordella, D., Iovieno, M. & Ducasse, L. 2012 Dimensionality influence on passive scalar transport. *Journal of Physics: Conference Series* **318**, 052042, Proceedings of the *13th European Turbulence Conference.*

Tu, C.-Y & Marsch, E. 1995 Mhd structures, waves and turbulence in the solar wind: observations and theories. *Space Sci. Rev.* **73** (1-2), 1–210.

Vallis, G. K. 2006 *Atmospheric and Oceanic Fluid Dynamics*. Cambridge, U.K.: Cambridge University Press.

Veeravalli, S. & Warhaft, Z. 1989 The shearless turbulence mixing layer. *J. Fluid Mech.* **207**, 191–229.

Veeravalli, S. & Warhaft, Z. 1990 Thermal dispersion from a line source in the shearless turbulence mixing layer. *J. Fluid Mech.* **216**, 35–70.

Vucelja, M., Falkovich, G. & Turitsyn, K. S. 2012 Fractals iso-contours of passive scalar in two-dimensional smooth random flows. *J. Stat. Phys.* **147**, 424–435.

Warhaft, Z. 2000 Passive scalar in turbulent flows. *Ann. Rev. Fluid Mech.* **32**, 203–240.

Watanabe, T. & Gotoh, T. 2007 Scalar flux spectrum in isotropic steady turbulence with a uniform mean gradient. *Physics of Fluids* **19**, 121707.

Wood, Robert 2012 Stratocumulus Clouds. *Mon. Weather Rev.* **140** (8), 2373–2423.

Xu, Guangwu & Xu, Zhiqiang 2015 Compressed sensing matrices from fourier matrices. *IEEE Trans. Inf. Theory* **61** (1), 469–478.

Yeung, P.K., Donzis, D. A. & Sreenivasan, K. R. 2004 Simulation of three-dimensional turbulent mixing for schmidt numbers of order 1000. *Flow, Turbulence and Combustion* **72**, 333–374.

Yokoi, N. 2013 Cross helicity and related dynamo. *Geophysical and Astrophysical Fluid Dynamics* **92**, 114–184.

Yokoi, N. & Balarac, G. 2011 Cross-helicity effects and turbulent transport in magnetohydrodynamic flow. *J. Physics: Conf. Series* **318**, 072039.

Zhou, T., Antonia, R. A. & Chua, L. P. 2002 Performance of a probe for measuring turbulent energy and temperature dissipation rates. *Exp. in Fluids* **33**, 334–345.

Zhou, Y, Matthaeus, WH & Dmitruk, P 2004 Colloquium: Magnetohydrodynamic turbulence and time scales in astrophysical and space plasmas. *Rev. Mod. Phys.* **76** (4), 1015–1035.